University of Duisburg-Essen
Department of Chemistry
Applied Analytical Chemistry

Improvement of atmospheric pressure ion sources for mass spectrometry

Dissertation
for the academic degree of
Doctor of natural sciences
Dr. rer. nat.

Presented by

Alexandra Pape

The here presented work was performed from May 2021 until May 2024 in the working group by Prof. Dr. O. J. Schmitz in Applied Analytical Chemistry at the University of Duisburg-Essen.

Day of Defense:	25/06/2024
Reviewer:	Prof. Dr. Oliver J. Schmitz Private lecturer Dr. Ursula Telgheder
Chairman:	Prof. Dr. Sebastian Schlücker

DOI: 10.17185/duepublico/82129
URN: urn:nbn:de:hbz:465-20240703-065105-6

I hereby certify that I have written the here presented thesis

“Improvement of atmospheric pressure ion sources for mass spectrometry”

myself and without external help. I have not used any auxiliary materials or sources other than those indicated and segments that have been adopted from other sources have been marked as such. The thesis has not been submitted in this or in a similar form to any other university. I assure that I have made the previous statement to the best of my knowledge and belief. I am aware of the consequences of an incorrect affirmation according to § 156 StGB leading to up to three years of imprisonment or fine in the case of a deliberate act and according to § 161 Section 1 StGB leading to up to one year of imprisonment or fine in the case of a negligent act.

02/05/2024

Alexandra Pape

“It is possible to commit no mistakes and still lose. That is not a weakness. That is life.”

– Captain Picard in “Star Trek: The Next Generation”

Acknowledgements

I would like to thank Prof. Dr. Oliver Schmitz for the opportunity to perform my doctoral work in his laboratory. I would also like to thank my colleagues for their technical counsel.

I would like to thank Hitachi High-Tech Corporation for their financial and technical support and their counsel.

I would like to thank my parents for supporting, understanding, and enduring me throughout this difficult time.

0. Table of Content

1. List of Abbreviations

3D	three-dimensional
AC	alternating current
AF	ammonium formate
AIMS	ambient ionization mass spectrometry
AP1	atmospheric pressure stage 1
APCI	atmospheric pressure chemical ionization
API	atmospheric pressure ionization
APLI	atmospheric pressure laser ionization
APPI	atmospheric pressure photoionization
APPJ	atmospheric pressure plasma jet
Aux.	auxiliary
avg.	average
°C	degree Celsius
CAD	computer-assisted drawing
CEM	chain ejection model
CI	chemical ionization
CRM	charged residue model
CWA	chemical warfare agent
DART	direct analysis in real time
DBD(I)	dielectric barrier discharge (ionization)
DC	direct current
DESI	desorption electrospray ionization
DoE	design of experiments

EI	electron ionization
ESI	electrospray ionization
eV	electron volt
FA	formic acid
FAPA	flowing atmospheric pressure afterglow
FID	flame ionization detector
FµTP	flexible microtube plasma
FoM	figures of merit
GC	gas chromatography
H	hydrogen
HPLC	high-performance liquid chromatography
HV	high voltage
IEM	ion evaporation model
iLOD	instrumental limit of detection
iLOQ	instrumental limit of quantification
iLTP	inverse low temperature plasma
kV	kilovolt
kV_{pp}	kilovolt, measured from peak to peak
L	liter
LC	liquid chromatography
LiF	laser-induced fluorescence
LOD	limit of detection
LOQ	limit of quantification
LTP	low temperature plasma
M	molecule

MALDI	matrix-assisted laser desorption/ ionization
min	minute
MIPDI	microwave induced plasma desorption/ionization
mmol	millimole
mg	milligram
µg	microgram
mL	milliliter
MRM	multiple reaction monitoring
MS	mass spectrometry
m/z	mass to charge ratio
Neb.	nebulizing
OES	optical emission spectroscopy
opt.	optimization
PADI	plasma-assisted desorption ionization
PDA	phase doppler anemometry
PEEK	polyether ether ketone
PTFE	polytetrafluoroethylene
Q0	quadrupole 0
QC	quality control
R.	repeller
R^2	regression factor
rf	radio-frequency
rpm	rounds per minute
RSD	relative standard deviation
s	seconds

SICRIT	soft ionization by chemical reaction in transfer
Std. dev.	standard deviation
TIC	total ion chromatogram
TPI	tube plasma ionization
UPLC	ultra-performance liquid chromatography
UV-VIS	ultraviolet-visible
USN	ultrasonic nebulizer
V	volt

2. Summary

In the first project, a new nebulization system for a liquid chromatography – mass spectrometry application (LC-MS) utilizing an inverse low temperature plasma (iLTP) ion source was developed. Instead of a standard atmospheric pressure chemical ionization nebulizer, two commercial nebulizers were disassembled and re-configured to spray the liquid chromatograph eluent onto the ionizing plasma in front of the mass spectrometer inlet. Since both devices, a medical inhaler by Omron and a bottle humidifier by Daiso, demonstrated irregular vibration and nebulization properties as well as a lack of mechanical robustness, another ultrasonic spraying device was developed in cooperation with Hitachi High-Tech corporations. For this application, focusing cones were developed to transport the solvent into gas phase and to focus the spray onto the plasma region to ensure better ionization. A design of experiments was performed to find the best operating parameters, and calibration curves were established to compare both the standard nebulizer and the Hitachi ultrasonic nebulizer. In general, the standard nebulizer proved advantageous which leaves further room for improvement of the ultrasonic nebulization for mass spectrometry applications. Furthermore, the iLTP ion source was compared to a tube plasma ionization configuration. Even though the tube plasma ionization ion source was less robust, its sensitivity was higher than that of the iLTP ion source.

In a second project, a repeller electrode was inserted into an electrospray ionization (ESI) housing to improve the ion transfer from the electrospray capillary to the mass spectrometer inlet. Different repeller designs were manufactured and their position and applied voltage optimized. It was found that the *m/z* of the investigated molecules and the flow rate of the supplied liquid influenced the peak intensity and the required repeller voltage to reach a signal intensity maximum. Smaller repellers were discovered to give better results and a concave repeller with a diameter of 12 mm was found optimal. A design of experiments provided optimal spatial conditions and repeller voltage. However, the effect that the repeller had on the overall results at the applied liquid chromatography flow rate (450 µL min^{-1}) was rather small in contrast to lower flow rates. A subsequent analysis of human plasma spiked with testosterone and reserpine also showed little improvement with the repeller electrode. It was furthermore discovered that the repeller electrode did not only aid the transfer of ions from the electrospray capillary into the mass spectrometer inlet, but that it was capable of ionizing molecules without any other ionization source present.

In the third project, the iLTP and a nanoESI ion source were coupled in a dual ion source design in front of a single quadrupole mass spectrometer. Due to the unshielded set-up, the experiments remained prone to environmental influences, but the parameters of both ion sources influencing the measurements were successfully investigated and subsequently optimized. The integration of a plasma ion source between ESI capillary and MS inlet showed a significant increase in the total ion current and the signal response of the test compound reserpine.

Im ersten Projekt wurde ein neues Verneblersystem für eine inverse Niedrigtemperaturplasma (iLTP)-Ionenquelle in einem Flüssigkeitschromatographie-Massenspektrometrie (LC-MS)-Aufbau entwickelt. Anstelle eines herkömmlichen Verdampfers, wie er in einer Chemischen Ionisation unter Atmosphärendruck (APCI)-Ionenquelle verwendet wird, wurden zwei kommerzielle, auf Ultraschall basierende Vernebler auseinandergebaut und neu konfiguriert, um den Eluenten der LC in das ionisierende Plasma vor dem Einlass des Massenspektrometers zu sprühen. Im Laufe der Untersuchungen stellten sich sowohl der medizinische Inhalator der Firma Omron als auch der Raumvernebler von Daiso als wenig robust mit unregelmäßiger Vibration und Verneblung heraus, weswegen in Kooperation mit Hitachi High-Tech ein neues Verneblersystem entwickelt wurde. Für den Sprayer wurde ein beheizbarer Fokussierungskonus designt, der den LC-Eluent möglichst trocken in die Gasphase überführen und auf die Plasmaregion fokussieren sollte. Dabei zeigte sich, dass der APCI-Verdampfer momentan noch etwas bessere Ergebnisse liefert, aber der Ultraschall-Vernebler für die Anwendung in der Massenspektrometrie großes Entwicklungspotential aufweist. Des Weiteren wurde die iLTP-Ionenquelle mit der tube plasma ionization (TPI)-Konfiguration verglichen. Obwohl die TPI-Konfiguration weniger robust erscheint, zeigte sie eine bessere Sensitivität als die iLTP-Ionenquelle.

Im zweiten Projekt wurde eine Repeller-Elektrode in das Gehäuse einer Elektrospray-Ionisation (ESI)-Ionenquelle eingebaut, um den Ionentransfer von der Elektrospray-Kapillare in den Einlass des Massenspektrometers zu verbessern. Verschiedene Repellergeometrien wurden designt und produziert und anschließend deren Position im Gehäuse sowie die angelegte Repellerspannung optimiert. Dabei stellte sich heraus, dass das *m/z* der untersuchten Moleküle und die Flussrate der Standards einen Einfluss auf die Peakintensität, sowie auf die benötigte Repellerspannung hatten. Mit einem Design of Experiments wurden die Position und Spannung optimiert. Bei der Nutzung der LC bei entsprechender Flussrate (450 µL min^{-1}) war der Repeller-Effekt im Vergleich zu den Spritzenpumpenexperimenten mit niedrigerer Flussrate stark verringert. Anschließend wurde die optimierte LC-MS-Methode an menschlichem Plasma,

welches mit den Analyten Testosteron und Reserpin gespiked wurde, getestet und wies im Vergleich zur unmodifizierten ESI bisher nur eine geringe Verbesserung auf. Es wurde außerdem herausgefunden, dass der Repeller nicht nur den Ionentransfer von der Elektrospray-Kapillare in den Einlass des Massenspektrometer begünstigte, sondern dass er in der Lage war, Ionen ohne weitere Ionenquelle zu ionisieren.

Im dritten Projekt wurde die iLTP-Ionenquelle mit einer nanoESI-Ionenquelle und einem Quadrupol-Massenspektrometer gekoppelt. Aufgrund des freien Aufbaus blieb das Experiment abhängig von Umgebungseinflüssen, dennoch konnten die Parameter beider Ionenquellen, die einen Einfluss auf die Messergebnisse hatten, erfolgreich untersucht und anschließend optimiert werden. Das Zuschalten einer Plasmaionenquelle zwischen einer ESI-Kapillare und dem Einlass des Massenspektrometers wies einen signifikanten Anstieg des Totalionenstroms auf, sowie eine Erhöhung der Signalintensität der Testsubstanz Reserpin im Massenspektrum.

3. Introduction and theoretical background

3.1 Low temperature plasma ionization

The content of this chapter was partially used in the publication Pape and Schmitz (2024)[1].

Originally, detectors like the flame ionization detector, the electron capture detector, and the thermal conductivity detector were used for gas chromatography (GC) analysis, and ultraviolet – visible (UV-VIS) detectors, fluorometric or electrochemical detectors were implemented in liquid chromatography (LC) devices. Mass spectrometers, however, offer a unique capability of elucidating the chemical composition of compounds and can not only be coupled to GC, but since the difficulty of introducing the liquid eluent into the vacuum system of early mass spectrometers has been overcome they are also being successfully employed as LC detectors.[2]

The interface between chromatographic systems and mass spectrometers is the ionization source. The most common ionization sources under vacuum are Electron Ionization (EI) and Chemical Ionization (CI), and they are usually combined with GC. EI, however, suffers from strong fragmentation of the analyte molecules. CI on the other hand provides the possibility of controlling the extent of the fragmentation and thus gives more information on the molecular weight of the molecules. While the group of techniques that fall under atmospheric pressure ionization (API) sources were first invented for LC-mass spectrometry (MS) couplings as liquid samples do not have to be introduced into a vacuum, they can now also be coupled to GC or used as ambient ionization mass spectrometry (AIMS) without any connected separation technique.[2-4]

API and AIMS techniques are not always strictly separable since AIMS techniques usually also work under atmospheric pressure. However, they often do not require sample preparation, they are compatible with and directly coupled to MS, and they employ soft ionization since excessive fragmentation can prevent sample identification.[3] Due to the lack of sample pretreatment, they are faster, cheaper, simpler and allow spatial sample examinations when coupled to corresponding techniques, and reduce the risk of contamination and carry-over[5]. However, in contrast to established GC- and LC-techniques, quantification is not yet possible as such[6].

One of the most common API sources is the electrospray ionization (ESI) source developed by the Fenn group[7] whose corresponding AIMS technique is the desorption-electrospray ionization (DESI) by Takáts *et al.* (2004)[8] which can desorb and ionize the analytes directly from an insulated surface[7-9]. The other “gold-standard”, and rather complementary API technique (cf. Figure 1), is the atmospheric pressure chemical ionization (APCI) by Horning *et al.* (1974). The analytes are ionized directly or via ionized nitrogen through a corona discharge at a needle electrode.[10-14]

Besides ESI and APCI, well known ion sources are atmospheric pressure photoionization (APPI), in which not a needle electrode but a vacuum-UV photon-generation lamp ionizes the analyte molecules, and atmospheric pressure laser ionization (APLI), in which a laser is used to ionize aromatic ring systems.[15, 16] An overview of the polarity and molecule weight range of the ionization types is given in Figure 1.

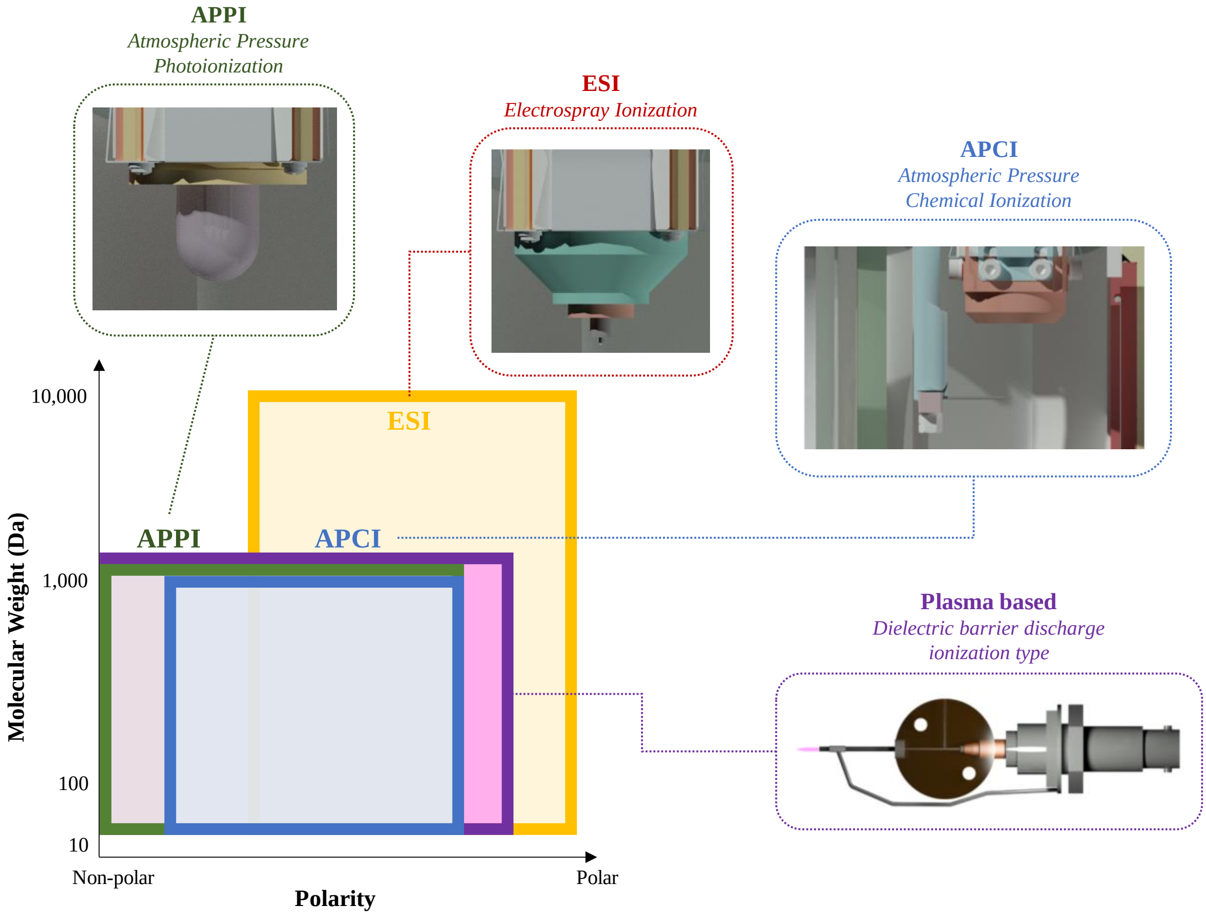

Figure 1: Optimal polarity and molecular weight of samples measured with different types of ion sources.[1]

ESI and DESI techniques belong to the spray-based ion sources. Besides laser ionization and photo ionization, there is also plasma ionization[17]. Plasma-based ion sources can be sorted into corona discharge techniques, glow discharge techniques, microwave-induced plasma techniques, and dielectric barrier discharge (DBD) techniques. While microwave-induced plasmas can reach from a few hundred up to a thousand degrees, the low temperature plasma (LTP), which is the focus of the present work, has only roughly 30 °C.[18, 19]

Figure 2 gives an overview of a selection of plasma-based ion sources.

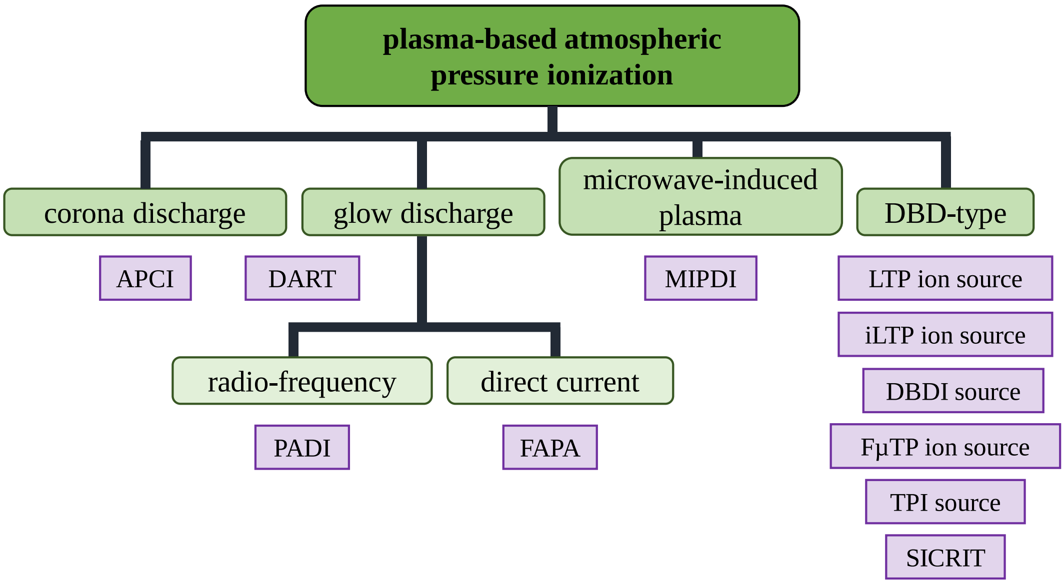

Figure 2: An overview over main plasma ion source types relevant to the present work: APCI[11]*, direct analysis in real-time (DART)*[20]*, plasma-assisted desorption ionization (PADI)*[21]*, flowing atmospheric pressure afterglow (FAPA)*[22]*, microwave induced plasma desorption/ ionization (MIPDI)*[18]*, LTP*[23]*, inverse LTP (iLTP)*[24]*, dielectric barrier discharge ionization (DBDI)*[25]*, flexible microtube plasma (FμTP)*[24]*, tube plasma ionization (TPI)*[26]*, soft ionization by chemical reaction in transfer (SICRIT)*[27]*.*[1]

The first application for DBDs was in ozone generation[28]. A typical DBD set-up is shown in Figure 3. An electric circuit consists of a high voltage (HV) alternating current (AC) source, grounding, as well as an HV electrode and a ground electrode between which there are a gap and one or two insulating material layers called dielectric barriers.

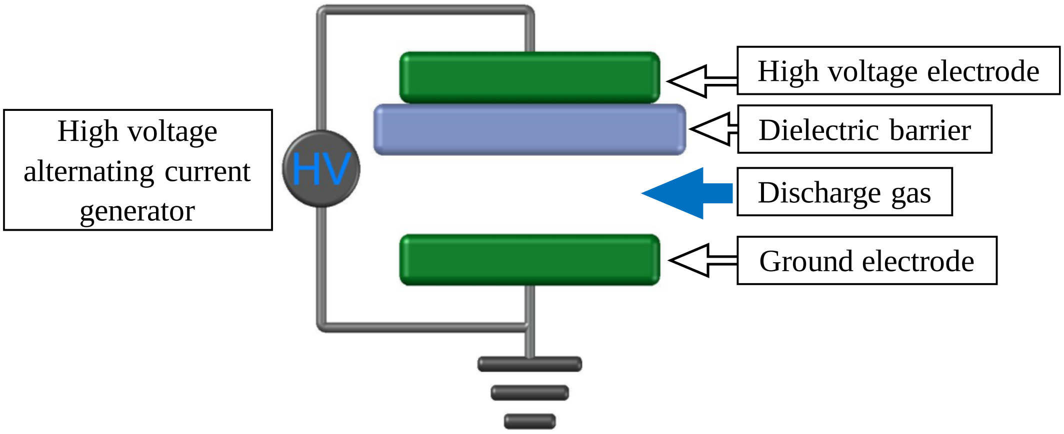

Figure 3: Physical set-up of a DBD. (Adapted from Kogelschatz et al. (1999)[29]*)*

As soon as AC voltage is applied, electrons travel from the HV cathode in the direction of the grounded anode. Only when a certain voltage, the so-called Paschen voltage, is reached, tiny filaments are formed through which the charge flows, the so-called electrical breakdown, as seen in Figure 4 (pink discharge channels). These filaments disappear after nanoseconds, but the so-called memory effect makes new micro-channels form at the position of the old ones while also lowering the required minimum voltage. The charge accumulates on the surface of the dielectric, creating an electric field against the externally applied field, leading to an interruption of the current flow.[30, 31]

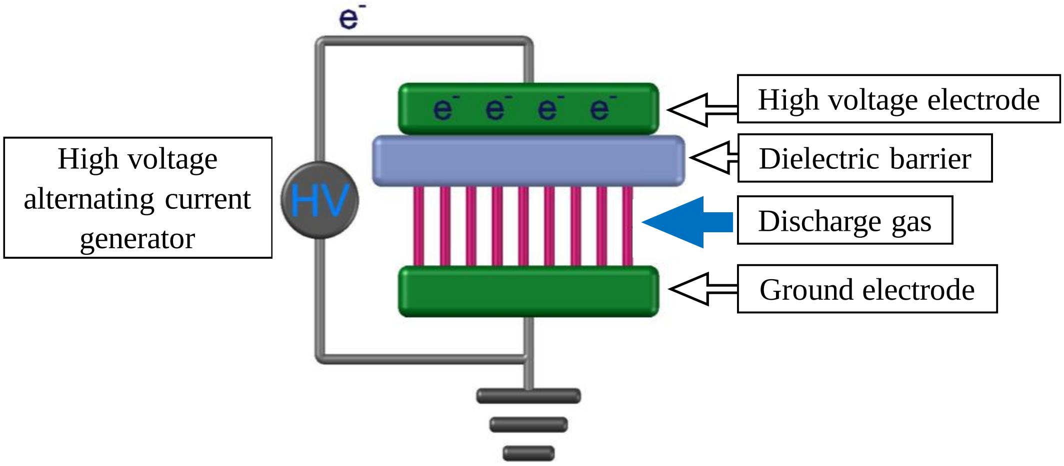

Figure 4: AC voltage applied to the DBD set-up: Microdischarges have begun to form and energetic electrons collide with the gas in the gap. (Adapted from Kogelschatz et al. (1999)[29])

When the electrons pass through the gap, they collide with the atmospheric molecules or with the discharge gas that is introduced into the gap and that is often helium or argon. A chain reaction takes place which leads to the ignition of the plasma, which contains electrons, molecular ions, and atomic ions. Since the electrons are much faster than the other particles, this plasma is a non-equilibrium plasma or LTP.[25, 29, 32]

Na *et al.* (2007) were the first to implement a DBD as an ion source for MS. Their set-up, called DBDI source, consisted of a hollow needle electrode made of stainless steel and a copper counter electrode. To analyze amino acids and explosives, the samples were placed on a glass slide which functioned as the dielectric barrier.[25, 33] Nowadays, the name “DBDI source” is used for DBD-based ion source configurations in which the HV and ground electrodes are placed as rings over a dielectric tube through which the discharge gas is channeled (Figure 5A).

During the course of the years, different electrode arrangements have been developed. For electrode configurations with a needle electrode on ground inside the dielectric tube and a ring electrode on HV, the name LTP ion source (Figure 5B) is used. It was first implemented by Harper *et al.* (2008) with a stainless steel needle inside a quartz tube dielectric barrier and an outer copper ring electrode to analyze explosives[23]. In the opposite configuration, namely with the needle electrode on HV, the configuration is called an iLTP ion source (Figure 5C)[34, 35]. Removing the grounded ring electrode leads to a TPI source (Figure 5D) which has the same configuration as the FµTP, the first ground-electrode free DBD-type ion source which additionally featured miniaturization and a flexible dielectric tube (Figure 5E)[24, 26]. For each of these configurations, different physical parameters such as sizes, distances, materials, and diameters have been optimized[36].

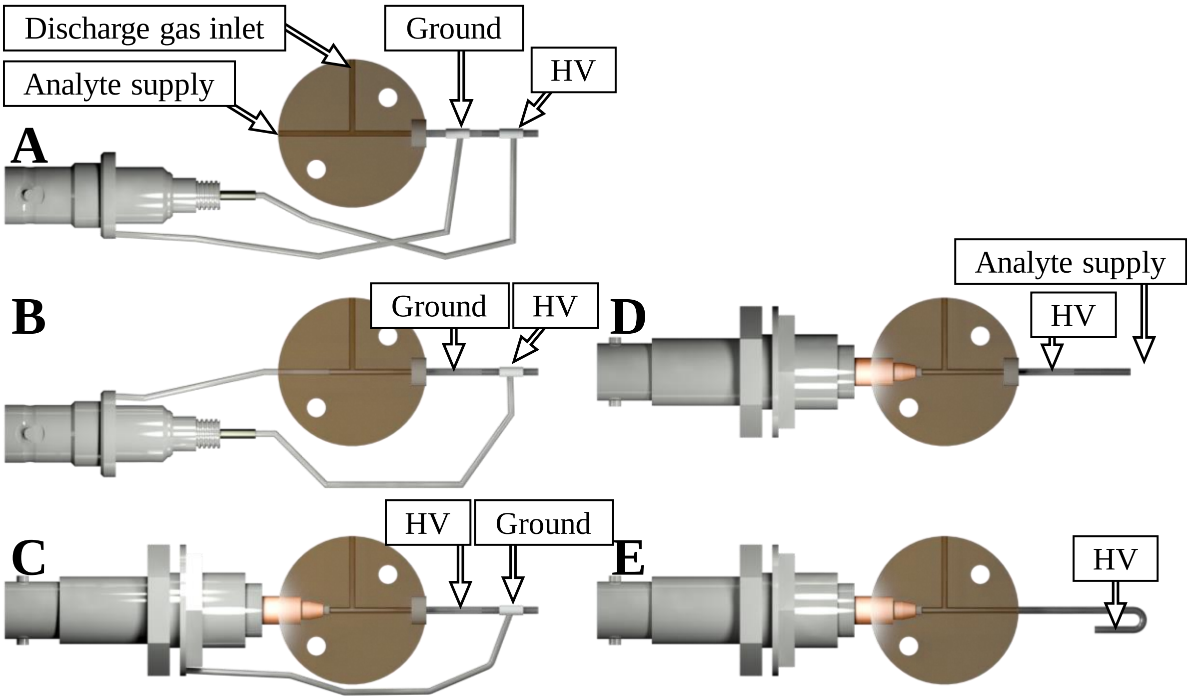

Figure 5: Schematic set-up of typical electrode configurations of DBD-based plasma ion sources; A: DBDI (based on unpublished work), B: LTP (based on Harper et al. (2008) [23]), C: iLTP (based on Brecht et al. (2021)[35]), D: TPI (based on Ayala-Cabrera et al (2022)[26]), E: FµTP (based on Brandt et al. (2017)[24]).[1]

The electrons which travelled from the HV electrode through the insulator into the gap can react there with the atmospheric molecules or supplied discharge gas. In the case of helium, it leads to the formation of helium metastable (He^M) species with an energy of 19.82 and 20.61 eV as can be seen in Figure 6.[37]

$He + e^- \rightarrow He^M + e^-$ *Equation 1*

In addition, helium is excited to further species of different energies which are described here as He*[38].

$He + e^- \rightarrow He^* + e^-$ *Equation 2*

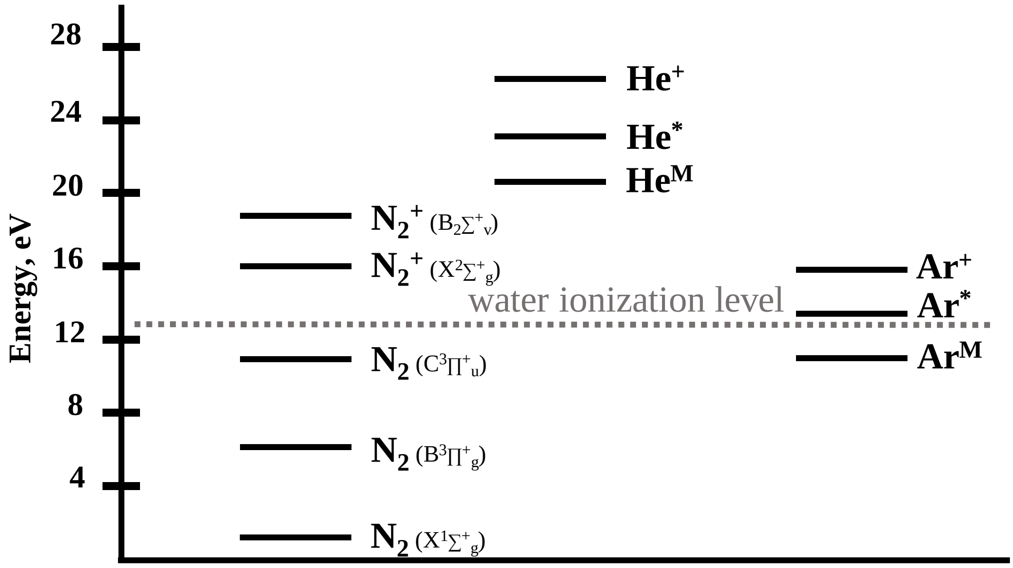

Figure 6: Energy levels of different species of nitrogen, helium, and argon, as well as the energy level required to ionize water (based on Kratzer et al. (2011)[39]).[1]

He^M can ionize nitrogen in the so-called Penning ionization. The ionized nitrogen then reacts further via mechanisms close to those found in APCI ion sources, eventually leading to water clusters which are capable of protonating the analyte molecules.[22, 40, 41]

$He^M + N_2 \rightarrow He + N_2^{\bullet+} + e^-$ *Equation 3*

$N_2^{\bullet+} + 2\ N_2 \rightarrow N_4^{\bullet+} + N_2$ *Equation 4*

$N_4^{\bullet+} + H_2O \rightarrow H_2O^{\bullet+} + 2\ N_2$ *Equation 5*

$H_2O^{\bullet+} + H_2O \rightarrow H_3O^+ + OH^{\bullet}$ *Equation 6*

$H_3O^+ + n\ H_2O \rightarrow H_3O^+(H_2O)_n$ *Equation 7*

A lot of research focusses on the elucidation of plasma chemistry for different conditions and discharge gases. While the reaction mechanisms for helium are thought to be uncovered, the reactions for argon and other noble gases remain to be found. Since the energies of the metastable species of argon (11.55 eV and 11.72 eV, cf. Figure 6) are less than those of helium, they are unable to ionize nitrogen and the above-mentioned chain reaction cannot take place.[42] Since ionization with argon plasma occurs, alternative reactions for the argon plasma chemistry have to be found.

DBD-based plasmas have experienced a surge in attention in the development of ion sources and applications. Reviews deal with developments[43-47], applications[48-51] or both[6, 37, 52-56], and various theses have also been published on this topic[1, 57-63].

As mentioned above, Na *et al.* (2007) were the first to use a DBD as an ionization source in mass spectrometry. In their configuration as seen in Figure 7, 3.5 – 4.5 kV were applied to a hollow stainless steel needle which was connected to a copper counter electrode. In between, a glass slide functioned as both dielectric barrier and sample plate. They measured amino acids and explosives without sample preparation in negative ion mode using an ion-trap mass spectrometer. Helium, nitrogen, argon, and air were used as discharge gases with the former being the best.[25, 33]

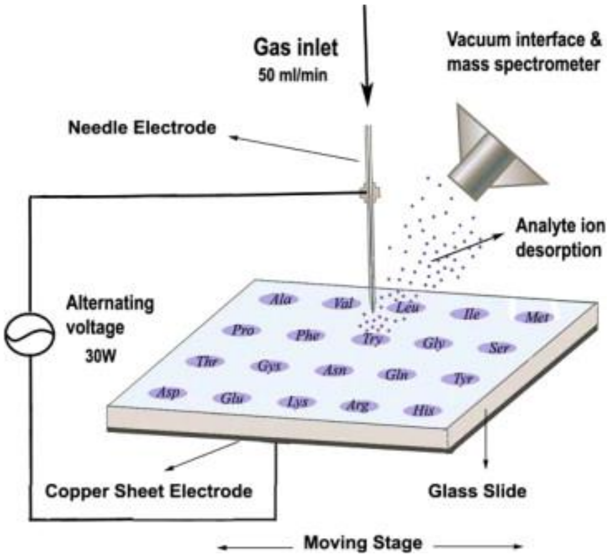

Figure 7: Experimental set-up used in the earliest DBD-based ion source experiments by Na et al. (2007).[25]

After this, research on this topic has skyrocketed. In the same year, a DBDI source, meaning two ring electrodes, was coupled to an ion mobility spectrometer (IMS)[64]. A year later, Harper *et al.* (2008) developed an LTP ion source[23]. It was used in an ambient set-up to analyze untreated olive oil which had been placed on a heated surface in front of the mass spectrometer inlet[65]. Miniaturization of this ion source gave the advantage of lower gas consumption, and in-situ studies were executed to differentiate between organic apples and non-organic ones in which diphenylamine, a common fungicide, was found[66]. Furthermore, without the need of additional heating, they also detected explosives on a glass surface, similar to the application by Na *et al.* (2007)[33, 67]. In most instances, however, heating is necessary for the transfer of the analyte molecules into the gas phase when an LTP is used[39, 68]. In the case of the Flowing Atmospheric Pressure Afterglow (FAPA) ion source, the plasma temperatures are much higher while the energy consumption is much lower with 400 – 500 V instead of 1.5 – 2.5 kV in DBD-based ion sources[22, 69, 70]. Thus, with plasma temperatures around 200 °C, FAPA was proven to obtain better analysis results for less volatile organic molecules in comparison to LTP and DART when no additional heat was used[68]. It was also found less prone to matrix effects[71]. However, the choice of plasma must be made in dependence of the analyte since the sample must be able to withstand heat and only fragment if desired.

Comparisons have not only been performed between different types of plasma ion sources, but also between different DBD-based plasma ion source configurations[34, 72]. Besides investigating the plasma chemistry[72-74], the Institute for Applied Sciences (ISAS) in Dortmund has taken a closer look at the influence of HV amplitude and duty cycle on the degree of fragmentation[75], as well as at discharge modes[76], discharge gas doping[42] or control of the atmospheric conditions[77].

Besides ambient applications, DBD-based ion sources have also been employed in LC-MS couplings. The DBDI is often capable of reaching better sensitivities than ESI and APCI and for some samples even displays less or comparable matrix effects[13, 35, 78-80]. Prior chromatography might identify a vaster majority of molecules like in the analysis of olive oil[78], fruit[79], and soil samples[80], but the sample preparation and separation leads to a higher expenditure of time.

Hagenhoff and Hayen (2018) compared their DBDI with ESI and APCI to detect vitamin D metabolites. The most common mechanisms for DBDI and APCI seemed to include the loss of water (e.g. $[M+H-H_2O]^+$), but they showed less matrix effects in the solvent and extracted serum-based samples as this is usually an issue encountered in ESI analysis.[81]

In GC-MS, EI is often used as the gold standard which leads to heavy fragmentation. Thus, DBDI sources could not only provide softer ionization but also higher sensitivity[82, 83].

The TPI developed by Ayala-Cabrera *et al.* (2022) comprises only an HV needle electrode inside a quartz tube while the ion source housing functions as the “virtual” ground electrode (cf.

Figure 5D). Employed in GC-MS, dopants such as water, toluene, and acetone were placed in the ion source housing in an effort to optimize the analysis conditions further. As such, the TPI outperformed APCI and APPI in a contaminant standard mixture including PAHs, esters, and nitro-compounds[26] as well as in an investigation of phthalates in plastics (not yet published).

The FµTP by Brandt *et al.* (2018) also reached higher sensitivity, a lower limit of detection and a better linear dynamic range than DBDI, LTP, and iLTP ion sources in the GC-MS analysis of a series of three perfluorinated compounds. The overall results of the FµTP were similar to those of the iLTP, highlighting the importance of the electrode configuration. The advantages of the FµTP comprise the easier set-up, robustness, and lower gas consumption due to its miniaturization.[24]

A special type of DBDI-based ion source is the “active capillary” plasma source shown in Figure 8. On the left, the “wire electrode”-configuration is similar to that of an LTP, while the “cap electrode”-arrangement on the right has instead a cap electrode at the end of the dielectric tube because the LTP-wire electrode was negatively affected by the discharge gas flow inside the capillary.[84] In this design, the quartz tube does not only function as the dielectric barrier but also as the sampling capillary of the mass spectrometer. The desorption for ambient applications is performed by a laser and the mass spectrometer vacuum is used to transfer the sample molecules through the plasma into the inlet.[85] After further optimization, this ion source became the first commercially available DBD-based ion source which is now termed SICRIT and available from Plasmion GmbH[86].

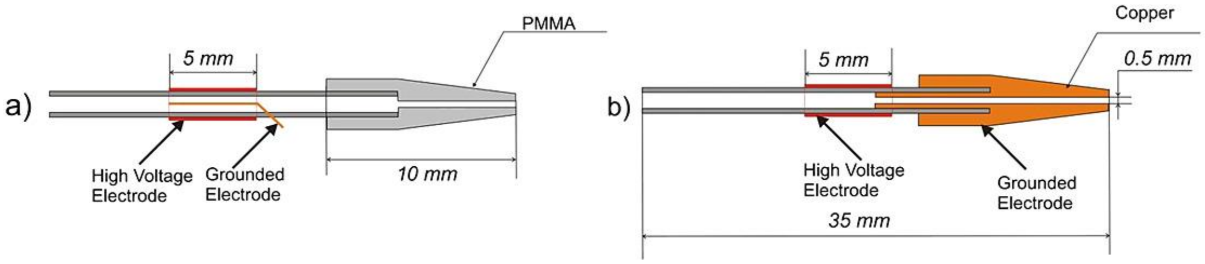

Figure 8: Wire-electrode design (a, left) and cap-electrode design (b, right) of the active capillary plasma ion source developed by Nudnova et al. (2012). Excerpt from [84].

The only other commercially available DBD-based plasma ion source is the DBDI-100 from China Innovation Instrument in Ningbo. It can work with different discharge gases, namely helium, argon, and nitrogen, at varying temperatures between 25 and 250 °C, and at flow rates of 0.2 – 5.0 L min^{-1}.[87] It was used by Li *et al.* (2020) in the direct analysis of chemical warfare agents (CWAs) in soil, bypassing otherwise required time-consuming sample preparation steps[88]. In other studies, a DBDI-100 was coupled to surface plasmon resonance[89] and capillary electrophoresis[90].

The SICRIT ion source is capable of creating a plasma by using air as the discharge gas. Thus, it opens possibilities for on-site analysis which is the ultimate objective of analytical chemistry[91]. One of the obstacles encountered is that all parts of the mass spectrometer have to be appropriately miniaturized. With an LTP ion source and a mobile mass spectrometer, Soprawalla *et al.* (2011) successfully analyzed thiabendazole on orange skins in a supermarket[66]. During the miniaturization of their LTP ion source, Wiley *et al.* (2013) observed a deterioration in signal owed to the use of air instead of helium as discharge gas. In a further study, they improved the ion source by changing the electrode configuration and distances between the mass spectrometer inlet, the plasma source, and the sample.[23, 92, 93] Similar to the SICRIT, the DBDI-based ion source by Kumano *et al.* (2013) had one ring electrode inside the dielectric tube and one outside, and the samples were introduced through the capillary into the mass spectrometer. RF voltage, however, was used for the plasma ignition and the ion source was coupled to a small-size mass spectrometer to allow a hand-held set-up.[94]

Meisenbichler *et al.* (2021) did not employ a handheld mass spectrometer, but their three-in-one ion source was miniaturized to a hand-held pen. This ion source featured DESI, Easy Ambient Sonic-Spray Ionization (EASI), an LTP, and a small camera to provide a visual image of the sample so that both optical and mass spectrometric data could be obtained from a two dimensional surface.[95]

Despite nearly two decades of research and an increasing number of publications demonstrating the advantages of DBD-based ion sources, the availability of commercial products is extremely limited. The resulting incomparability of the many “home-made” ion sources and the lack of systematic optimization methods make it difficult to draw any other conclusion than that the investigation of these types of ion sources is far from reaching its peak. The surpassing of the efficiency of common ion sources like ESI and APCI show the vast opportunity that DBD-based ion sources provide in the field of mass spectrometric detection and the ignorance of the underlying plasma chemistry gives the researchers further motivation to exploit the potential of LTPs.

3.2 Electrospray ionization

Another established and common ionization technique is ESI. While electrospray of high molecular weight molecules was already being researched by Dole and his co-workers[96], Fenn's group is known for being the first to couple it to MS[7, 97], even though Aleksandrov *et al.* (1984) also combined LC and MS in the same year[98] and subsequently produced a series of application publications[99].

In ESI, a liquid is introduced through a hollow steel capillary or needle on which voltage is applied. In the first set-up, from Yamashita *et al.* (1984) in Fenn's group, the spray was guided through an end plate nozzle before reaching the skimmer and the vacuum region of a quadrupole mass spectrometer[7]. They analyzed rather small molecules in positive[7] and negative[97] ion mode, before moving to larger molecules of which also multiple charges via sodium adducts could be detected[100].

The ionization of molecules via electrospray ionization has been extensively researched in the past and can be divided into three steps: the creation of charged droplets at the tip of the capillary, the evaporation of solvent and disintegration of solvent droplets leading to smaller droplets, and the formation of gas-phase ions[101].

There are three models to be considered: In the charged residue model (CRM) proposed by Dole *et al.* (1968), ionic charges are present on the surface of the droplet containing the analyte molecule. When the solvent evaporates, the analyte molecule obtains the charges from the surface of the solvent droplet. In the ion evaporation model (IEM) proposed by Irbaine and Thomson (1976), ions directly leave the droplet as soon as the droplet radius has fallen below 10 nm.[96, 101, 102] The chain ejection model (CEM) considers large proteins that unfold due to external influence, e.g. an acidic LC mobile phase. Due to its hydrophobicity, unfolded chains get to the surface of the droplet and are expelled into the vapor phase. The protein is sequentially ejected and separated from the droplet.[103]

Despite ESI being often considered the gold-standard for polar molecule ionization (cf. Chapter 3.1), there have been made amendments to this technique in order to enhance the ionization process or ion transfer. Besides the reduction of background noise, the sensitivity in ESI is of high importance. It is influenced by the conversion of the molecules into gas-phase ions and how well these ions are transported through the mass spectrometer until detection. This of course depends partially on the mass analyzer and the method of detection.[104] In the present work, the majority of measurements was performed in multiple reaction monitoring (MRM) mode which is optimal for the used triple quadrupole mass spectrometer.

Ion transfer loss is attributed partially to the fact that the bursting molecule-solvent droplet disperses wider than the inlet of the mass spectrometer[105]. Early attempts to improve ion transport were for example the implementation of an ion funnel (under vacuum), referring to a series of ring electrodes whose electric field focuses the ions[106], also in combination with a multi-capillary inlet, meaning parallel steel tubes in a heating block to guide the ions towards the ion funnel and then into the Q0 of the mass spectrometer[107].

In the set-up from Chowdhury *et al.* (1990), the analyte was sprayed through a needle at 4-6 kV and then entered the vacuum region of the mass spectrometer through a metal capillary tube. Instead of a countercurrent to aid the dissolvation, they heated the capillary tube, if necessary, even to temperatures specific for their different analytes, but found their results only comparable to previous publications.[108]

Page *et al.* (2007) found in their ESI-MS set-up that increased inlet capillary temperatures led to smaller droplets and more collisions of charged species with the capillary wall. However, it could not be directly correlated to higher analyte sensitivity. Similar to the previous article, they found different temperatures optimal for different analytes. Additionally, they mentioned that low flow rates create smaller droplets and increase the analyte peak intensity. However, in contrast to the experiments performed for this thesis (50 – 450 µL min^{-1}), in which also the effect of flow rates was investigated, they used flow rates between 0.1 and 2.0 µL min^{-1}.[105]

An improvement also for high flow rates above 200 µL min^{-1} was found by using an off-axis nebulizer instead of an on-axis one which increased the $[M+H]^+$ signal by a factor of over 20[109]. Further endeavors to increase the efficiency of ESI have been undertaken such as investigation of parameters influencing size and velocity of the spray[110] and coupling of two ESI ion sources into one housing[111] or two different ion sources into one housing[112], but detailed analysis of dual ion sources would go beyond the scope of the present thesis.

The implementation of a repeller electrode such as presented in this work was also done by Cristoni and co-workers. Previously, they had performed the analysis of protein ions using an APCI without corona discharge[113]. In order to enhance the signal, they implemented a metallic surface into the ion source housing to which they applied a voltage[114]. This method of ionization was then called surface-activated chemical ionization (SACI) and subsequently optimized regarding the metallic surface geometry, applied potential, solvent type, and sample flow rate[115].

4. Objective

In the first part of this work, a new nebulization system for a previously built inverse low temperature plasma ion source should be developed. For this, two commercial ultrasonic nebulization devices will be studied and modified. In addition, a sprayer, designed by Hitachi High-Technologies, should also be investigated. Custom-made guidance cones to focus the analyte spray onto the plasma plume, as well as heat and auxiliary gas flows will be used to aid the nebulization, evaporation and ionization processes of the analyte molecules in order to improve the sensitivity of the method. The new nebulization method should be compared to a standard nebulizer previously used for APCI, using both the iLTP ion source as well as the TPI configuration.

In the second part of this work, a repeller electrode should be introduced into an ESI ion source and voltage will be applied to it. The created electric field is thought to aid the transfer of the ions towards the inlet of the mass spectrometer. For this, different repeller geometries will be designed and tested, as well as their spatial position and applied voltage optimized first in a step-by-step evaluation via syringe pump continuous injection and then in a design of experiments using an LC-MS set-up. A real application will be done by analyzing reserpine and testosterone in a human plasma matrix with and without repeller electrode. Furthermore, the capability of the repeller electrode to ionize the analyte molecules should be investigated.

In the third part, a plasma ion source should be combined with a nanoESI ion source. The aim is it to couple both ionization types to increase the ionization yield and therefore the sensitivity of the method.

5. Materials and methods

5.1 Chemicals

Caffeine (ReagentPlus ®), testosterone (>98 %), reserpine (>99 %), creatinine (anhydrous, >98 %), Cholecalciferol (Vitamin D3), and DL-phenylalaine (ReagentPlus ®, 99 %) were obtained from SigmaAldrich/ Merck (St. Lois, USA) as powders. Methanol (LC-MS grade) was used from VWR (Darmstadt, Germany) and Thermo Fisher (LC-MS grade) (Waltham, USA) and acetonitrile (LC-MS grade) from VWR (Darmstadt, Germany). Ultrapure water was used from the laboratory system arium® pro VF from Sartorius AG (Göttingen, Germany). Formic acid optima (LC-MS grade) was obtained from Fisher Chemical (Schwerte, Germany). The ESI-L Low Concentration Tuning Mix (G1969-85000) were obtained from Agilent Technologies (Santa Clara, USA). Human plasma (P9523) was obtained from Merck and prepared as indicated in the manufacturer instructions. Argon (99.998 %) and nitrogen (99.999 %) were used from AirLiquide (Paris, France).

5.2 Materials

As syringes, a Hamilton (Reno, USA) 1002RN Gastight Syringe 2.5 mL, fixed needle, blunt needle end, cannula size 22 gauge, needle length 2 inch and an Agilent Technologies 5190-1528 manual syringe 1 mL, fixed needle, bevel tip needle end, cannula size 22 gauge, needle length 50 mm, were used. For the dual ion source experiments, a 50 µL syringe with a blunt tip from Hamilton was used, while in the argon gas flow rate experiment, an identical syringe with a bevel tip was used.

The filter used for the standards in the nanoESI-iLTP experiments was a 0.2 µm PTFE filter (13 mm) from VWR (Darmstadt, Germany).

The column for LC-MS experiments was a Poroshell 120 EC-C18 1.9 µm 2.1 x 50 mm USJSA07941 from Agilent Technologies.

The printing of the guidance cones made from PEEK to aid the nebulization was performed at the 3D-printing facility Co-Creation Lab of the University of Duisburg-Essen in Essen. The guidance cones for the USN made from steel were printed at the 3D-printing facility of the University of Duisburg-Essen 3D DabLab in Duisburg, and the drilling holes were added and the polishing of the cones was performed at the university’s mechanical workshops in Essen.

5.3 Devices

A XS204 DeltaRange balance from Mettler Toledo (Columbus, USA) was used. A single channel syringe pump (PSNE1000) from Prosense B.V. (Munich, Germany) and a LEGATO® 180 syringe pump from kdScientific (Holliston, USA) were used.

Two UPLC systems from VWR (Darmstadt, Germany) were used. One UPLC was equipped with a UV/VIS-detector, the other with a DAD-detector. Both Chromaster Ultra R_S-system had been provided by Hitachi High-Technologies Corporation (Mito, Japan).

The triple quadrupole mass spectrometer MS02a was a prototype developed by Hitachi High-Technologies (Tokyo, Japan). The single quadrupole mass spectrometer used for the dual ion source was a VWR Hitachi Chromaster 5610 by VWR (Darmstadt, Germany).

The Hi-Heater SAH-1PHT (350 W) from the company Hybec (Arlington Heights, USA) and the plastic bottle humidifier from Daiso (Hiroshima, Japan) were provided by Hitachi High-Technologies Corporation. The hi-heater was used in combination with the Hitachi-built USN while the gas supply for the Omron and the humidifier nebulizers was done with a VG flow heater 500 °C by the company Horst (Lorsch, Germany). The Omron (Kyoto, Japan) MicroAIR U100 (NE-U100-E) nebulizer and its single replacement parts were bought from Shop Apotheke Service B.V.

The plasma ion sources used a GHTS 60-high voltage switch from Behlke Power Electronics (Kronberg in Taunus, Germany). A function generator from Telektronics AG1022 (Beaverton, USA) and laboratory power supply unit FUG MPL 1000 10000 from FuG Elektronik GmbH (Schechen, Germany) were also employed.

The nanoESI ion source was re-configured from an OS-3001 DESI Manual Ion Source by Prosolia (Indianapolis, USA) with an emitter from Waters (Milford, USA) made of fused silica and with an inner diameter of 50 µm, an outer diameter of 150 µm, and a length of 40 mm. It was connected via a Tee-piece from Upchurch Scientific (Oak Harbor, USA) to a tubing with 50 µm inner diameter through which the analyte solution was supplied via syringe.

5.4 Softwares

The data was copied from the software *MS02a TQ_MS Control System* of the triple quadrupole mass spectrometer from Hitachi High-Technologies and the software *MSD System Manager* of the single quadrupole mass spectrometer from VWR/ Hitachi.

The statistical evaluation was done with *OriginPro 2020* and *Microsoft Excel*.

OriginPro 2020 was used for the determination of peak areas. If not noted otherwise, the integration of a peak area was based on the following parameters: The median was used as the baseline, the number of local points (the number of consecutive data points that had to be over the defined threshold to count as a peak) was 10, and the threshold height was 100 % (in cases where a visible peak gave no result, this value was reduced to 90 %; if still no peak was found, it was not counted as a peak).

In the case of the Design of Experiments for the USN experiments, the peak area detection was based on retention time because of the wide peak elution caused by the low LC flow rate: the caffeine peaks between 97 – 197 s and the testosterone peaks between 125 – 200 s were evaluated.

The *OriginPro* 2020 extension *Design of Experiments* was used for the design of the experiments procedure, the evaluation of results, and the determination of optimal values.

The evaluation of data from the PDA experiments was also performed with *OriginPro 2020*.

For the computer assisted drawings (CAD), *AutoDesk AutoCAD* 2022, 2023, and 2024 were used.

5.5 Methods

5.5.1 Methods for LTP and USN experiments

The following tables list the parameters used for the measurements with the plasma-based ion sources combined with different types of nebulizers. Furthermore, the set-up for the droplet diameter determination is elucidated.

Table 1: Injection, MS, and USN conditions for the experiments with the Omron nebulizer if not noted otherwise.

Syringe pump parameters		**MS parameters**	
Flow rate:	100 µL min^{-1}	**Ion source:**	iLTP
Standard:	50 µg L^{-1} reserpine in MeOH	**IS 1 HV:**	0 kV
USN parameters		**IS heater:**	-
Nitrogen auxiliary gas flow rate:	0.5 L min^{-1}	**AP1 heater:**	200 °C
Nitrogen auxiliary gas temperature:	150 °C	**Nebulizer (Neb.) gas:**	3 L min^{-1}
		Auxiliary (Aux.) gas:	2 L min^{-1}
		Counter gas:	2.0 L min^{-1}
		Collision gas:	0.7 L min^{-1}
		Acquisition method:	Q1Sweep

Table 2: LC, MS, and USN conditions for the experiments with the humidifier nebulizer if not noted otherwise.

LC Parameters			**MS parameters**	
Column:	Agilent Poroshell 120 EC-C18 1.9 µm 2.1 x 50 mm USJSA07941		**Ion source:**	iLTP
Solvent A:	H_2O + 0.1 % FA		**IS 1 HV:**	0 kV
Solvent B:	MeOH + 0.1 % FA		**IS heater:**	200 °C
Flow rate:	200 µL/ min		**AP1 heater:**	200 °C
Method:	Time (min)	A (%)	**Neb. gas:**	1.8 L min^{-1} (2.2 L min^{-1} for analyte flow rate tests)
	0	95	**Aux. gas:**	2.0 L min^{-1}
	3	95	**Counter gas:**	2.0 L/ min
	10	5	**Collision gas:**	0.7 L/ min
	10.5	95	**Acquisition method:**	Q1Sweep, *m/z* 100-800
Injection volume:	10 µL		**Syringe pump**	
Oven temperature:	40 °C		**Flow rate:**	30 µL min^{-1}
Standard:	differs			

USN parameters	
Nitrogen auxiliary gas flow rate:	1.8 L min^{-1}
Nitrogen auxiliary gas temperature:	180 °C

Table 3: LC, MS, and USN conditions for the Hitachi with nebulizer cones A and B.

LC Parameters			**MS parameters**	
Column:	Agilent Poroshell 120 EC-C18 1.9 µm 2.1x50 mm USJSA07941		**Ion source:**	iLTP
Solvent A:	H_2O		**Cone:**	A, B
Solvent B:	ACN		**IS 1 HV:**	0 kV
Flow rate:	100 µL/ min		**IS heater:**	-
Method:	time [min]	A [%]	**AP1 heater:**	200 °C
	0	30	**Neb. gas:**	Used for USN cooling gas
	3	2	**Aux. gas:**	Used for USN heated gas
	5	2	**Counter gas:**	2.0 L/ min
	5.5	30	**Collision gas:**	0.7 L/ min
	8	30	**Collision energy:**	35 eV for caffeine 35 eV for testosterone
Injection volume:	10 µL		**Acquisition method:**	MRM (Q1 sweep for blank measurements)
Oven temperature:	40 °C		**Transitions:**	*m/z* 195.1 → 138.1 for caffeine *m/z* 289.2 → 109.1 for testosterone
Standards:	For cone comparison: 1mg L^{-1} caffeine, reserpine, testosterone in 95 % H_2O, 5 % ACN For cone B heater test and DoE: 1 mg L^{-1} caffeine, reserpine testosterone in 30 % H_2O, 70 % ACN For FoM: 1.5, 15, 30, 60, 100, 150, 300, 600, 1200 µg L^{-1} in 30 % H_2O, 70 % ACN			

USN parameters	
Cooling gas flow rate:	As indicated below
Heated gas flow rate:	As indicated below
Heated gas temp.:	300 °C
Heating cartridges temp. for B:	For cone comparison, cone B heater test: 90 °C For DoE, FoM: 110 °C
Use of ceramic insulator for B:	For cone comparison, cone B heater test: no For DoE, FoM: yes
Piezo-element controller power	4 W

Phase Doppler Anemometry (PDA) is a means to determine droplet velocity and size. In cooperation with the NanoEnergieTechnikZentrum of the University of Duisburg-Essen in Duisburg, PDA measurements could be performed on the droplets produced by the Omron and the Daiso humidifier mesh. The set-up is shown for the humidifier mesh in Figure 9. This set-up is connected to a nitrogen gas heater. The focal point of the lasers is situated slightly below the exit of the USN cone and is the point of measurement. The analyte in this experiment was methanol supplied by a syringe pump.

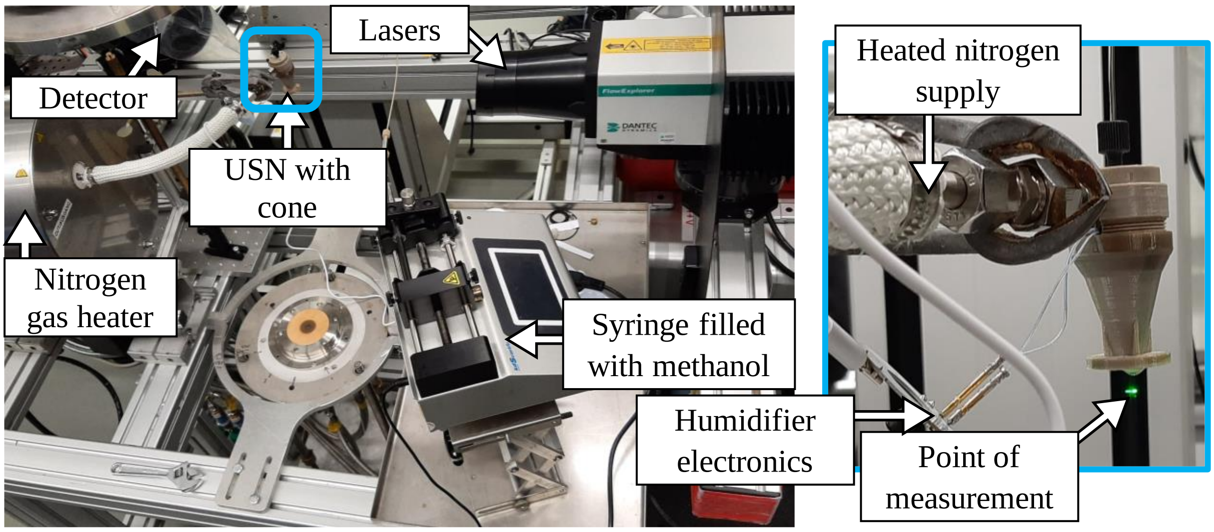

Figure 9: Experimental set-up of the humidifier USN with cone for a PDA measurement.

5.5.2 Methods for ESI experiments

The following tables list the parameters used for the experiments that employ a repeller electrode in order to enhance the analyte signal intensity for ESI-MS.

Table 4: Parameters of optimization measurements via syringe pump injection.

MS parameters		**Standard**
Ion source:	ESI	35 µg L^{-1} caffeine
IS H1 HV:	4 kV	25 µg L^{-1} reserpine
IS heater:	400 °C	35 µg L^{-1} testosterone
AP 1 heater:	200 °C	200 µg L^{-1} vitamin D3
Neb. gas:	3 L min^{-1}	1 mg L^{-1} phenylalanine
Aux. gas:	16 L min^{-1}	1 mg L^{-1} creatinine
Counter gas:	5.0 L min^{-1}	in 50:50 H_2O:MeOH with 0.1 % formic acid and approx. 7 mol L^{-1} ammonium formate
Collision gas:	0.7 L min^{-1}	
Scan mode:	Q1Sweep	

Syringe pump parameters	
Syringe pump flow rate	50 µL min^{-1}
Syringe type	Hamilton 2.5 mL syringe

Table 5: Parameters of measurements via LC-MS injection.

LC Parameters			**MS parameters**		
Column:	Agilent Poroshell 120 EC-C18 1.9 µm 2.1x 50 mm USJSA07941		**Ion source:**	ESI	
Solvent A:	H_2O with 0.1 % FA and approx. 7 mol L^{-1} AF		**IS H1 HV:**	4 kV	
Solvent B:	MeOH with 0.1 % FA and approx. 7 mol L^{-1} AF		**IS heater:**	400 °C	
Flow rate:	450 µL min^{-1}		**AP 1 heater:**	200 °C	
Method:	B (%)	Time (min)	**Neb. gas:**	3 L min^{-1}	
	5	0	**Aux. gas:**	16 L min^{-1}	
	5	0.5	**Counter gas:**	5.0 L min^{-1}	
	100	5.5	**Collision gas:**	0.7 L min^{-1}	
	100	7.5	**Scan mode:**	MRM	
	5	7.51			
	5	10			
Injection volume:	10 µL				
Oven temperature:	40 °C				
Standard			**MRM transitions**		
			Q1 (m/z)	**Q3 (m/z)**	**CE (eV)**
35 µg L^{-1} caffeine			195.1	138.1	30
25 µg L^{-1} reserpine			609.3	195.1	75
35 µg L^{-1} testosterone			289.2	97.1	50
200 µg L^{-1} phenylalanine			166.2	120.2	15
200 µg L^{-1} creatinine			114.1	114.1	5
in 95:5 H_2O:MeOH					

Table 6: Parameters of the flow rate investigations.

MS parameters		**Mobile phase (analyte)**	
Ion source:	ESI	35 µg L^{-1} caffeine	
IS H1 HV:	4 kV	25 µg L^{-1} reserpine	
IS heater:	400 °C	35 µg L^{-1} testosterone	
AP 1 heater:	200 °C	200 µg L^{-1} vitamin D3	
Neb. gas:	3 L min^{-1}	1 mg L^{-1} phenylalanine	
Aux. gas:	16 L min^{-1}	1 mg L^{-1} creatinine	
Counter gas:	5.0 L min^{-1}	in 50:50 H_2O:MeOH with 0.1 % formic acid and approx. 7 mol L^{-1} ammonium formate	
Collision gas:	0.7 L min^{-1}	**LC flow rate:**	varied
Scan mode:	Q1Sweep	**Column:**	None

Table 7: Parameters of the measurement with the APCI nebulizer without needle and different repellers.

MS parameters		**Standard**	
Ion source:	varied	35 µg L^{-1} caffeine	
IS H1 HV:	APCI: 3 kV ESI: 4 kV	25 µg L^{-1} reserpine	
IS heater:	400 °C	35 µg L^{-1} testosterone	
AP 1 heater:	200 °C	200 µg L^{-1} vitamin D3	
Neb. gas (APCI):	2 L min^{-1}	1 mg L^{-1} phenylalanine	
Neb. gas (ESI):	3 L min^{-1}	1 mg L^{-1} creatinine	
Aux. gas (APCI):	2 L min^{-1}	0.1 % formic acid	
Aux. gas (ESI):	16 L min-^{1}	dissolved in 50 : 50 H_2O : MeOH	
Counter gas:	5.0 L min^{-1}	**LC flow rate:**	200 µL min^{-1}
Collision gas:	0.7 L min^{-1}	**Column:**	None
Scan mode:	Q1Sweep		

5.5.3 Methods for nanoESI-iLTP coupling experiments

The following table lists the unchanged parameters used for the experiments in which either the nanoESI or the nanoESI in combination with a plasma ion source were employed. All other parameters are listed individually for the respective experiments.

Table 8: Parameters of the measurement with the nanoESI and/ or a plasma ion source.

MS parameters		**Standard**	
AP1 voltage:	80 V	1 mg L^{-1} caffeine, reserpine, and testosterone in MeOH + 0.1 % formic acid, filtered through a 0.2 µm PTFE filter (13 mm)	
AP2 voltage:	30 V		
Ion source temperature:	70 °C	**Syringe pump flow rate:**	500 nL min^{-1}
AP1 temperature:	120 °C	**Column:**	None
Dwell time:	500 ms		
Scan speed:	Normal		

The spatial position of the nanoESI probe was defined through an xyz-table. The spatial position and the required ESI voltage had to be readjusted from time to time and will therefore be noted further below for each measurement. The plasma ion source parameters were optimized to a frequency of 12.5 kHz, a pulse width of 50 µs, a flow rate of 80 mL min^{-1} argon gas and a plasma voltage of 1.8 kV.

5.6 Low temperature plasma-based ion sources

A previously built homemade iLTP ion source[35, 57], shown in Figure 10, was used. In brief, a stainless steel needle of approximately 0.4 mm diameter and a pointy tip was screwed onto a modified high voltage plug and served as the needle electrode. It is engulfed by a quartz tube with an inner diameter of 0.6 mm and an outer diameter of 1.2 mm which is fixed by a ferrule in a Tee-piece and which functions as dielectric barrier. The discharge gas argon is supplied from a top channel into the T-piece. The stainless steel ring electrode is pushed over the dielectric and connected to the ground of the HV plug.

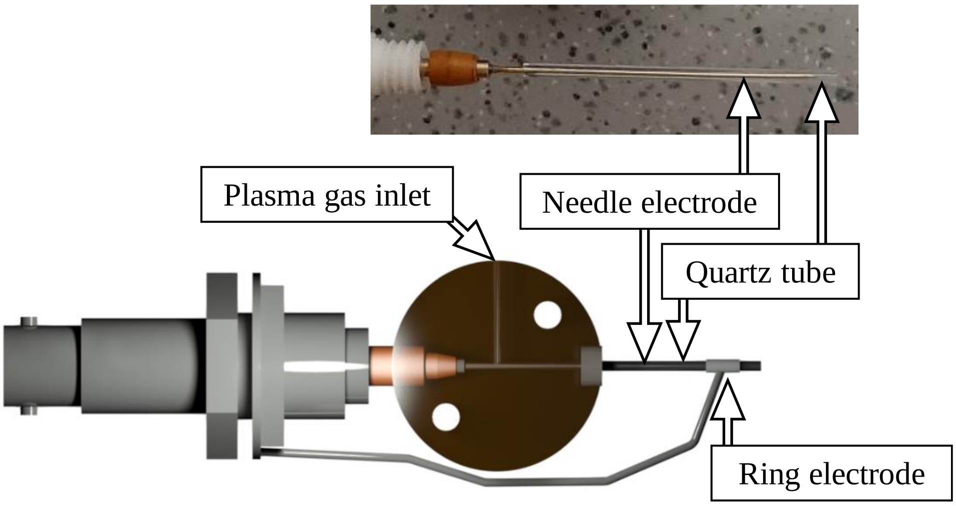

Figure 10: CAD of the home-made iLTP ion source and a photo of a partially disassembled iLTP ion source used by Brecht et al. (2020).[57]

The iLTP was driven by AC voltage and ignited at a frequency of 10 kHz and a pulse width of 50 µs. Ignition occurred, depending on the ambient conditions, between 1.8 and 2.5 kV. After ignition, the frequency was changed to 12.5 kHz and the pulse width to 2 µs, and operation of the iLTP was performed using 2.4 kV. The argon discharge gas flow rate was 200 mL min^{-1}.

For the TPI-configuration, the ring electrode and the connecting wire were unscrewed from the HV plug holder. The difference can be seen in Figure 11. The TPI was operated at the same frequency and pulse width conditions. All parameters were kept identical, except for the voltage which had to be 3 kV in order for the plasma not to be extinguished. However, the voltage and argon plasma flow at which ignition occurred and time until ignition varied from day to day.

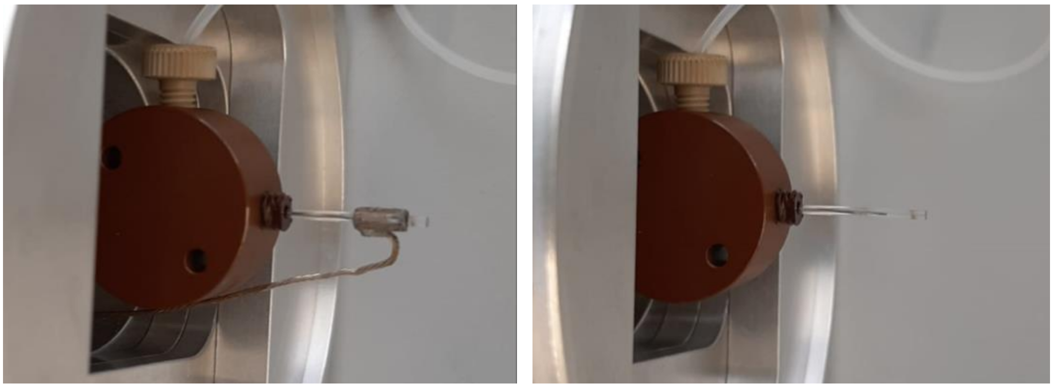

Figure 11: Ion source in iLTP- (left) and TPI-configuration (right).

For the coupling to nanoESI, an FµTP ion source based on Brandt *et al.* (2018) was developed as seen in Figure 12. A GC capillary served as dielectric barrier and was supported by a tube sleeve. Like the other plasma ion sources in our laboratories, it was operated with argon gas. The interior needle electrode, a tungsten wire, was bound around an HV plug (in contrast to a screwing connection as used in the above mentioned iLTP/ TPI configurations). Argon entry, needle electrode and dielectric were connected through a Tee-piece as seen in Figure 10 but using smaller tunnels.

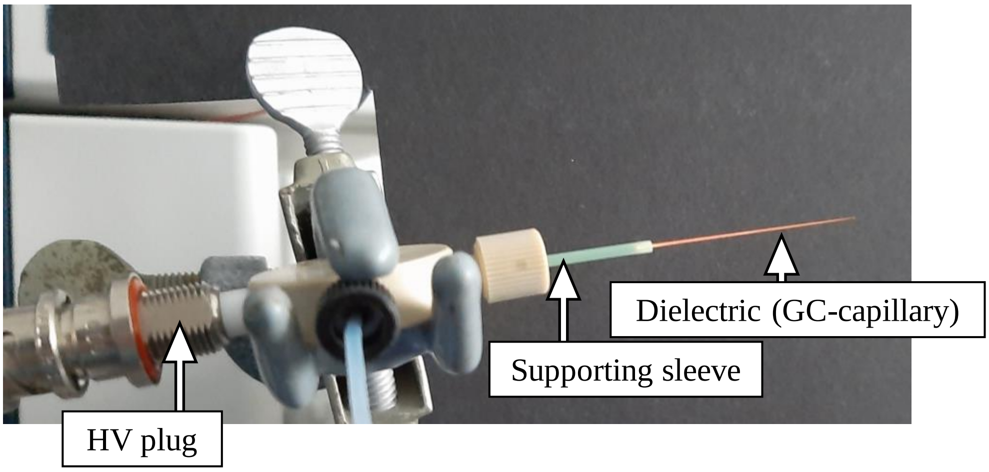

Figure 12: Ion source design based on the FµTP but with a stabilizing supporting sleeve for the dielectric and operated with argon gas.

6. Results and Discussion

6.1 Developing an ultrasonic nebulization system for a low temperature plasma ionization source

In order to transport the molecules eluting from the LC into gas phase, a nebulizer is used to spray and evaporate the liquid into the ionization region. The aim of this project was it to enhance the nebulization which was previously being performed using a standard APCI nebulizing device for the iLTP ion source of the MS02a. An issue was probably the large droplet size and the high velocity of the droplets which was thought to impede proper ionization in the plasma region of the iLTP ion source. Ultrasonic nebulization was to be used to improve the droplet size and drying process of the droplets and to slow the velocity with which the analyte molecules pass the plasma region. For the nebulization of the analyte in the solvent, different approaches were tested. At first, two commercial products, a medical inhalation device and a room humidifier, were taken apart and re-built for the following study. Based on these results, a spraying system was developed by Hitachi High-Tech, with which a Design of Experiments (DoE) and a determination of Figures of Merit (FoM) were executed. For the room humidifier and for the Hitachi nebulizer, custom guidance cones to aid the focusing and heating of the spray were designed and constructed.

Omron nebulizer

The first type of nebulizer built for the iLTP ion source in this project was based on the commercial mesh nebulizer “MicroAIR U100 (NE-U100-E)” by OMRON, which can be seen in Appendix Figure 69 (left). In its normal application, the Omron MicroAIR nebulizer is a device used in the medical field. The medicine is filled into a small tank and when the device is activated, the liquid is pushed through a vibrating mesh (a metal plate with tiny holes) and nebulized, so that it can be inhaled by the user.

The interior parts of the Omron MicroAIR nebulizer were disassembled (Appendix Figure 69). In order to withstand the elevated temperatures applied to the set-up, the holding pieces of the mesh, which consisted originally of polycarbon and silica, were re-designed from more heat-resistant materials, namely polyimide and PEEK. In the Omron itself, a piezo-element, a piece of metal which deforms when voltage is applied, is glued to a titanium piece. Its oscillating against the metal mesh is what brings the mesh itself to vibrate. The extracted parts were then arranged as shown in Figure 13 (and Figure 15 left) so that the liquid could enter the system through a needle between the piezo-element and the vibrating mesh and be sprayed upwards through the metal piece.

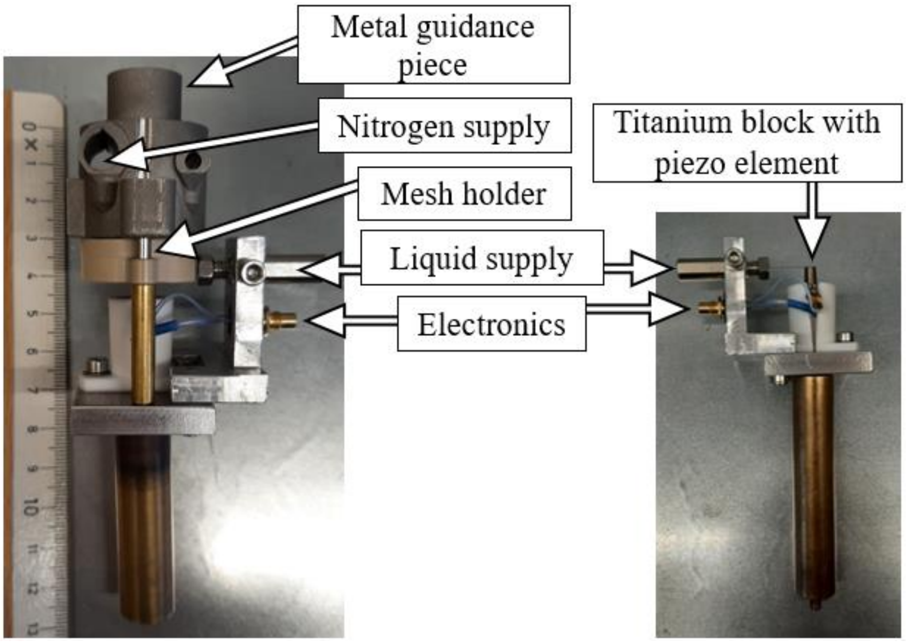

Figure 13: "Extracted Omron" with metal holder and PEEK mesh holder (left) and without metal holder and mesh holder (right).

Heated nitrogen auxiliary gas was supplied through a heating drum into the metal piece. The entire set-up was placed upside down on top of the ion source housing (Appendix Figure 70).

Measuring caffeine and reserpine via continuous injections, different values for nitrogen temperature (set: 50 – 350 °C), flow rate (0 – 5 L min^{-1}), and solvent composition (MeOH, H_2O, MeOH/ H_2O) were tested (cf. Table 1). However, the solvent could not be heated sufficiently to ensure complete transfer into the gas phase due to heat loss of the gas leaving the gas heater. During the course of a measurement day, especially with high water contents in the mobile phase during LC gradient runs, the humidity in the ion source housing increased, condensing droplets formed at cold spots and as a result arcing occurred, i.e., electric short circuits between the wet metal piece of the nebulizer and the ring electrode of the iLTP. This would often lead to the extinguishing of the plasma. Furthermore, the vibration mode of the mesh was not regular, and the pulsing could be seen in the chronograms like Figure 14 which complicated peak evaluation.

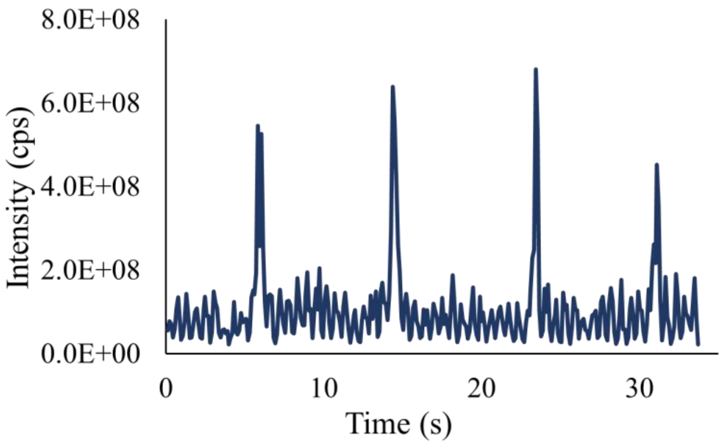

Figure 14: Chronogram of 50 µg L^{-1} *reserpine in methanol measured with Omron-iLTP-MS in Q1Sweep (full scan mode). All further measurement parameters are found in Table 1.*

Another issue was the constant hitting of metal (titanium block) on metal (mesh) with the metal needle in between which would lead to damage of the material. Even when a small channel was made in the titanium piece into which the needle was placed, this problem could not be diminished.

Therefore, a new method of nebulization had to be found.

Bottle humidifier

Similar to the Omron nebulizer, the mesh and its electronics were extracted from commercial bottle humidifiers of the brand Daiso. The disassembly procedure can be found in Appendix Figure 71. The main difference between the two nebulizers is that, in the case of the bottle humidifier, the metal plate containing the mesh is a piezo element itself and the voltage is applied directly to it for the vibration. The advantage is that there is no constant metal-on-metal interaction to wear out the metal mesh as it had proven a disadvantage in the Omron nebulizer. Furthermore, the nitrogen auxiliary gas was not supplied from one side through the metal piece anymore but in circular tubes inside a PEEK holding piece around the mesh as seen in Figure 15 and in Appendix Figure 72.

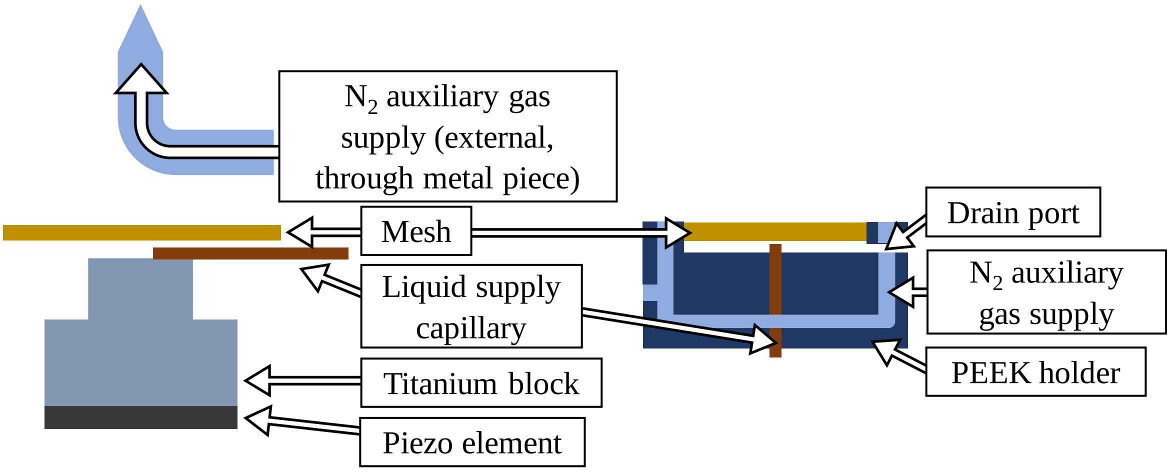

Figure 15: Working modes of the mesh nebulization: In the Omron nebulizer, a piezo-element externally vibrates the mesh (left), while in the bottle humidifier, the mesh itself is brought to vibrate (right).

Figure 16 below shows the extracted humidifier pieces in the set-up which was integrated from either the top or the side into the ion source housing.

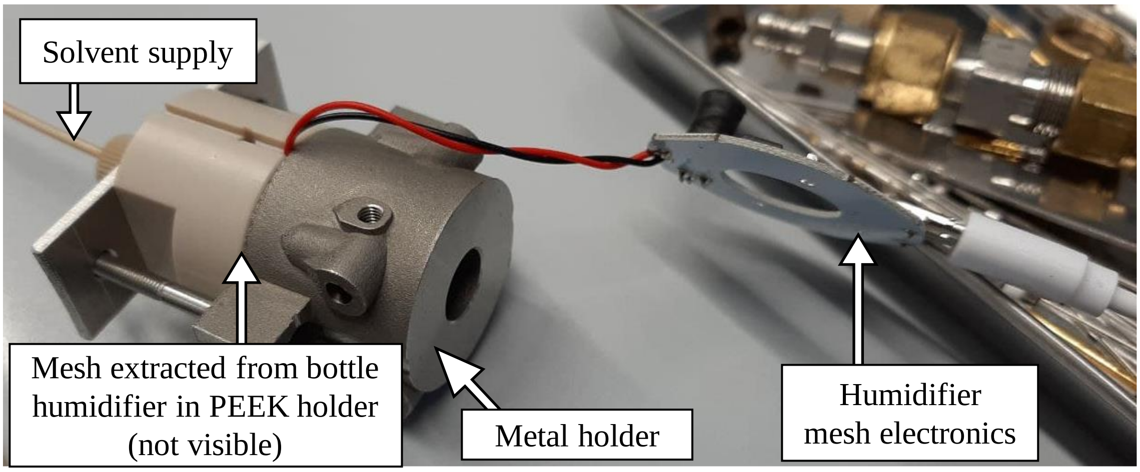

Figure 16: Extracted parts of the bottle humidifier incorporated into a new set-up to implement into the ion source housing as well as to provide heated auxiliary gas by the metal holder piece.

As before, arcing was a re-occurring problem. To reduce the humidity, long periods of high-water content in the mobile phase were avoided. Instead of the above-shown metal piece, a so-called focusing cone made from PEEK was developed for better focusing of the solvent into the plasma region and also to avoid electric short circuits between metal parts (Figure 17 and Appendix Figure 72).

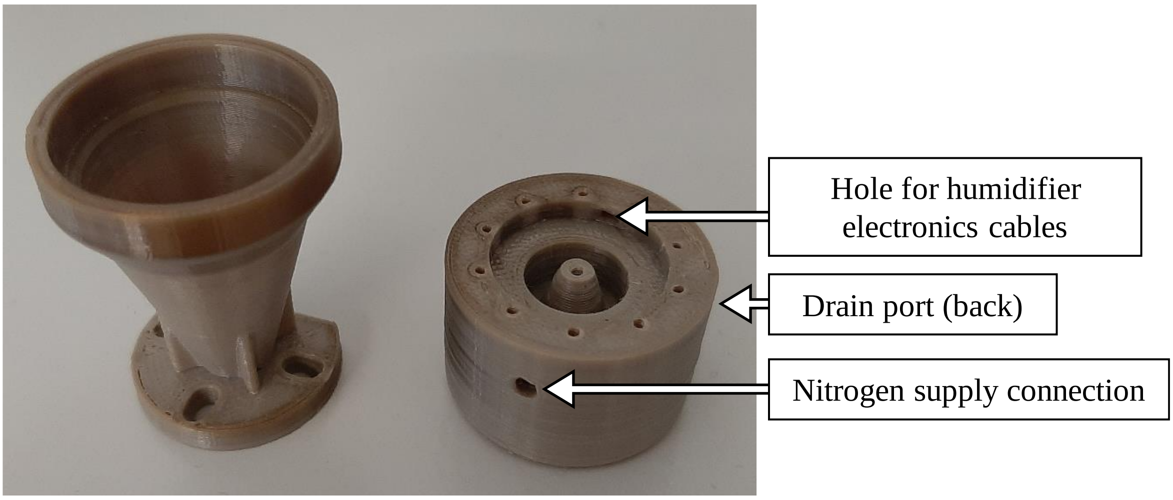

Figure 17: PEEK focusing cone for the extracted humidifier set-up. A system of internal tubes guides the auxiliary nitrogen gas to exit holes around the spray, helping with the dispersion of the sprayed droplets.

While this cone would have been able to focus the analytes better onto the plasma region through a narrowing nozzle, it could not be heated and could also only withstand auxiliary gas temperatures up to 250 °C. Therefore, it was inserted into the previously used APCI nebulizing system which contained heating plates (Figure 18). The APCI spraying parts were extracted and instead, the humidifier sprayer was put into the same position. This also circumvented the issue of the gas heater which could not – despite isolation of the connection tube – supply nitrogen of sufficient temperature into the USN set-up. However, even though the guidance cone was designed to focus the spray better onto the plasma by the narrowing nozzle, attachment of the APCI heater plates led to the spray exiting through the APCI sprayer tube.

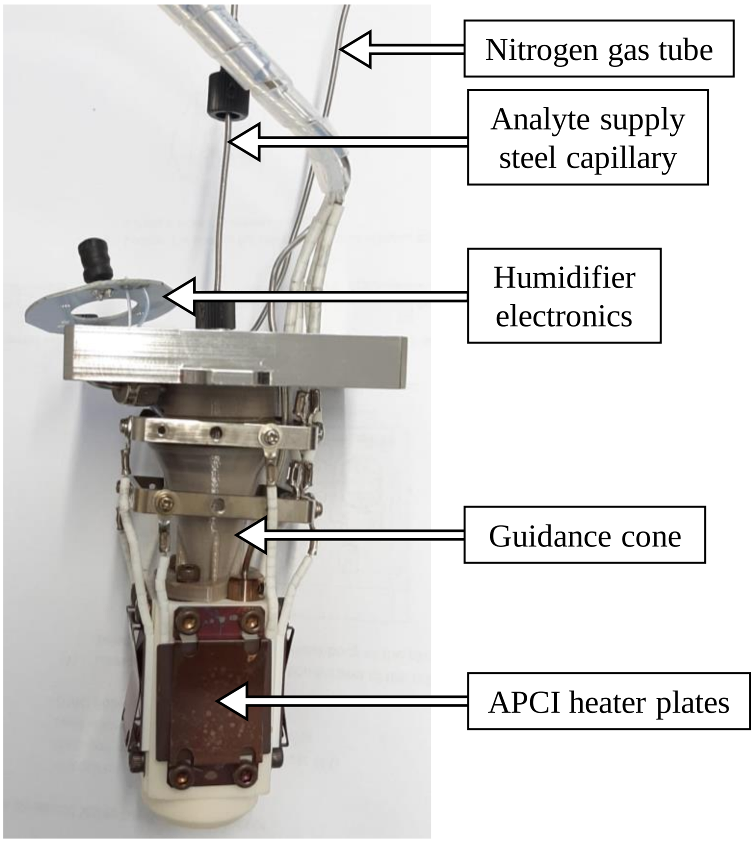

Figure 18: Focusing cone and extracted humidifier implemented into the top of a standard APCI nebulizer.

The length of the capillary protruding the PEEK holder and the strength with which the capillary pushed against the vibrating mesh were found to be a critical parameters. To avoid movement of the capillary inside the PEEK holder, a steel capillary was used instead of a PEEK capillary. Another important feature in this set-up was the connection of a plastic tube serving as drain port which allowed accumulating liquid in the holder-piece to flow outside and thus avoid the risk of an electrical short circuit. This set-up could now be mounted onto the ion source housing either from the side or from the top (Appendix Figure 73).

Different flow rates were tested to not flood the mesh and prevent adequate spraying. Despite the normal working conditions of the humidifier advertised by its manufacturer Daiso being 330 – 500 µL min^{-1}, the following experiments used flow rates of 30 µL min^{-1} to avoid wasting analyte solution through the drain port.

The temperature of the nitrogen heating and its flow rate were further parameters to be optimized. The nitrogen flow rate was increased in 0.2 L min^{-1} steps. A nitrogen flow rate under 1.2 L min^{-1} was found to be insufficient to deliver the analyte to the ionization region, and a flow rate over 2.4 L min^{-1} resulted in the baseline of the chronogram to show irregularities. During normal operations of the iLTP with the standard APCI nebulizer, the APCI heating plates apply temperatures of up to 400 °C. The USN plastic cone, however, could not withstand temperatures over 250 °C. Therefore, the maximum temperature to be applied safely when having the USN incorporated into the set-up was 220 °C. Thus, 180, 200 and 220 °C were tested. All further parameters can be found in Table 2.

Despite precautions and optimization, the pulsating of the mesh was as much a problem with the humidifier as with the Omron. This might be because both devices were not built for continuous use. Due to the accumulation of eluent, peaks in the mass spectrum during such a pulsation would lead to a signal intensity of nearly ten times as much as in the average of a smooth working mesh period (cf. Figure 19).

The mentioned vibration irregularities of the mesh made the interpretation of averaged mass spectra difficult, and if possible, the inclusion of such peaks in the averaging process was avoided. Unfortunately, the results suffered from big standard deviations (up to 59 %) which often impaired the finding of trends in the influences of the tested parameters. Nevertheless, it could be determined that the mounting of the USN on top was advantageous in comparison to the assembly from the side as it was found that a tenth in concentration resulted in similar peak intensities for the top configuration as in the side configuration (cf. Appendix Figure 74). In the top configuration, more analytes pass the plasma due to gravity, which might explain the higher intensities. For the side configuration, the bent trajectory of the analytes would require optimal conditions (velocity, aided by the nitrogen flow rate) to pass into the ionizing plasma region and subsequently be drawn into the mass spectrometer inlet. Therefore, further studies were undertaken with the configuration from the top. As the nitrogen flow appeared stable between 1.6 and 2.0 L min^{-1}, it was continued with a flow rate of 1.8 L min^{-1} and an APCI heater temperature of 200 °C (cf. Appendix Figure 74).

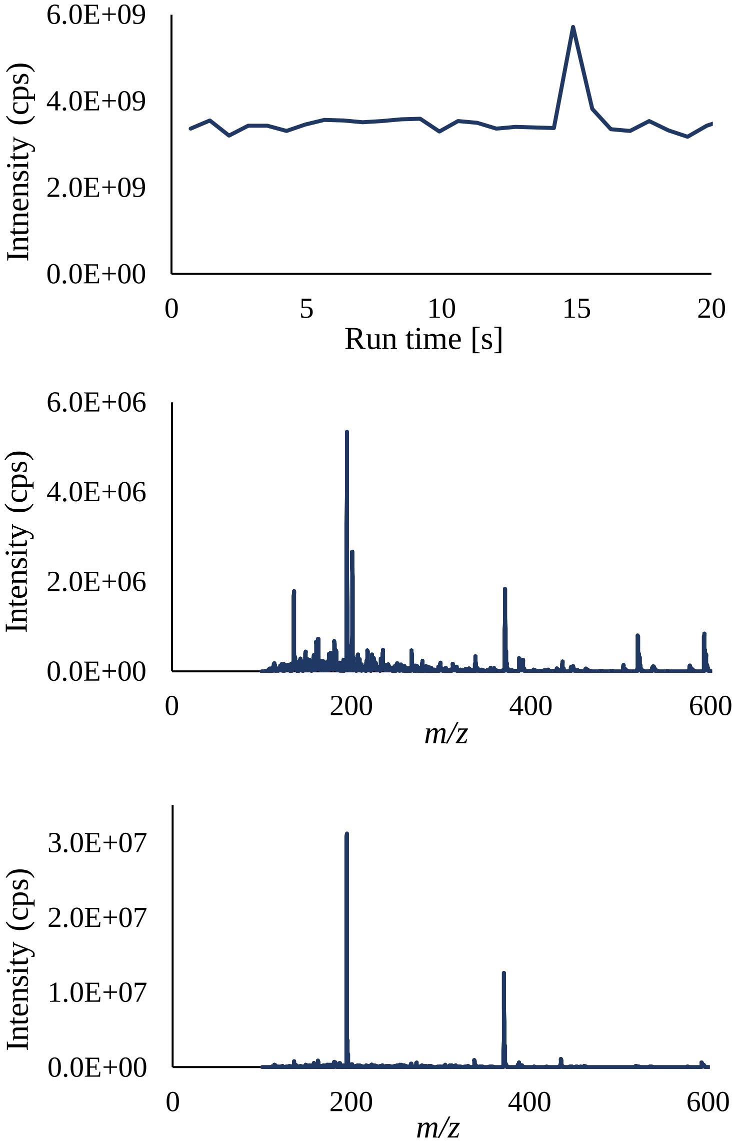

Figure 19: 100 µg L^{-1} caffeine in MeOH via continuous injection at 30 µL min^{-1} measured in full scan mode (Q1Sweep), with nitrogen gas flow rate 1.8 L min^{-1}, IS heater temperature 180 °C, and humidifier-USN on the top of the iLTP ion source housing. All further measurement parameters can be found in Table 2. Top: Example chronogram of the total ion chronogram (TIC) illustrating the irregular working mode of the mesh. Middle: Mass spectrum averaged from 2 – 13 s, a regular vibration period, in the chronogram. The caffeine peak has an intensity below 6.0x10^{6} counts per second. Bottom: Mass spectrum in the peak maximum of the peak visible in the chronogram on top at around 15 s. The caffeine peak has an intensity over 3.0x10^{7} counts per second.

In the next step, the UPLC was coupled to the USN-iLTP-MS and a solution containing 100 µg L^{-1} caffeine and 500 µg L^{-1} reserpine was successfully measured in triplicates with a gradient elution (cf. Table 2). The residual standard deviation (RSD) for the two substances were 8 and 10 %, respectively (cf. chromatograms in Appendix Figure 75). However, the irregular working mode of the mesh posed a continual problem and several dry experiments also showed that the efficiency of the spray depended on the distance between the steel capillary of the liquid supply and the mesh. If the distance was too big, liquid would gather on the mesh and be sprayed either not at all or in bulks. If the steel capillary was firmly pressed against the mesh, the metal plate would break or become damaged over time. Therefore, the liquid application was a major point in the development of the next nebulizer system.

Droplet sizes

The aim to reduce the droplet size could only be partially achieved, as measurements of the Omron and humidifier spray via phase doppler anemometry (PDA) demonstrated. PDA is an analysis tool for particle velocity, size, and temperature. It is based on laser doppler anemometry in which two lasers are arranged in a defined angle and the measurement takes place in the intersection point of these (cf. Appendix Figure 76). The size of the measuring point depends on the angle of the lasers and the focusing lenses. Once a particle passes the measuring point, the light is scattered and forms a particular interference pattern depending on the velocity of the particle. In PDA, the detectors of both lasers also generate signals called Doppler bursts, based on the measured particle. While their frequency is the same, the phases of the signals depend on the angle in which the detectors are placed to each other and the diameter of the – assumed – spherical particle.

The number of droplets measured has an influence on the accuracy of the measurement, which is why in the present investigation, the measurement was stopped when a defined number of data points had been gathered. One difficulty encountered recording the droplet sizes are apparent bi- or trimodal distributions shifted to higher droplet sizes which may lead to misguided interpretations, as seen in Figure 20 (left). Koo *et al.* (2003) thus suggested to fix the highest measured droplet size at twice the value of the expected highest droplet diameter. Since the expected droplet size is approximately 10 µm, data points above 20 µm are not considered.[116-120]

The nitrogen gas flow rate, the methanol liquid flow rate and the nitrogen temperature were varied for both the modified Omron and the humidifier nebulizers, but in most cases without significant effect. The nitrogen exiting the heating device cooled down rather quickly despite the heat-insulated transfer line which had a negative effect on both this experiment and also on the LC-MS experiments which had been mentioned above. However, it could be determined that for the Omron nebulizer it was found that an increase in temperature led to an increase in droplet velocity (Appendix Figure 77), and for the humidifier it could be determined that the droplet velocity increased with inreasing nitrogen flow rate (cf. Appendix Figure 78). However, the influence of the temperature on the droplet size remained inconclusive, which may mainly be due to heat loss in the transfer line of the nitrogen heater which led to the temperature at the cone entry to be very low in comparison to the set temperature. The droplet size for the modified Omron nebulizer was found to be distributed below 10 µm as shown exemplary in Figure 20 (left). For the modified humidifier, the droplet size varied between 8 and 14 µm (right).

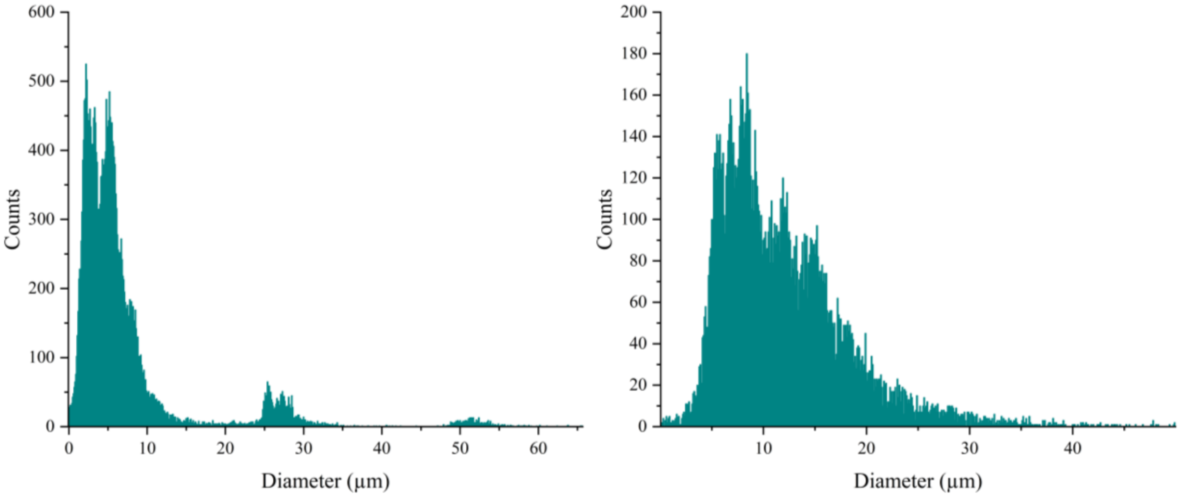

Figure 20: Droplet size distribution measured with the modified Omron nebulizer with 200 µL min^{-1} methanol flow rate, set 2.5 L min^{-1} nitrogen gas flow rate, and a set temperature of 50 °C (left), and with the modified humidifier nebulizer with 200 µL min^{-1} methanol flow rate, 1.2 L min^{-1} nitrogen gas flow rate and a set temperature of 25 °C (right).

Figure 21 shows the distribution of droplet sizes for the unmodified Omron (left) as well as the experimental set-up of the Omron measurement (right). The median droplet size is around 5 µm. However, in this experiment, water was dispersed instead of methanol as the unmodified Omron nebulizing device only worked with water solutions.

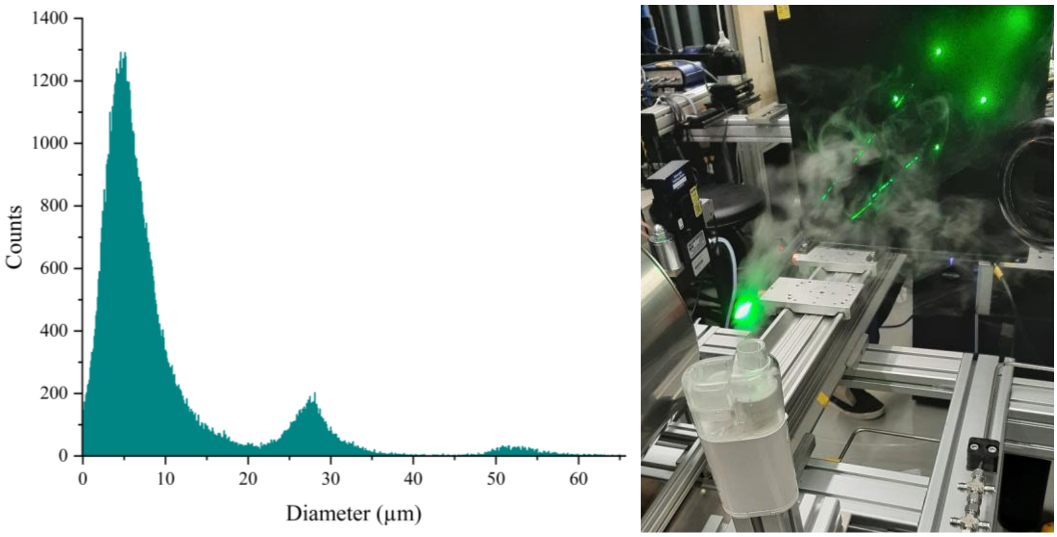

Figure 21: Droplet size distribution of the unmodified Omron nebulizer (left) and experimental set-up of the experiment (right). Here, water was used instead of methanol.

As a comparison, Dobrowolska *et al.* (2020) found droplets between 1 and 5 µm for their pneumatic and vibrating-mesh nebulizers[121], but this depends on the position of measurement, mixing auxiliary gas, and temperature. Tsai *et al.* (2017) showed a distribution for droplets of a similar Omron nebulizer between 1 and 20 µm, with the median being approximately at 5 µm[122].

Hitachi nebulizer

Based on the previously mentioned drawbacks of both the Omron and the bottle humidifier nebulizers, our cooperation partner Hitachi High-Tech Corporations developed a new type of USN-based spraying device.

In the previous designs, a critical parameter for the working mode of the set-up was the distance between the solvent-supplying steel capillary and the vibrating piezo-mesh (cf. Figure 15). In the new design, the liquid is guided through a channel inside a metal plate. The metal plate consists of three layers and in the middle layer, a channel is built. In the middle of this channel, a small mesh is incorporated in the top layer, as shown in the side-view in Figure 22. A three-dimensional view for further visualization is given in Appendix Figure 79. The piezo-element has to be firmly pressed against the metal plate, and when it vibrates and comes into rapid contact with the middle of the metal plate, it pushes the solvent, which is flowing through the channel, through the mesh in the top layer where it disperses into fine droplets, generating the plume seen in Figure 23.

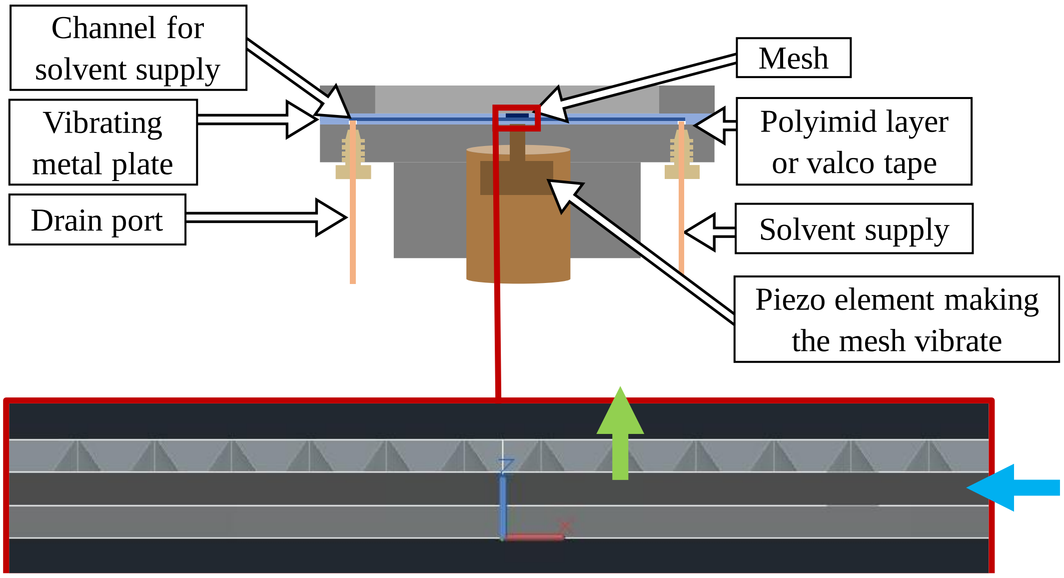

Figure 22: Side view of the metal plate of the Hitachi nebulizer: the liquid flows through a channel in the middle layer (blue arrow). The middle of the metal plate contains a mesh with conical holes with exit diameters of 0.02 or 0.05 mm. Through contact with a vibrating piezo element, the middle of the metal plate is brought to vibrate, leading to the liquid to be sprayed through the mesh (green arrow).

Figure 23: Operating Hitachi nebulizer: 300 µL min^{-1} *methanol was supplied through the PEEK capillary and the piezo-element was operated at 4 W.*

As a focusing cone to direct the spray onto the plasma plume had already proven helpful for the humidifier set-up, a new cone for this type of USN was developed as well, seen in Figure 24. This cone was 3D-printed and contained, similarly to the previous cone, a torus-shaped hole with an inlet as well as several exit tubes for the nitrogen auxiliary gas. A main advantage is that this cone was made from stainless steel and had no restrictions regarding the applied heat. This cone was placed on top of metal plates that could be moved in x-z-position on the ion source housing, guaranteeing optimal positioning of the cone on top of the plasma jet.

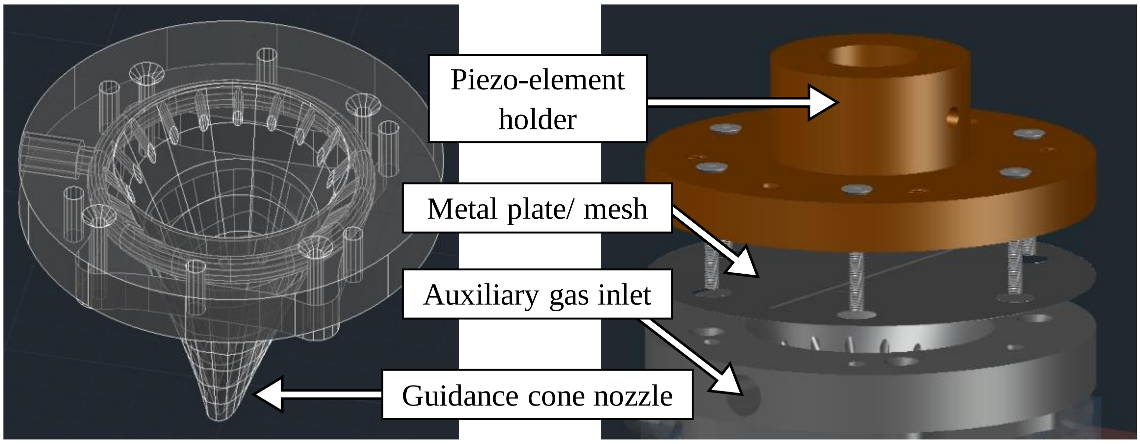

Figure 24: CADs of the cone in X-ray view (left) and in exploded realistic view with the mesh and the piezo-element holder (right).

After several preliminary experiments, it became clear that an improved guidance cone, called cone B, based on the design geometry of the first one, called cone A, had to be developed. The main challenge was to improve the evaporation process of the solvent. It was of importance to avoid droplet formation of condensing liquid at the end of the cone nozzle where the temperature was too low. A new heating device, the Hybec Hi-Heater, was used which allowed heating of the nitrogen auxiliary gas right before entry into the cone which reduced the heat loss during transfer. Thus, at the exit of the cone, up to 50 °C could be reached, measured with a thermocouple.

The new cone, also 3D-printed from steel, featured additional heating cartridges to increase the temperature even further, as depicted in Figure 25. Thus, the cone itself could be heated up and provide even better evaporation of the solvent than with supplying heated gas only.

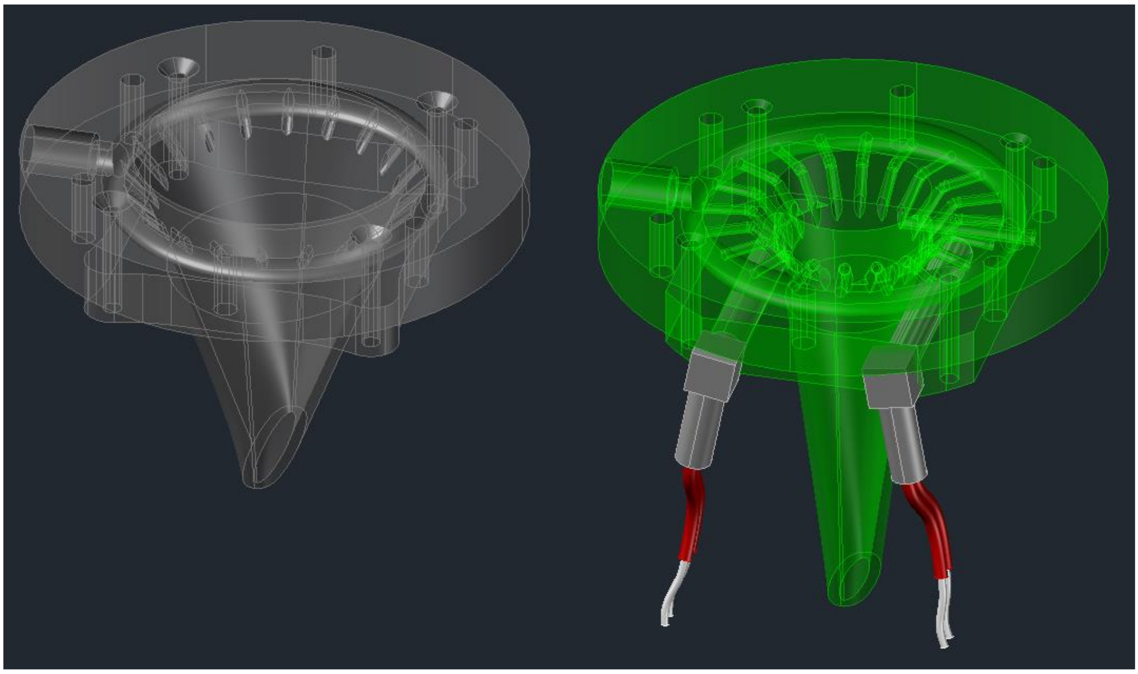

Figure 25: Initial cone design (A, left) and the improved version (B, right) with two heating cartridges.

Furthermore, the nozzle of the new cone was longer to focus the molecules better onto the plasma plume and to give the droplets longer contact time with the heated metal cone and heated nitrogen gas to evaporate. A smaller exit at the end of the nozzle ensured that less analyte was sprayed beside the plume or onto the iLTP electrode. The opening diameter of the nozzle at the mesh side was reduced so that the spray would not be able to expand. However, since the metal plate is being fixed tightly between the piezo-element holder and the cone, a small opening might hinder the proper vibration of the center of the metal plate. Therefore, a gap of one millimeter and the diameter of the previous cone opening was added. An expansion of the liquid into this gap, which might lead to contamination, was theorized, but no such carryover effects were observed. This gap was also included in an 8 mm-thick ceramic plate made from Macor® ceramics that was placed between the heated metal cone B and the mesh (cf. Figure 26). It served as a heat insulator as the piezo-element had a maximum working temperature of 90 °C. Additionally, cooling gas between 3 and 9 L min^{-1} (nitrogen gas at room temperature) was circulated near the piezo-element in an additional effort to prevent overheating of the piezo-element.

In cone A, the auxiliary gas tubes exited the donut-shaped hole through straight tubes in a 45 ° angle to aid the dispersion of the spray in the downwards direction (cf. Figure 25 left). Since the new cone has a smaller inner diameter, the wall thickness at the height of the auxiliary gas tubes is greater and inserting a tube in a 45 ° angle would lead to the auxiliary gas to be added further downstream. Since an addition as early as possible is desirable, the auxiliary gas tubes in cone B had a new tube shape which allowed the gas to flow horizontally at first before then being added in the same 45 ° slope (cf. Figure 25 right). A cross-section cut of the improved guidance cone B inserted on top of the ion source housing displaying the experimental set-up is shown in Figure 26 and the actual experimental set-up can be found in Appendix Figure 80.

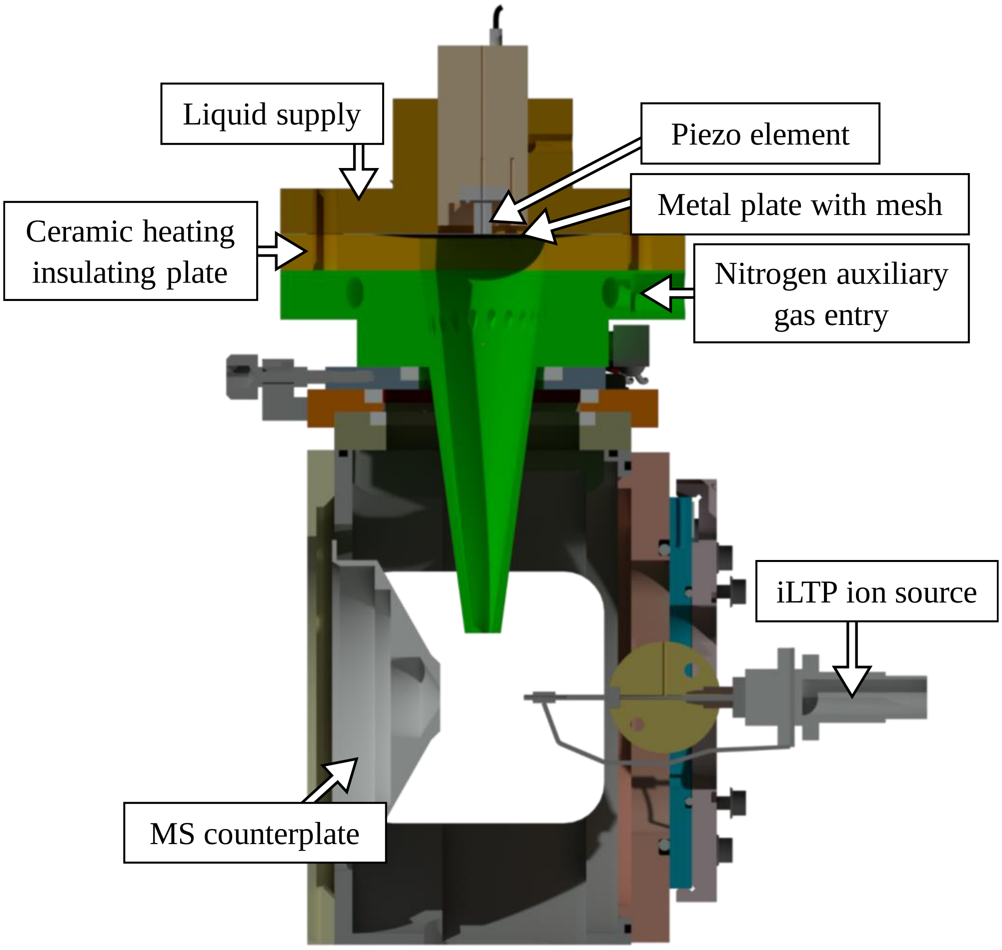

Figure 26: Side-cut CAD of the experimental set-up of experiments with the Hitachi nebulizer including the iLTP ion source, a ceramic plate for heat insulation, the vibrating metal mesh, and the piezo-element.

To compare the efficiencies of cones A and B, 1 mg L^{-1} caffeine and testosterone solution was injected via LC-iLTP-MS. All parameters can be found in Table 3. As the comparison in Figure 27 shows, the improved cone B resulted in peak areas several times higher than those obtained with cone A. Therefore, any further measurements were conducted using cone B.

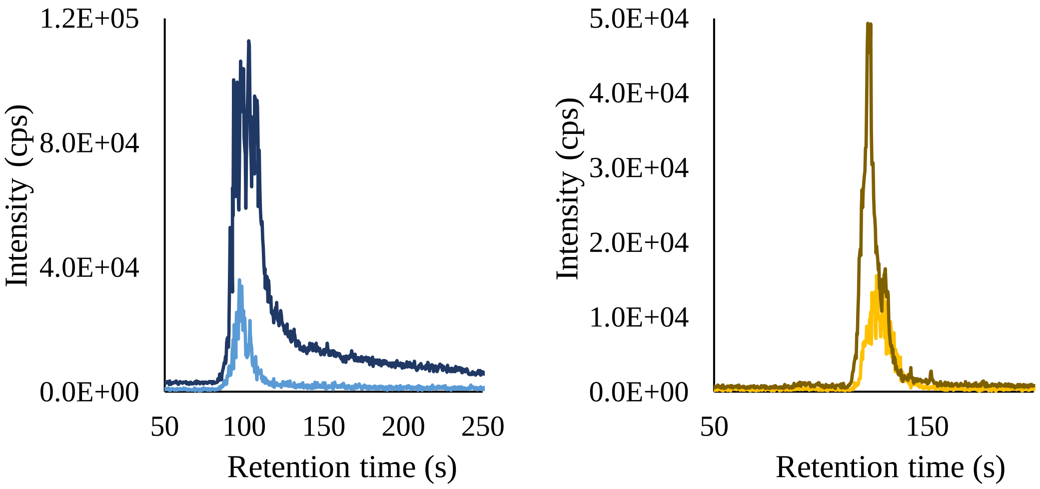

Figure 27: Chromatograms for 1 mg L^{-1} caffeine (left) and testosterone (right) measured with the UPLC-iLTP-MS using the Hitachi nebulizer with cone A (light colors) and the improved version, cone B (dark colors).

The wide peaks and the irregular shape in the chromatograms can be explained by the slow liquid flow rate of 100 µL min^{-1}, which had been determined as an appropriate flow rate for the USN-set-up in order to not leak through the drain port, and the high water content in the standard solution.

The difference between cones A and B are mainly the peak shape and the fact that heating cartridges heat up cone B itself. In order to investigate the reason for the better performance of cone B, measurements were performed using only the nitrogen auxiliary gas heater and no heating cartridges (like in cone A). Comparative measurements were also performed using the heating cartridges only, as well as both heating applications, and none. The parameters were as in Table 3, but auxiliary and cooling gas were both set to 6 L min^{-1}. Figure 28 shows that the best combination is having both gas heater (300 °C) and heating cartridges (90 °C) applying heat (measurement C). If only either is connected, there is a loss in sensitivity (A, B). Auxiliary gas from the side is necessary by all means, as a lack of it gives very low peak areas (D).

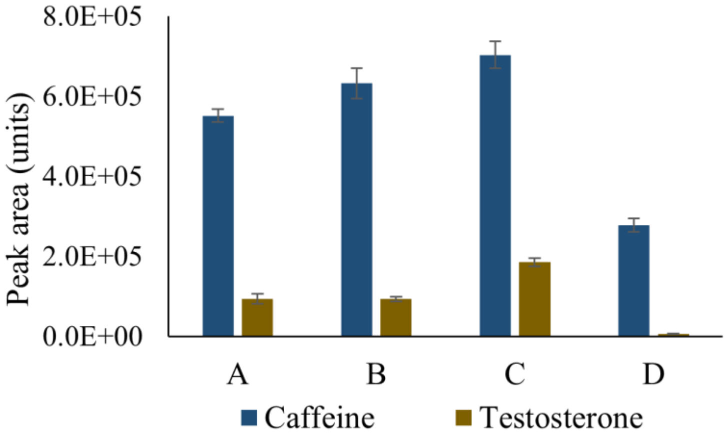

Figure 28: Peak areas of 1 mg L^{-1} caffeine and testosterone being measured in an UPLC-iLTP-MS set-up with the Hitachi nebulizer and cone B: A) with the gas heater only, B) with heating cartridges only and unheated auxiliary gas, C) with both gas heater and heating cartridges, and D) with heating cartridges only but no auxiliary gas. Measurements were performed with six repetitions and without insulating ceramic plate. The gas heater temperature was 300 °C and the heating cartridges temperature was 90 °C.

With the necessity of both heating applications proven, a DoE was performed in order to find the optimal values for the following parameters:

The minimum gas flow rates (cooling and auxiliary gas) of the instrument are 3 L min^{-1}, and it is considered that too high gas flow rates (> 9 L min^{-1}) would increase the velocity of the analyte too much which probably decreases the time for evaporation and ionization. Due to additional heat insulating plates from Macor® ceramic, the heating cartridge temperature could be increased up to 110 °C and the temperature measured near the piezo-element did not reach its critical temperature of 90 °C. Therefore, heating cartridge temperatures between 90 and 110 °C were considered for the DoE. Since the evaporation of the droplets is the main aim and the gas heater temperature takes the longest time to equilibrate and is also influenced by the gas flow rate, its value was fixed at the highest possible temperature given the experimental set-up which was 300 °C. All other parameters were as shown in Table 3.

The DoE results were evaluated with OriginPro. Figure 29 shows the main effects plots for caffeine and Appendix Figure 81 for testosterone. The parameters reaching above the dotted threshold have a significant effect on the analytical results. If a parameter on the y-axis is paired with itself, it means that it has an influence on other parameters as well. This means that the biggest influence on the caffeine peak area was found to be the flow rate of the heated gas. The other parameters and parameter combinations only played minor roles. Testosterone, however, seemed to be significantly influenced by a variety of parameters and their combinations which needs to be further investigated in future studies. The correlation of two different parameters with the biggest effect were the heating cartridges temperature with the cooling gas flow rate for both caffeine and testosterone, whose interactions are depicted in the contour plots in Figure 30 for caffeine and Appendix Figure 82 for testosterone.

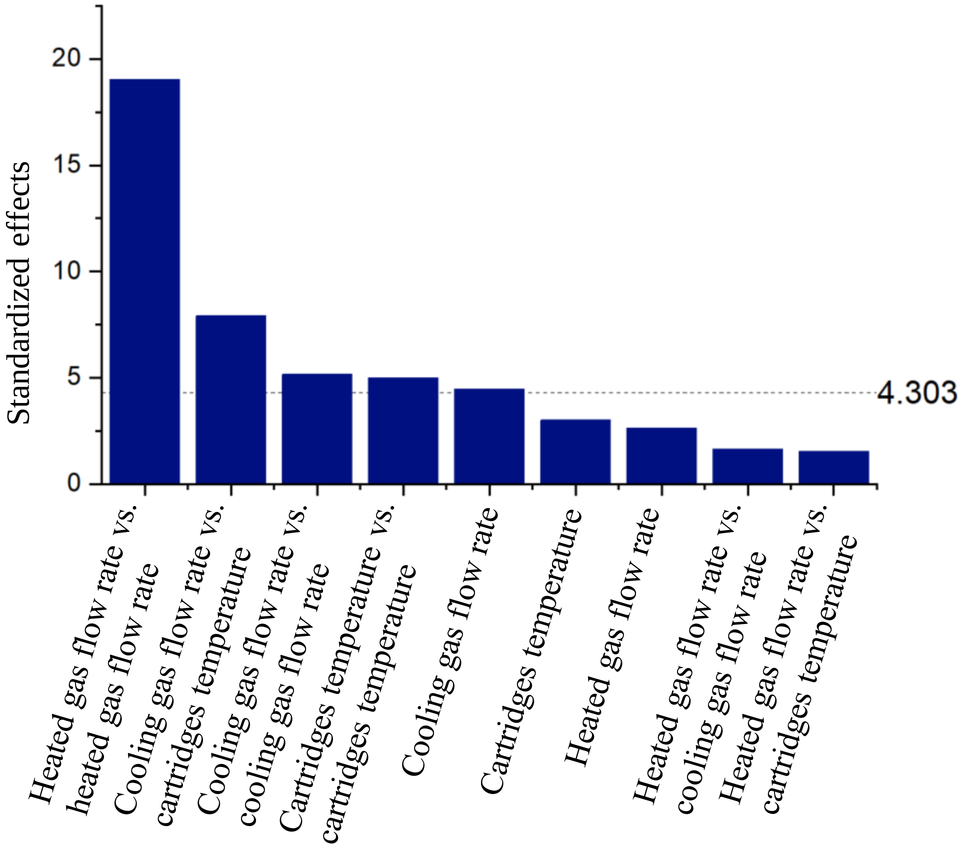

Figure 29: Standardized effects plots for caffeine. Any column over the marked threshold line has a significant influence on the peak area.

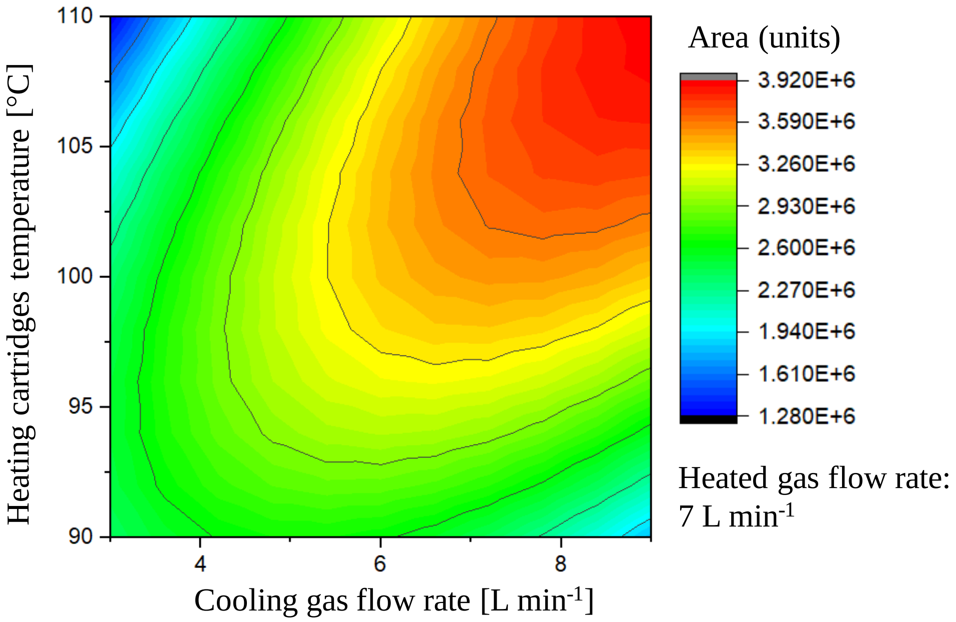

Figure 30: Contour plot for the influence of heating cartridges temperature and cooling gas flow rate on the peak area of caffeine. The heated gas flow rate was kept at the optimal value of 7 L min^{-1}.

Optimal cooling gas flow rate (9 L min^{-1}) and cartridges temperature (110 °C) are at their highest possible values. As explained above, both values cannot be increased further. If a thicker or two insulating ceramic plates were added into the set-up to better shield the piezo-element from elevated temperatures, the path of the analytes would also become longer and the entry of heated nitrogen auxiliary gas would happen further downstream. Therefore, the set-up was kept with one ceramic plate. The heated gas flow rate optimum differed for testosterone and caffeine, which is why any further experiments were performed at a compromisable heated gas flow rate of 7 L min^{-1}.

To evaluate the efficiency of the USN with now optimized parameters, the FoM were determined. They are comprised of a group of characteristic values which describe the method and allow comparison between methods. They include the instrumental Limit of Detection (iLOD) and the instrumental Limit of Quantification (iLOQ) which demonstrate the lowest detectable and the lowest quantifiable concentration of the method and are calculated by means of the rule of three by the signal-to-noise ratio. The correlation coefficient R² describes how well the measured signal responses fit the calibration curve. The sensitivity shows how well the method can distinguish between two close concentration levels by describing the change in response in dependence of a change in concentration. The intra-day and inter-day precision and trueness are calculated using Quality Control (QC) standards. There are three levels of QC standards (low, medium, and high concentration) which correspond to concentrations used in the calibration curve. For the precision, the relative standard deviation (RSD, %) is calculated, and the trueness correlates the theoretical concentrations of the QC standards to the experimentally obtained concentrations of the QC standards: After the establishing of a calibration curve, the QC standards at three levels were measured in triplicates. These were the same standards that had been used for the establishing of the calibration curve. Based on the measured peak areas, the experimental concentration using the calibration curve was calculated. These values often differed heavily from each other. The trueness, also called relative error, was then calculated based on the following:

$$Relative\ Error\ (\%) = \frac{experimental\ concentration\ (obtained\ with\ calibration) - theoretical\ concentration)}{theoretical\ concentration} * 100$$

All standards for the calibration curve and the QC standards were measured on three different, non-consecutive days. All measurement parameters can be found in Table 3. The gas flow rates and the temperatures were as mentioned above.

An example for a calibration curve that was established for caffeine and testosterone using the iLTP-probe is shown in Figure 31. The measured concentrations ranged from 1.5 to 1200 µg L^{-1}. For the calibration curve, all concentrations below the determined iLOQ were eliminated and Grubbs' tests for outliers were performed. Outliers were eliminated and standards were excluded if these actions significantly improved the regression coefficient of the calibration curve and thus its fit to the measured peak areas.

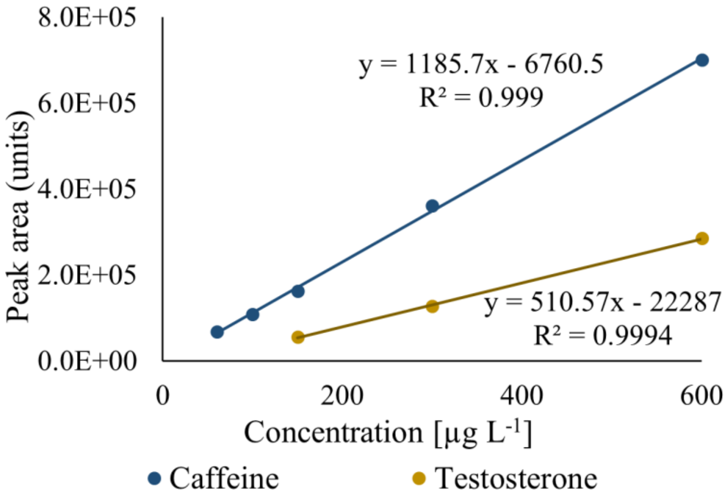

Figure 31: Calibration curve for caffeine and testosterone using the iLTP probe and USN-cone B.

The FoM were determined using the iLTP and the TPI ion sources, each in combination with the USN-cone B nebulization system and the standard APCI nebulizer. In addition, the same measurements were also repeated with ESI. In order to ensure better comparability, the working parameters of the TPI were the same as for the iLTP, except for a higher applied voltage (cf. Chapter 5.6). The results of all measurements can be found in Appendix Table 13 – Table 17. The iLOD and iLOQ are summarized in the following table:

*Table 9: Summary of the average (avg) iLOD and iLOQ values (µg L^{-1}) determined for the USN-cone B nebulizer and the APCI nebulizer with iLTP and TPI, as well as ESI. *Since the ESI-measurements gave high deviations on one day, only two measurement days could be considered.*

		iLTP		TPI		iLTP		TPI		ESI*	
		USN				APCI nebulizer					
		Avg.	RSD (%)	Avg.	RSD (%)	Avg.	RSD (%)	Avg.	RSD (%)	Avg.	RSD (%)
Caffeine	iLOD	25.7	39.4	19.7	43.2	1.5	1.9	1.2	17.5	0.22	-
	iLOQ	78.7	24.0	55.3	62.9	6.4	31.2	5.0	25.2	0.74	-
Testosterone	iLOD	41.3	13.3	17.7	36.8	2.0	91.6	1.4	23.3	0.17	-
	iLOQ	133.0	11.1	85.7	46.5	8.6	78.8	4.3	18.4	0.60	-

There are rather high variations in peak area within and between the measuring days when using the USN. The slow LC flow rate and the irregular vibration of the mesh affected the peak shape. The peak shapes of both caffeine and testosterone are very irregular, as evident from Figure 32 which shows a comparison of the caffeine and testosterone peak at 600 µg L^{-1}measured with the USN-cone B (left) and the APCI nebulizer (right).

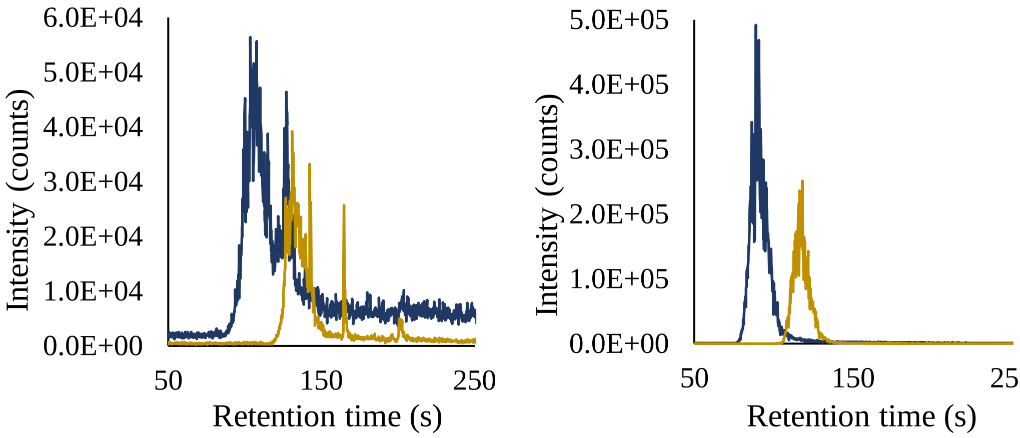

Figure 32: 600 µg L^{-1} caffeine (blue) and testosterone (ochre) measured with the USN-cone B setup (left) and the APCI nebulizer (right) using the iLTP ion source.

Furthermore, the peak area of the same standard varied over the course of the day which explains the high RSD values for the precision and trueness measurements. One factor might be that the cone was heating itself up during the course of the measurement day and that the one hour given for temperature equilibration before the start of the experiment was not sufficient. Another explanation might be that the long, continuous use of the vibrating mesh led to irregularities and inefficient spraying during the course of the experiment.

As the calibration curves show, the APCI nebulizer nearly always gave a better signal response and higher sensitivity than the USN-cone B nebulization system (Figure 33) and the TPI always resulted in bigger peak areas than the iLTP (Figure 34). In the literature, the TPI-type electrode configuration had given similar FoM values as the iLTP[24], but in the present case the TPI proved advantageous, despite its working conditions not having been optimized.

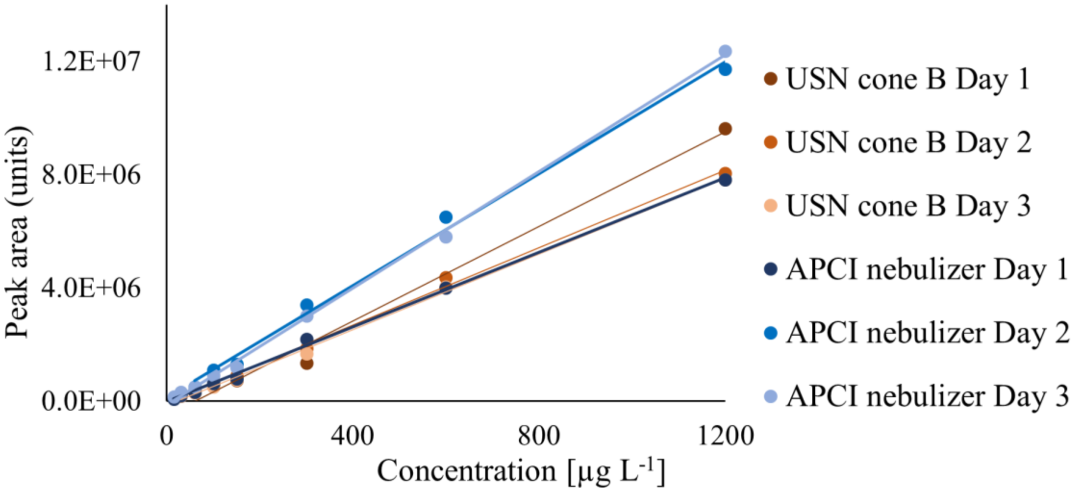

Figure 33: Calibration curves of caffeine measured with the USN-cone B nebulizer (blue) and the APCI nebulizer (brown) using the TPI ion source.

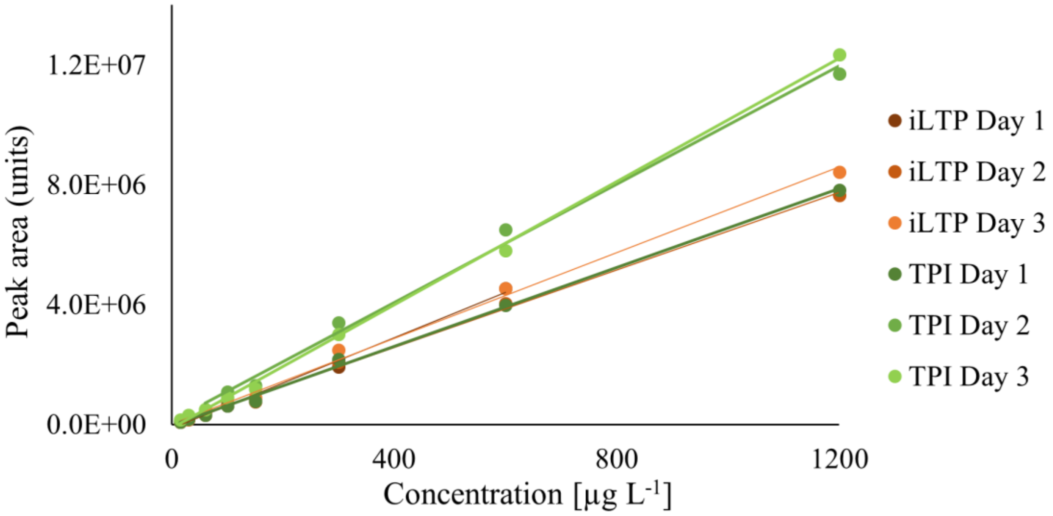

Figure 34: Calibration curves of caffeine measured with the iLTP (green) and TPI (brown) using the APCI nebulizer.

To summarize, these results demonstrate that USN-based spraying of the LC eluent onto the plasma might be a promising field of research to increase the efficiency of LC to MS coupling employing plasma-based ion sources, but there is still room for improvement. One of the main issues with the USN-cone B nebulizer is probably that the droplets are not sufficiently small after the nebulization by the vibrating mesh. Different types of nebulization have already been tried in the literature, however, the main difference is that the flow rates tend to be in the low µL min^{-1} range or without a constant liquid supply at all. Examples include the use of USN by piezo-element vibration for corona-discharge IMS[123] or corona-discharge MS[124]. For investigations with a constant liquid supply, flow rates between a few and up to 50 µL min^{-1} were usually investigated, e.g. using nebulizing chips made from silicon and/or glass[125, 126], surface acoustic wave nebulization[127], also in combination with an LTP ion source[128], or piezo-element driven ultrasonic nebulization in combination with ESI[129, 130]. Since the present work was limited by a fixed LC flow rate of 100 µL min^{-1}, exploration of other types of nebulization did not seem feasable.

Due to the metal-metal interactions of the piezo-element and the plate, the mesh was damaged over the course of the experiments, as seen in Figure 35. This might have had a negative influence on the vibration and thus the spray efficiency. Instead, a mesh with piezo-electric properties like in the bottle humidifier would be of advantage. However, the supply of the liquid without leaking, dead volume, and loss of eluent remains a challenge. A smaller elution rate of the coupled LC might also be of advantage for both the connection between the supply capillary and the vibrating mesh, but also for the vibrating mesh itself to avoid the formation of droplets on the mesh which had been observed during some experiments.

Figure 35: Surface suffering from metal-on-metal interactions of the mesh plate with 0.05 µm holes after several weeks of use.

Due to the temperature restrictions on the piezo-element, the heat applied onto the droplets via the heated nitrogen auxiliary gas and the metal cone are not enough to evaporate the droplets. A cone made of aluminium instead of steel might heat faster and higher, but in this case, a better cooling system besides the insulating ceramics plate and the nitrogen cooling gas has to be developed, like e.g. a water cooling channel. In order to aid the evaporation process and to prevent the droplets from condensating, the ion source housing itself might be heated. A reduced humidity also lowers the risk of arcing in the ion source, but it might also change the plasma chemistry which involves reactions with water molecules.

Furthermore, the dimensions of the spray, including its direction onto the plasma region might have to be miniaturized further. Optimization of position and angles of all critical elements (cone-exit, plasma ion source, and mass spectrometer inlet) would also pose an interesting investigation.

6.2 Implementation of a repeller electrode into an electrospray ionization source

The original idea of this project was it to enhance the transfer of the ions created at the tip of the ESI capillary to the mass spectrometer inlet. For this endeavor, a repeller electrode, meaning a piece of metal at which voltage was applied, was inserted into the ion source housing. The created electric field was thought to push positively charged analyte ions towards the inlet.

At first, different repeller shapes were designed and subsequently manufactured by the mechanical workshops of the university. The first repeller was a steel plate with a diameter of 30 mm and a thickness of 2 mm. It was connected to an HV plug and isolated (Figure 36). The ground of the HV plug was connected via an outer ring to the rest of the ion source housing as can be seen in Figure 37.

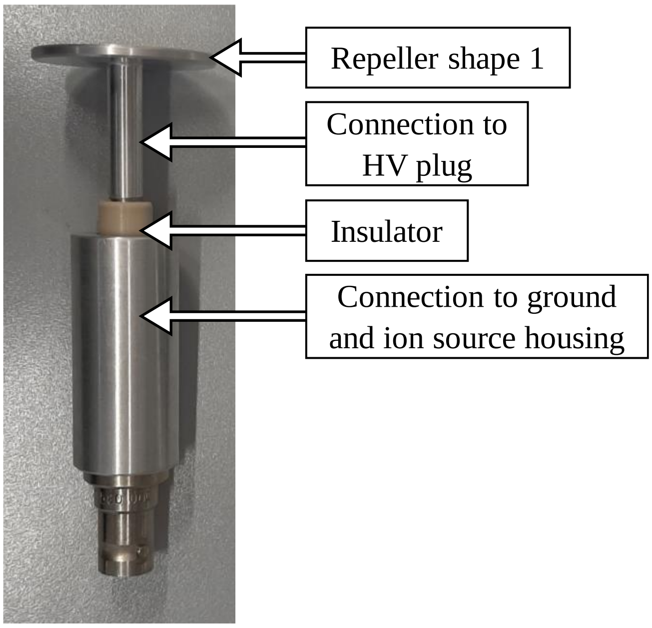

Figure 36: Repeller electrode 1: diameter 30 mm, thickness 2 mm, flat.

The repeller was inserted into the ion source housing opposite to the counter plate of the mass spectrometer. With two moveable plates, the repeller could be adjusted in x- and y-direction, as seen in Figure 37. Inside the repeller holding plate, the repeller could also be moved in z-direction.

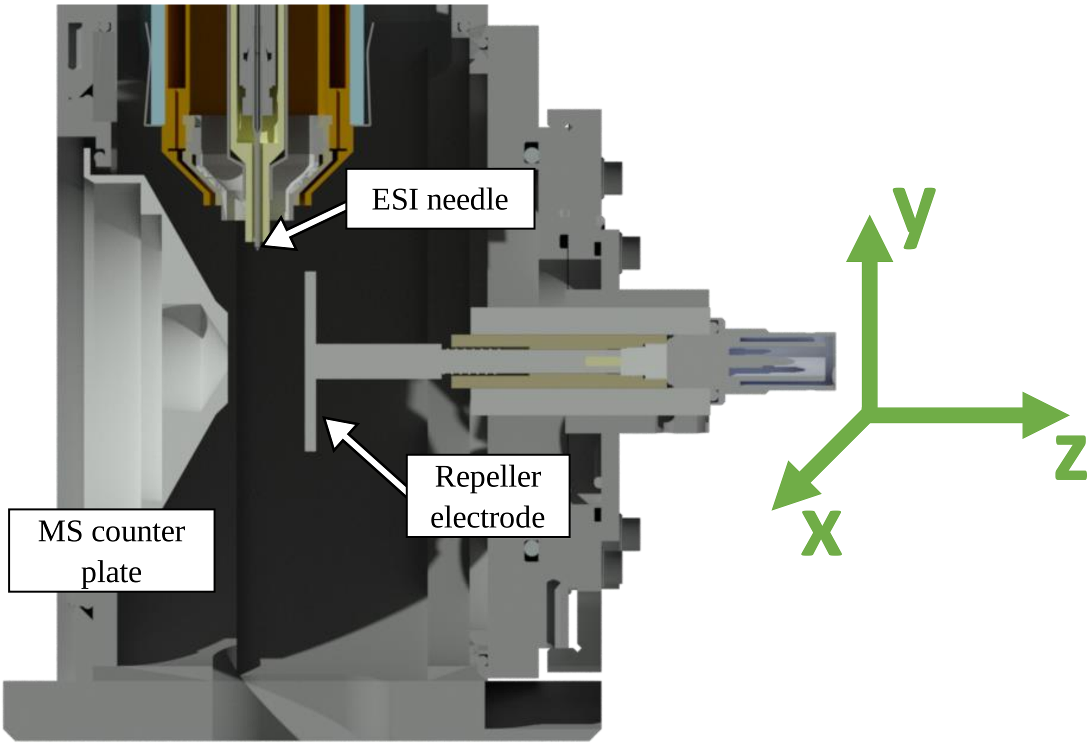

Figure 37: Repeller 1 inserted into the ion source housing at the closest possible position near the ESI needle (y = 0 mm, z = 0 mm).

Besides repeller 1, further designs are shown in Figure 38. The metal stick onto which the repeller head was screwed was replaceable, as can be seen for repellers 4, 5, and 6.

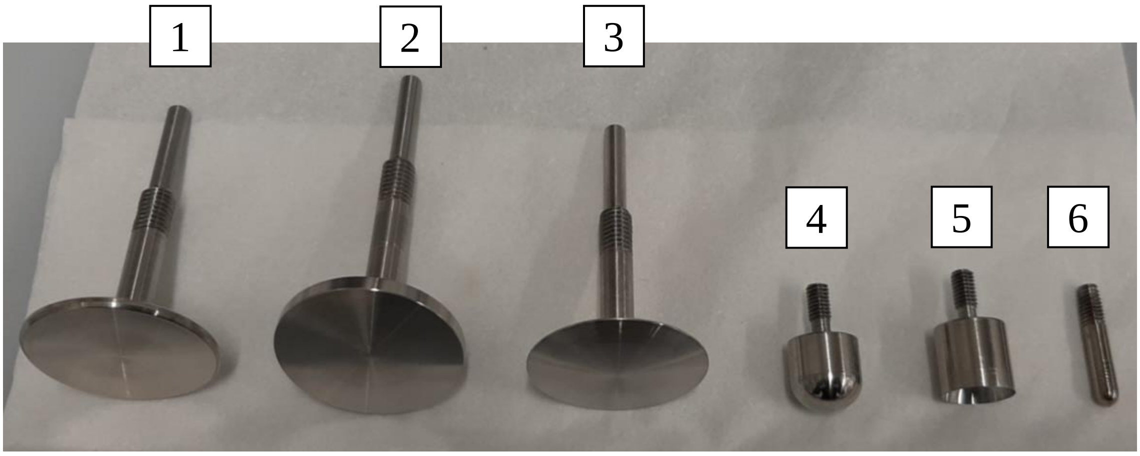

Figure 38: Repellers from left to right: 1) flat, Ø 30 mm, 2) tilted by approx. 13 °, Ø 30 mm, 3) slightly convex, Ø 30 mm, 4) ball-shaped, convex, Ø 12 mm, 5) ball-shaped, concave, Ø 12 mm, 6) rod-shaped, Ø 4 mm.

Furthermore, a three-dimensional repeller from a metal mesh was constructed as can be seen in Figure 39. The idea was it to not only have a repeller from the side but also from the bottom, and since the repeller was made from a mesh, it was easily deformable.

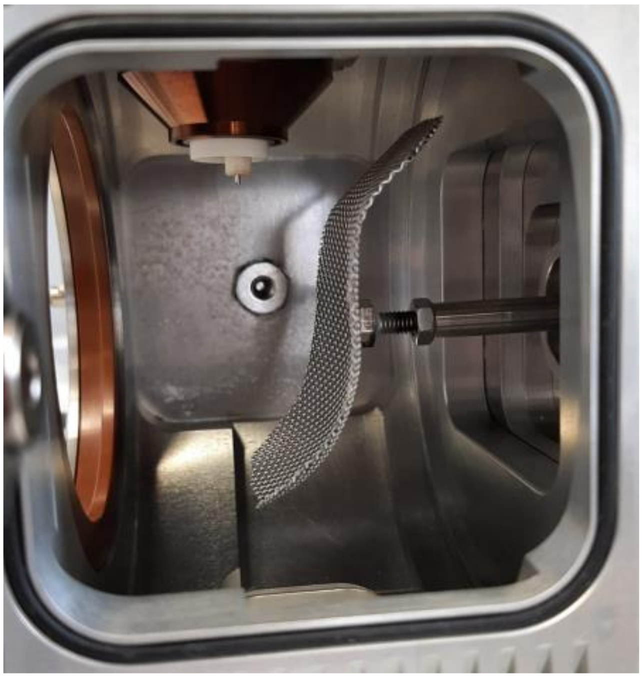

Figure 39: Repeller 7, a three-dimensional steel mesh formed in armchair-formation.

Optimization of the repellers

The influence of the repeller shape, the position of the repeller in the ion source housing, and the applied voltage on the ion transfer efficiency were investigated using continuous injection. Since the syringe pump could not achieve high flow rates, the direct injections were performed at a flow rate of 50 µL min^{-1} in contrast to the 450 µL min^{-1} used in the established LC-method for LC-ESI-MS experiments[57]. All further measuring parameters can be found in Table 4.

At first, repeller 1 was positioned as close as possible to the ESI needle, as is shown in the CAD drawing in Figure 37. During a direct injection measurement, the full scan mass spectra of the six analyte compounds caffeine, reserpine, testosterone, vitamin D3, phenylalanine, and creatinine were recorded while the voltage applied to the repeller electrode was increased every 100 s by 0.2 kV, ranging from 0 to 4.0 kV. This was repeated for different positions of the repeller in the ion source housing: After confirming that the repeller was best centered in x-direction in front of the counter plate and ESI needle, different y-positions (heights) were tested in 3 mm steps. For each y-position, different z-positions (depths) were recorded as well.

An exemplary chronogram of the total ion current (TIC) measured during such measurements is shown in Figure 40. It displays the signal response for different depths (z-position) with which the repeller was inserted into the ion source housing. If the repeller was too close to the ESI needle, the TIC decreased as soon as voltage was applied (Figure 40 dark blue). If the repeller was moved further away (lighter blue tones), the TIC increased until a maximum and then decreased again. The further the repeller was away from the needle, the lower the maximum signal response became and also the more voltage was needed to reach the signal maximum. This is because a stronger electric field would have to be created to have the same effect at the space near the ESI needle. Another side effect was visible arcing between the ESI needle and the repeller if the distance was too small. In these cases, a voltage and a current could be read off and no low voltage could be applied, which is the reason for the gaps in the measurements in Figure 40. As a position too close to the ESI needle was thus unfavorable, positioning the repeller at lower (y-)positions was desirable. The effect of the change in y-position on the TIC is shown in Appendix Figure 83.

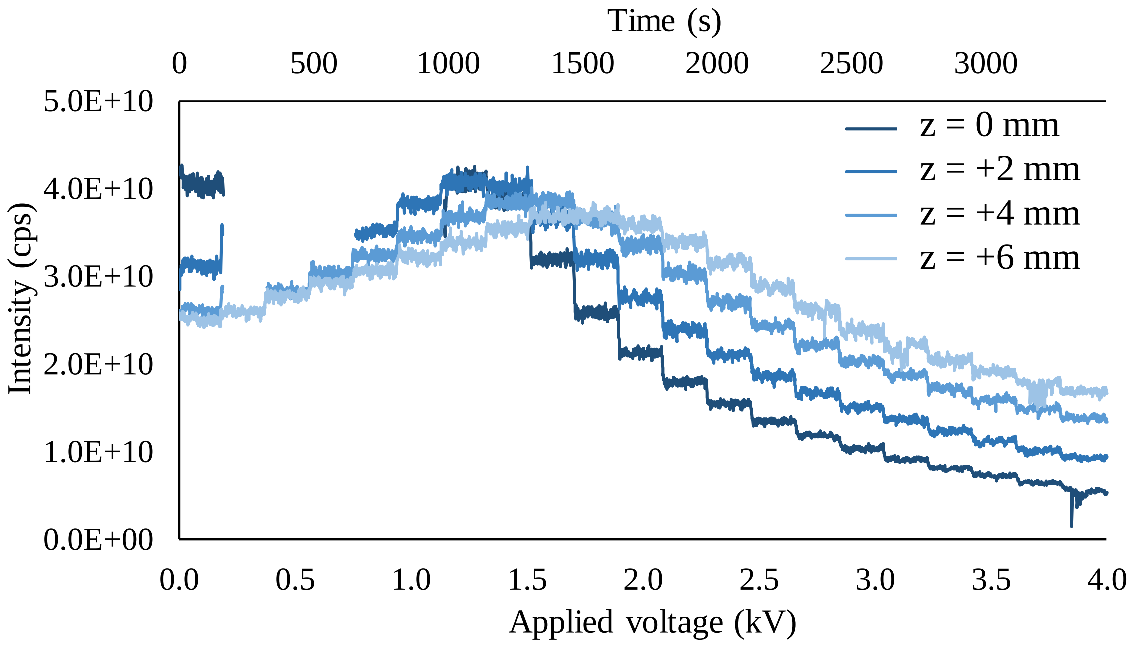

Figure 40: Total ion chronogram for a measurement with repeller 1 at a position of x = centered, y = -6 mm, and different z-positions and differing applied repeller voltages.

In order to find out which repeller exhibited the best properties, the response of each of the six analyte compounds at every voltage step and repeller position was taken into consideration. Figure 41 shows an exemplary mass spectrum of the six analytes. Figure 42 shows an exemplary graph of the peak height of each analyte in dependence of the applied voltage for a measurement with repeller 1 at y = -6 mm and z = +4 mm. Similar to the TIC chronogram (cf. Figure 40), an intensity maximum is reached at a certain voltage for every compound. This voltage, however, differs slightly for each analyte, which was investigated and is detailed further below.

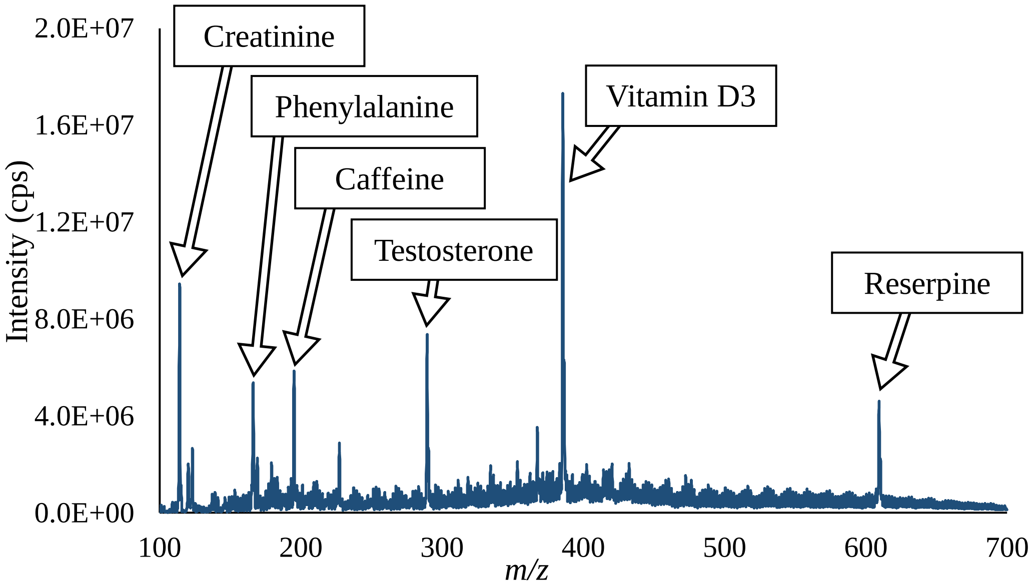

Figure 41: Exemplary mass spectrum showing the peaks for caffeine, reserpine, testosterone, vitamin D3, phenylalanine, and creatinine measured with repeller 6 (rod, Ø 4 mm) at its optimal position y = -9mm, z = 0 mm, and a voltage of 2.4 kV.

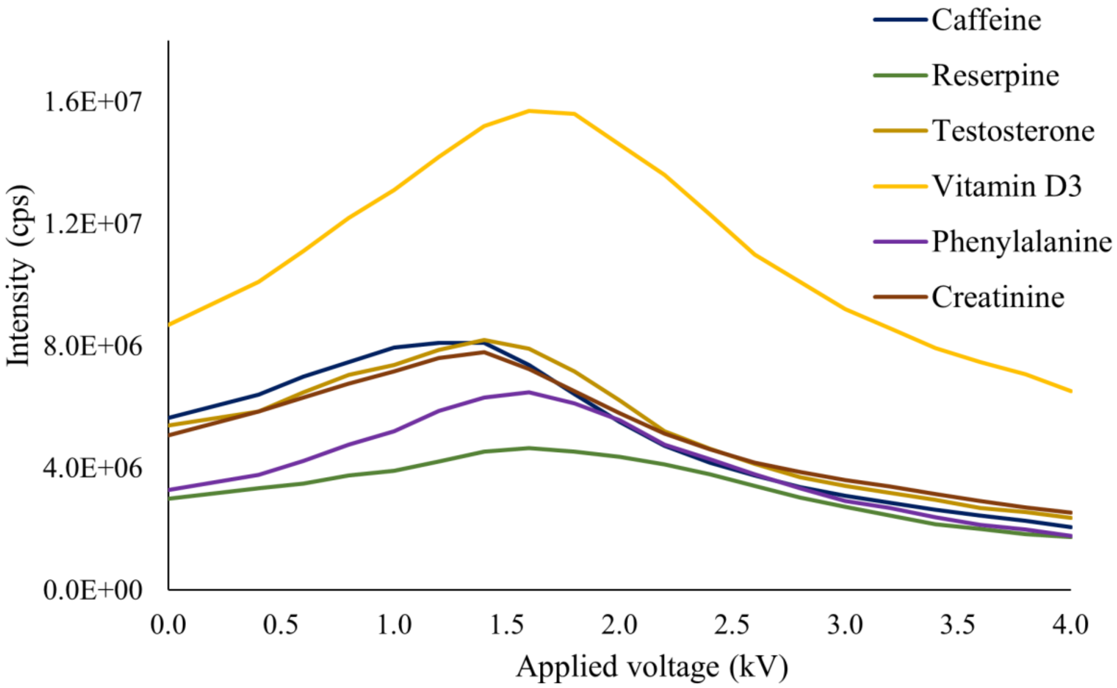

Figure 42: Peak heights of the analyte compounds in averaged mass spectra for differing applied repeller voltage, measured with repeller 1 (flat, Ø 30 mm) at y = -6 mm and z = +4 mm.

When deciding for an optimal repeller position and voltage, the TIC chronogram as well as the respective analyte responses were taken into consideration. As an example, Figure 43 illustrates the dependency of the response of caffeine on z-position and voltage for y = -3 mm. At the closest position (z = 0 mm), the signal response decreases as soon as voltage is applied. Starting from z = +2 mm onwards, a significant peak maximum can be seen which shifts to lower signal intensities and higher voltages for increasing distances of the repeller to the ESI needle, similar to the results of the TIC chronograms in Figure 40.

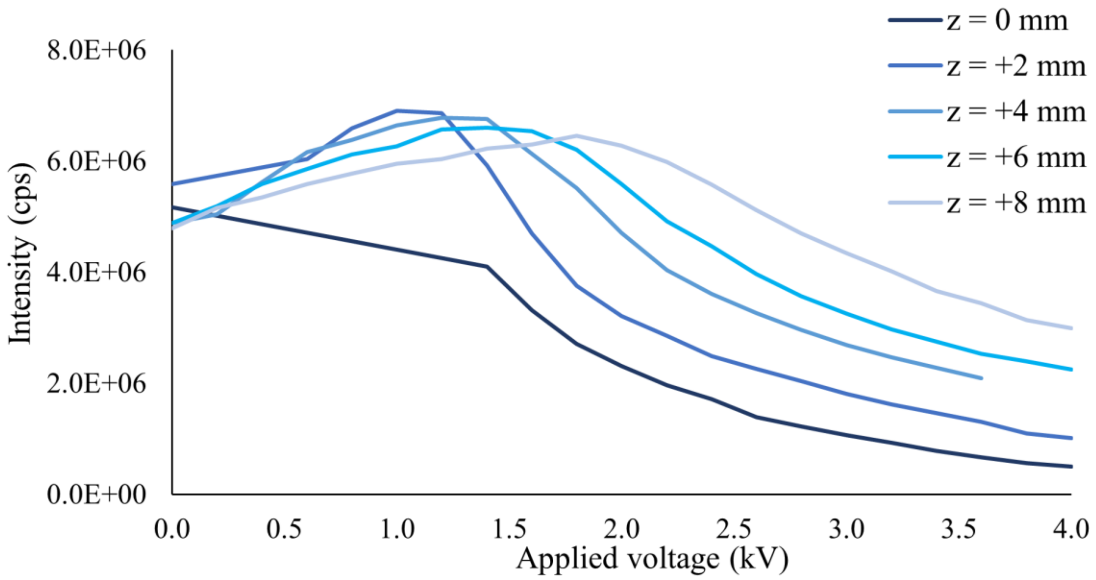

Figure 43: Peak height of caffeine in dependence of the applied repeller voltage and distance in z-direction to the ESI needle, measured with repeller 1 (flat, Ø 30 mm) at y = -3 mm.

The preliminary optimization of repellers 1, 4, 5, 6, and 7 were thus performed and optimal position and voltage determined. Preliminary testing had shown that a smaller repeller gave better results, so that repellers 1, 2, and 3 (Ø 30 mm) were not considered further.

With the spatial repeller positions found optimal via syringe pump continuous injections (50 µL min^{-1}), measurements with LC-MS analyte injections were undertaken at 450 µL min^{-1}, which is the aimed flow rate for the long-term application. The parameters can be found in Table 5. Exemplary chromatograms with repeller 4 (ball-shaped, convex, Ø 12 mm), applying no voltage (left) and 1.5 kV (right) are shown in Figure 44. The peak area recorded with repeller is higher; however, the relative increase of signal response that had been found previously with the syringe injection experiment is not reflected.

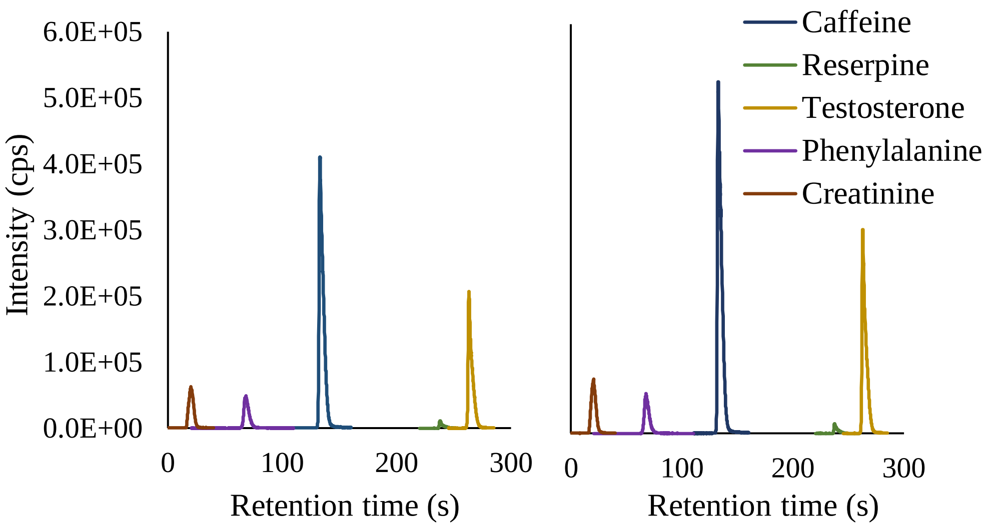

Figure 44: Chromatograms of the analyte standards caffeine, testosterone, reserpine, phenylalanine, and creatinine for LC-MS measurements using repeller 4 at y = -6 mm, z = +2 mm, applying no voltage (left) and 1.5 kV (right).

It was found that for LC-MS injections with a higher flow rate, a higher repeller voltage was required to achieve the maximum in signal response, as can be seen in Table 10. For this, different voltages were tested for each repeller, while the position in the ion source housing was kept at the optimal position found with the syringe pump experiments.

Table 10: Optimal repeller voltage for repellers 1, 4, 5, 6 for the syringe pump experiments at 50 µL min^{-1} flow rate and LC-MS experiments at 450 µL min^{-1} flow rate.

Repeller	**Optimal voltage**		**Optimal yz-position**
	Direct injections with 50 µL min^{-1} flow rate	**LC-MS injections with 450 µL min^{-1} flow rate**	
1	1.0 kV	1.5 kV	y = -6 mm, z = +2 mm
4	1.2 kV	1.5 kV	y = -6 mm, z = 0 mm
5	1.2 kV	1.5 kV	y = -9 mm, z = 0 mm
6	1.4 kV	2.0 kV	y = -11 mm, z = -2 mm
7	2.0 kV	2.5 kV	y = -11 mm, z = 14 mm

When the optimal voltage for LC-MS injections was found, the most promising repellers 4, 5, 6, and 7, as well as repeller 1 and no repeller were compared with LC-MS injection on the same measurement day, resulting in the graph shown in Figure 45.

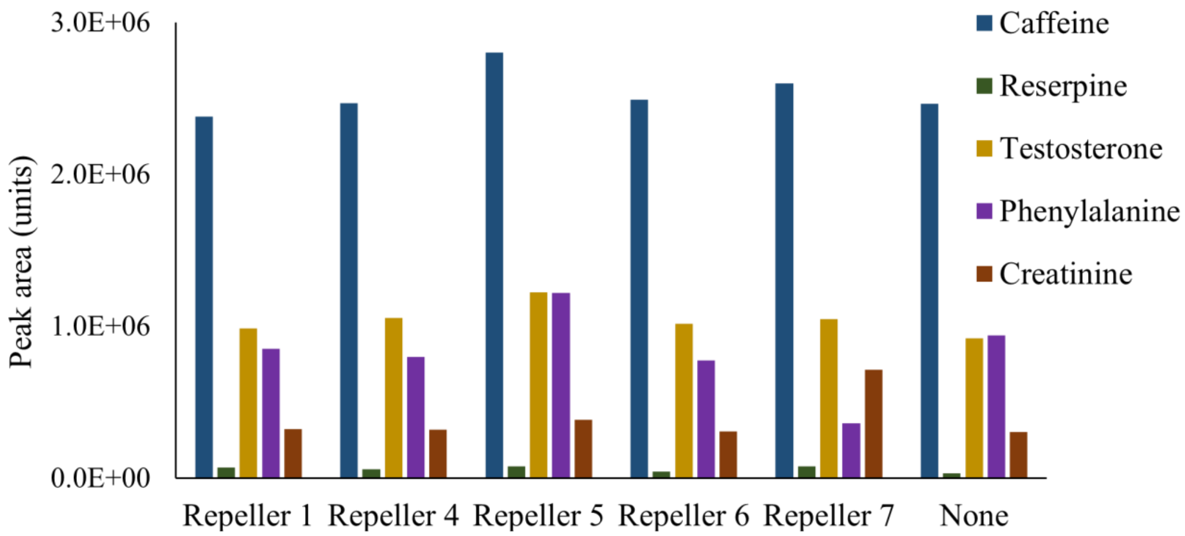

Figure 45: Peak areas for single measurements of caffeine, reserpine, testosterone, phenylalanine, and creatinine using repellers 1, 4, 5, 6, 7, and none for comparison purposes with the repellers in the spatial position found optimal via syringe pump experiments and the voltage found optimal for LC-MS measurements.

Applying the optimal voltage for each repeller, repeller 5 (concave, Ø 12 mm) gave the best results. Therefore, any further measurements were performed with repeller 5 under the conditions of Table 5 and Table 10 if not noted otherwise.

Further investigations of the effects of a repeller electrode

During the direct injections via syringe pump at a flow rate of 50 µL min^{-1}, the application of appropriate repeller voltage had led to a high increase in signal response (cf. Figure 42). However, the LC-MS injections at a flow rate of 450 µL min^{-1} did not have the same impact (cf. Figure 45). Therefore, the effect of the flow rate on the repeller efficiency was investigated:

The standards caffeine, reserpine, testosterone, vitamin D3, phenylalanine, and creatinine were directly injected as a mobile phase of the UPLC into the MS. Thus, the flow rates 50, 100, 200, 300, and 450 µL min^{-1} could be tested. All further parameters can be found in Table 6. As with the previous direct injection experiments, the repeller voltage was increased every 100 s by 0.2 kV from 0 to 4 kV. The signal without repeller at every flow rate was also recorded (Figure 46 top, triangles). The peak heights of each compound from averaged mass spectra were used for the evaluation. It could also be noticed that the peak heights without repeller were already higher than when a repeller was implemented with low voltages.

In order to normalize the results, the peak height for the measurements with the repeller at every voltage was divided by the peak height without repeller at the same flow rate, and the result is shown for caffeine in Figure 46 (bottom). Comparing the different signal responses at 0 kV repeller voltage and having no repeller inserted, it was initially concluded that the presence of the repeller alone has an influence on the ion transfer and flow dynamics in the ion source housing. Only when a certain minimum voltage is applied does the signal response reach the same value that had already been reached without a repeller. Furthermore, the positive effect of the repeller is highest for the lowest flow rate. Since the LC-MS measurements had to be performed at high flow rates, the repeller influence is diminished in comparison to the direct injections at low flow rates. However, the overall effect of the repeller in this experiment was not as great as previously seen in the optimization experiments.

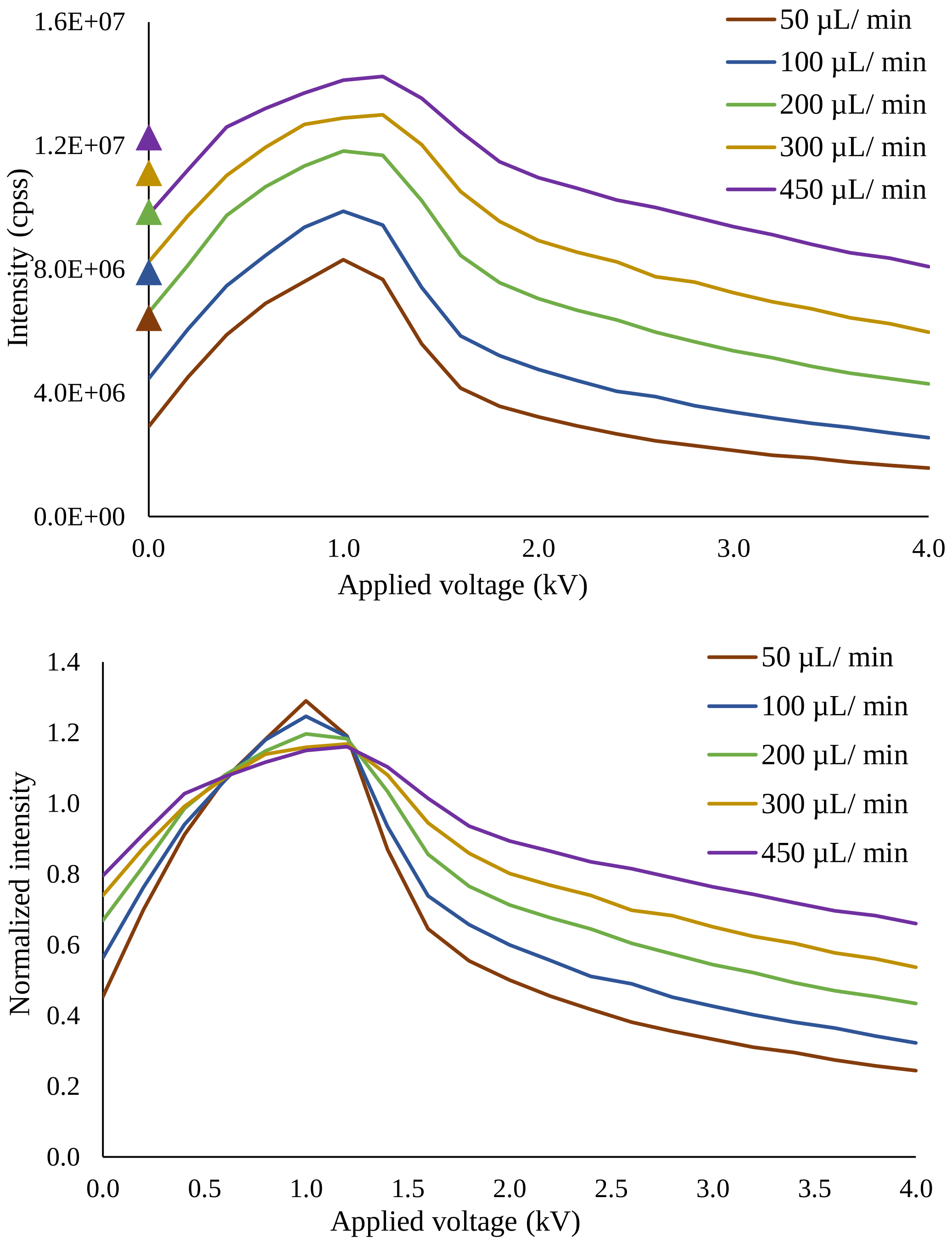

Figure 46: Top: Averaged peak height of 35 µg L^{-1} caffeine measured with repeller 5 at y = -9 mm, z = 0 mm (previously determined optimal positions) at different flow rates and applied repeller voltages. The triangles represent the average peak height recorded at the corresponding flow rate without repeller. Bottom: The normalized peak height is obtained by dividing every averaged peak height obtained with repeller by the averaged peak height obtained without repeller at the same flow rate.

Another observation was that the repeller voltage of the signal response maximum differs for the different analytes (cf. Figure 42). To test whether there is a correlation between optimal voltage and analyte *m/z*, an Agilent Technologies ESI tune mix with measurable compounds ranging from 322 to 1821 Da was measured via direct injection at a flow rate of 50 µL min^{-1}. As can be seen in Figure 47, the higher the *m/z* of the molecule, the higher is the required voltage to reach the maximum peak intensity.

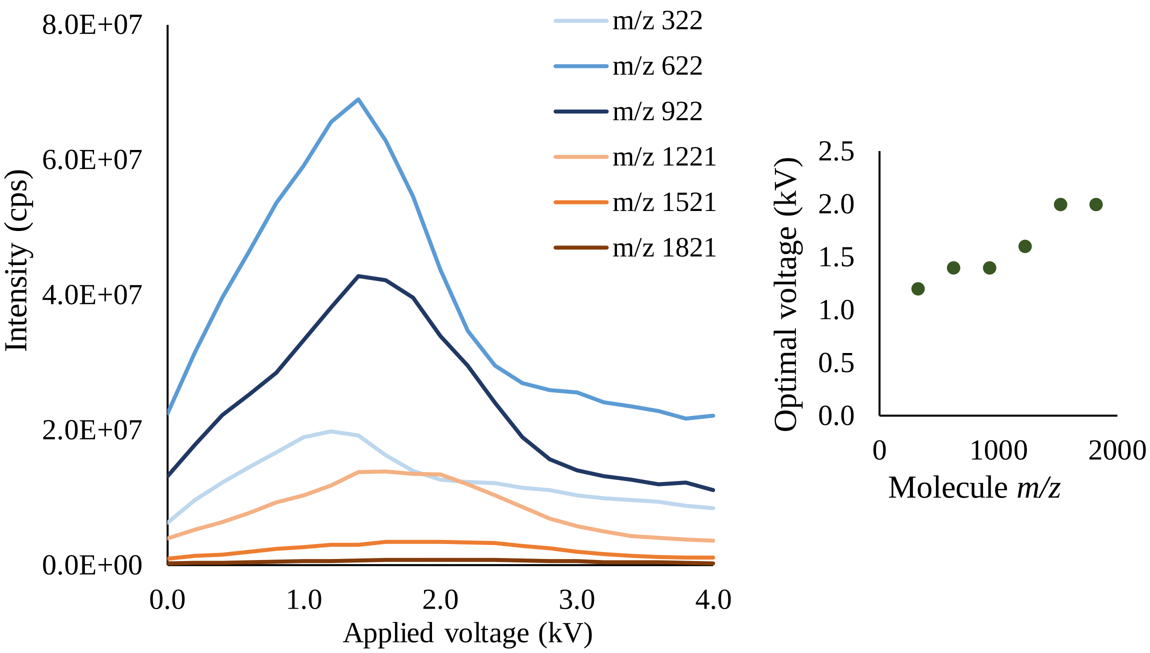

Figure 47: Peak intensity in dependence of repeller voltage for compounds of the ESI low concentration tune mix from Agilent containing compounds with m/z from 322 to 1821.

Design of Experiments and calibration

In order to find the optimal x-, y-, and z-position and the corresponding voltage of the best repeller, a DoE was performed using LC-MS injection. The parameters are shown in Table 5, however, in this study, 0.1 % formic acid and 5 mmol ammonium formate were also added to the sample. For the x-position the boundaries 3 mm to the left and to the right from the center position were used, for the y-position 0 mm and -11 mm, and for the z-position 0 mm and +6 mm (referring to Figure 37). The voltage was varied between 0 and 4 kV.

With the evaluation of the DoE results, it could be confirmed that the best x-position is centered in front of the counter plate and the ESI needle. Figure 48 shows the contour plot for the y-z-position for both caffeine (top) and testosterone (bottom) as examples. Surprisingly, the resulting peak area increased with increasing distance from the mass spectrometer inlet in z-direction which requires a higher voltage to establish the same electric field near the ESI capillary than at smaller distances. The curves of fit displaying the responses of each analyte to each parameter as well as the averaged optimized results can be found in Appendix Figure 84.

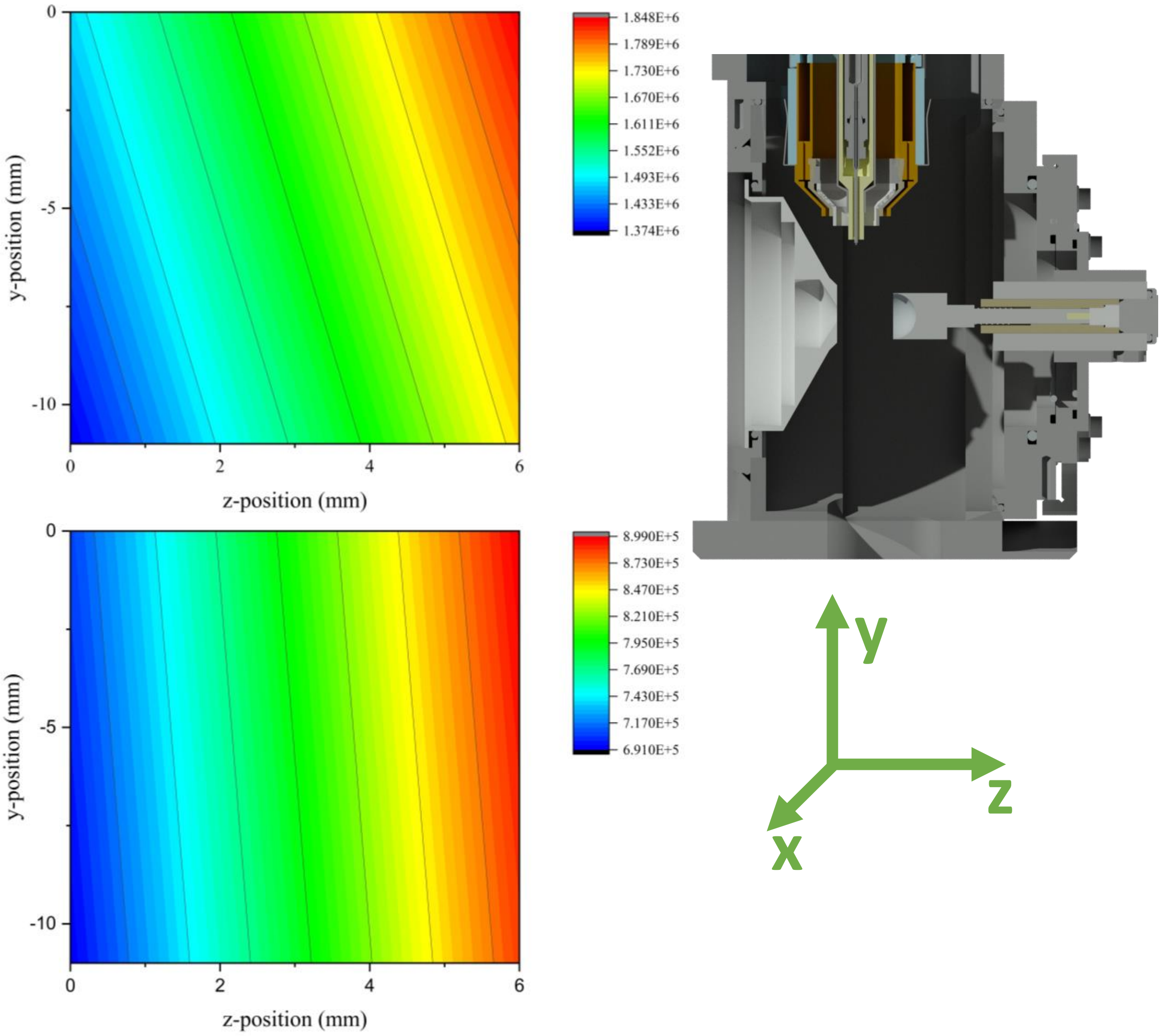

Figure 48: Contour plots for caffeine (top) and testosterone (bottom) showing the effect of the spatial y-z-position of repeller 5 with the fixed x-position in the center and the fixed voltage of 2.27 kV.

According to the results evaluated with OriginPro, the optimal parameters were x = -0.24 mm, y = -11 mm, z = +6 mm, and 2.27 kV. The optimized position that had been found with the previous step-by-step optimization via syringe pump had been x = 0 mm, y = -9 mm, z = 0 mm and subsequently 1.5 kV for LC-MS injections. With both types of optimization, triplicate runs with all analytes were performed and compared to ESI without repeller. The resulting peak areas in Figure 49 show a slightly higher response for the step-by-step optimized values, but the DoE-based results give a lower standard deviation. Therefore, it was decided to continue with the results from the DoE.

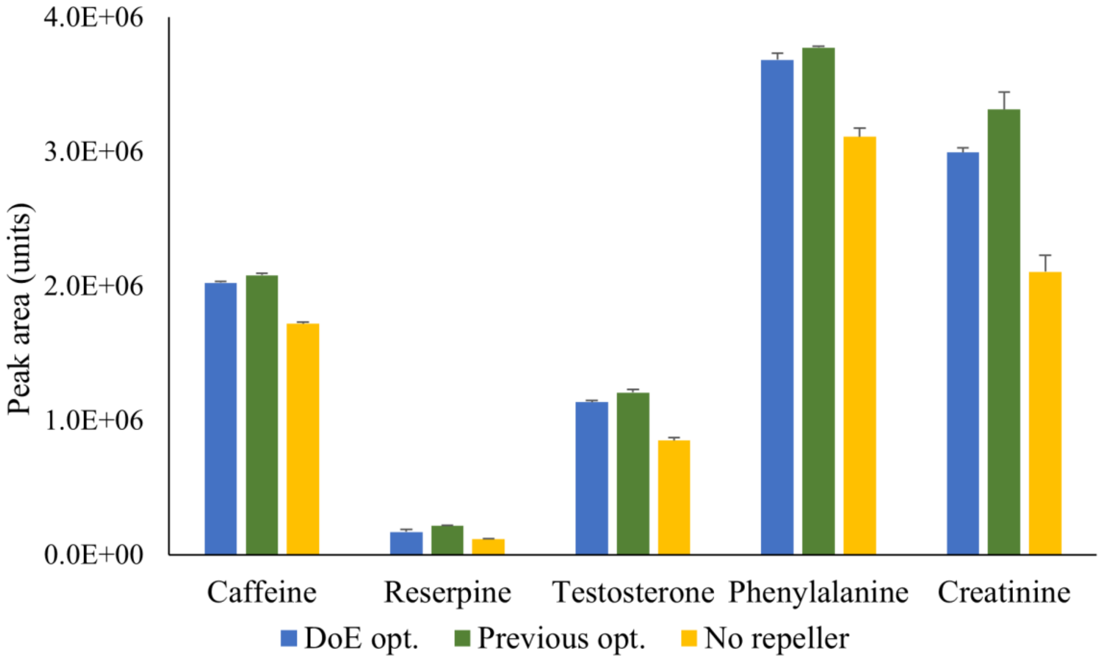

Figure 49: The five standards measured via LC-MS with the parameters found optimal for repeller 5 after the DoE experiments, the step-by-step optimization, or without repeller inserted.

In the next step, a calibration curve was established. Standards ranging from 0.1 ng L^{-1} to 300 µg L^{-1} were prepared from stock solutions. All other parameters can be found in Table 5 and measurements were performed in triplicates. For the limit of detection (LOD), the lowest concentration which gave a recognizable peak and a signal-to-noise ratio of at least three was determined. As an example, Figure 50 shows the peaks that were obtained for 0.1, 0.03, and 0.01 µg L^{-1} for caffeine. As can be seen, 0.1 µg L^{-1} (dark blue) gives a recognizable peak for both with and without repeller with a signal to noise ratio higher than three, while both 0.03 and 0.01 µg L^{-1} are not distinguishable from noise anymore. Therefore, the LOD for caffeine must be below 0.1 µg L^{-1} for both set-ups.

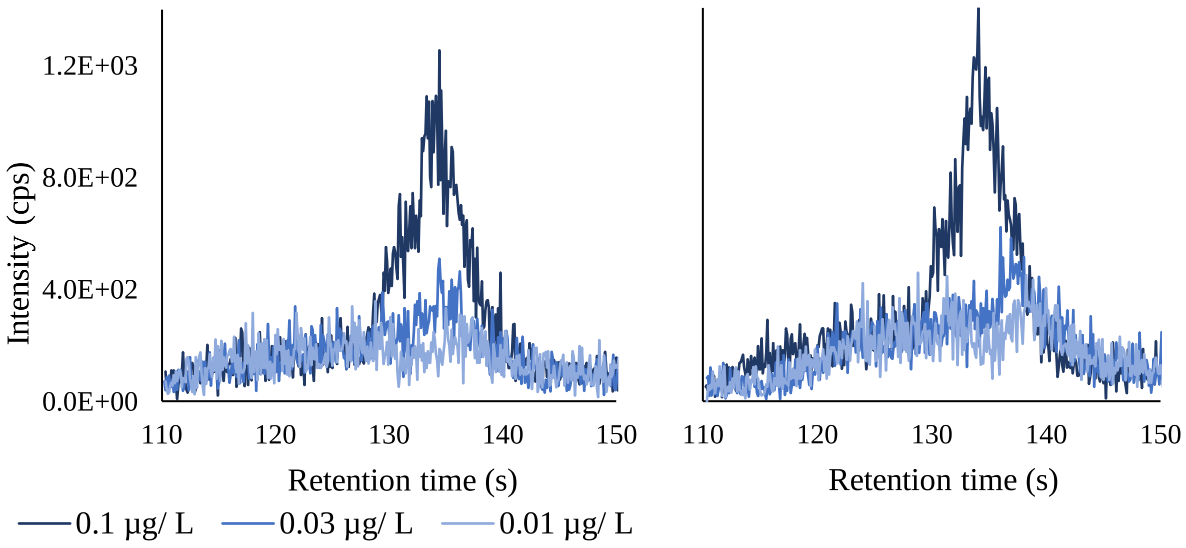

Figure 50: Chromatogram of caffeine at concentrations near the LOD using repeller 5 (left) and no repeller (right).

There is no big difference in peak area for the measurements with and without repeller which is also evident from Figure 51 which shows exemplary calibration curves for caffeine and testosterone. As reserpine, creatinine, and phenylalanine could not be detected well, no calibration curves for these substances could be established.

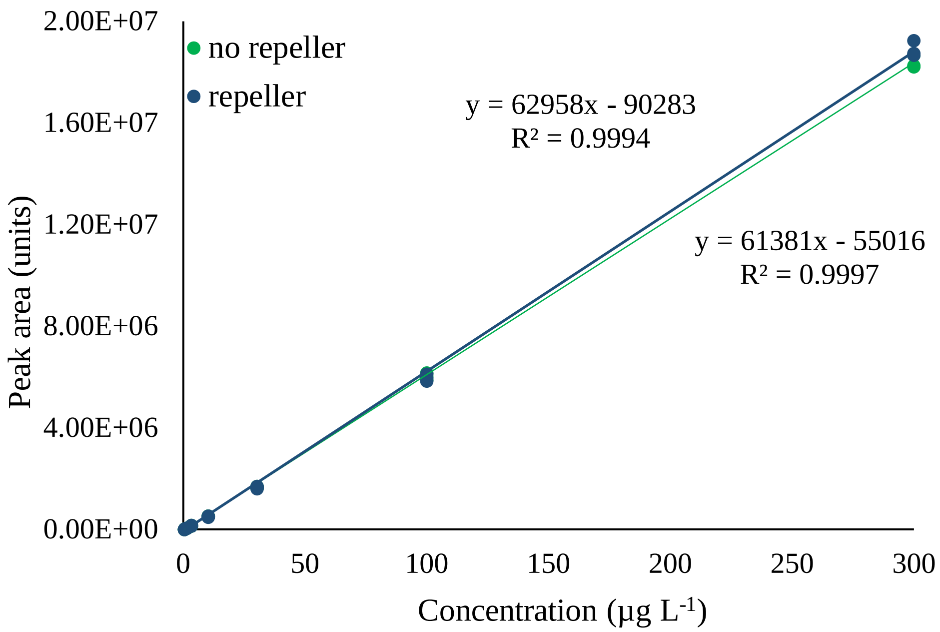

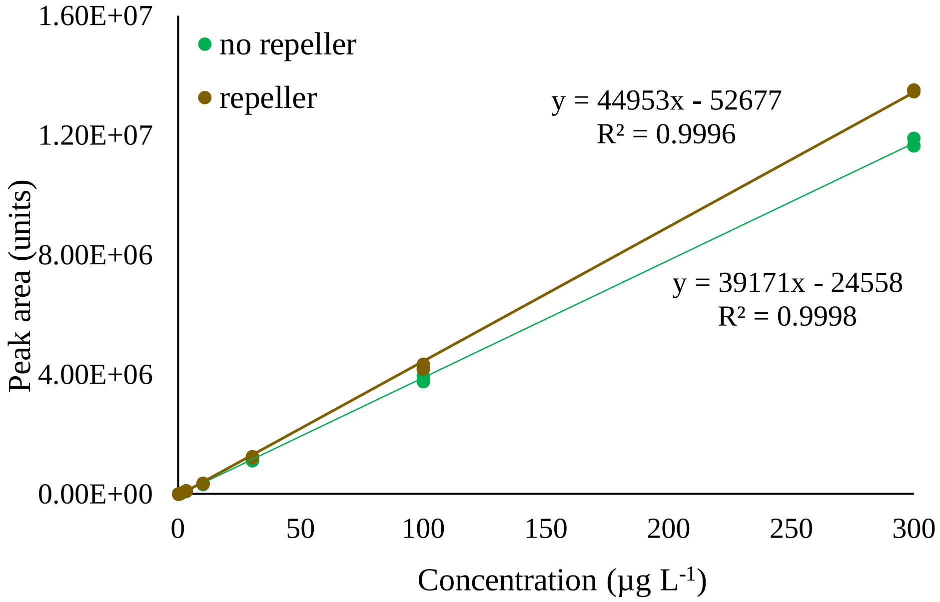

Figure 51: Calibration curves for caffeine (top) with and without repeller (0.1 – 300 µg L^{-1}) and testosterone (bottom) with repeller (0.03 – 300 µg L^{-1}) and without repeller (0.1 – 300 µg L^{-1}).

The slopes of the calibration curves with repeller are higher in both instances which shows that the repeller has a positive effect on the sensitivity of the method, meaning that an increase in concentration leads to a higher increase in signal response. Based on the calibration curve and the chromatograms of the runs, it could be determined that the LOD for caffeine is below 0.1 µg L^{-1} and for testosterone below 0.03 µg L^{-1} with repeller and without repeller. In general, the peak areas are only slightly greater for the measurements with repeller and the difference to the peak areas without repeller becomes smaller with decreasing peak area. Therefore, it has to be concluded that the repeller electrode has an overall minor effect on the abundance of ions entering the MS under the used measurement conditions.

It is probable that not only the electric field has an influence on the ion transmission but that fluid dynamics of the liquid and the auxiliary gas flows in the ion source housing also play a role. To test this, a new ion source housing would need to be designed which is smaller and has more flexibility regarding the position and angle of the ESI needle and the repeller electrode. Fluid dynamics calculation would also be of advantage for a possible future project in that direction.

Real samples

Nevertheless, the repeller efficiency was also tested in a real sample to see whether the repeller would work with matrix and also to see the effect of increasing contamination in the ion source. Human plasma was prepared by dissolving the plasma powder in 5 mL water according to the instructions of the manufacturer. Based on the procedure by Leal Cunha et al. (2021), the plasma was prepared as follows[131]. 800 µL acetonitrile, that had been stored in the -20 °C freezer, were added to 200 µL plasma sample. The reaction tubes were first inverted for one minute, vortexed for two minutes, and then centrifuged at 14,000 rpm for ten minutes. The upper 800 µL of each reaction tube were filtered through a 0.20 PTFE membrane into one glass vial. This vial was then dried at 40 °C under soft nitrogen flow for 50 min. The remaining substance was reconstituted with 1200 µL of 1 mmol L^{-1} formic acid in methanol solution. The plasma samples were spiked with sufficient analyte to ensure good visibility. Since the unspiked plasma already showed peaks of caffeine, phenylalanine, and creatinine, as visible in Figure 52, only reserpine and testosterone were added to the sample.

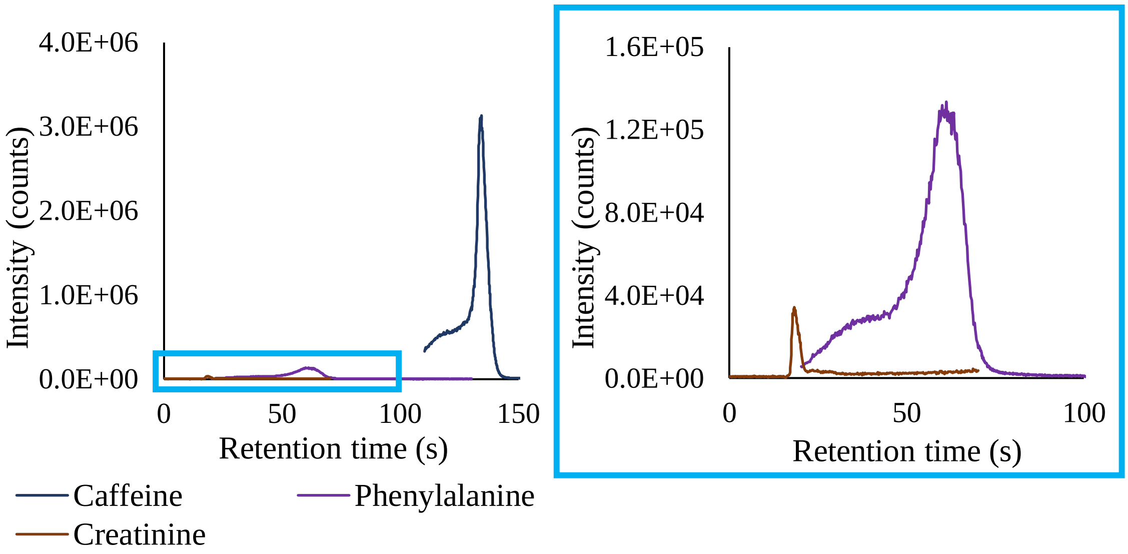

Figure 52: Chromatogram of unspiked plasma with caffeine, phenylalanine, and creatinine measured in MRM mode (left) and in zoomed view to better visualize phenylalanine and creatinine (right).

All parameters can be found in Table 5.The measurement order was as follows: At first, a standard consisting of 50 : 50/ methanol : water, as had been used during all previous measurements, with 30 µg L^{-1} reserpine and 10 µg L^{-1} testosterone was measured. Then, the processed plasma spiked with the same concentration of analytes was measured and subsequently a methanol/ water blank serving as quality assurance was measured. Measurements with and without repeller were done on two different measuring days, and the mass spectrometer was cleaned before and after each measuring day, including the counter plate, AP1 and APM.

There was a rather high variability in between runs, leading to RSDs up to over 90 % as can be seen in Appendix Table 18. It is curious, however, that the RSD for caffeine was below 5 % in both measurement series (with and without repeller). Reserpine and testosterone, which had been spiked to the plasma, obtained RSD values between 46 and 94 % in the plasma and between 8 and 57 % in the standards. Carry over can be excluded since the blank measurements showed no peaks.

In the standards, the highest signal was obtained in the first measurement of the day for both reserpine and testosterone. Then, the reserpine response fell further with every run while the testosterone signal reached a plateau, as can be seen in Figure 53.

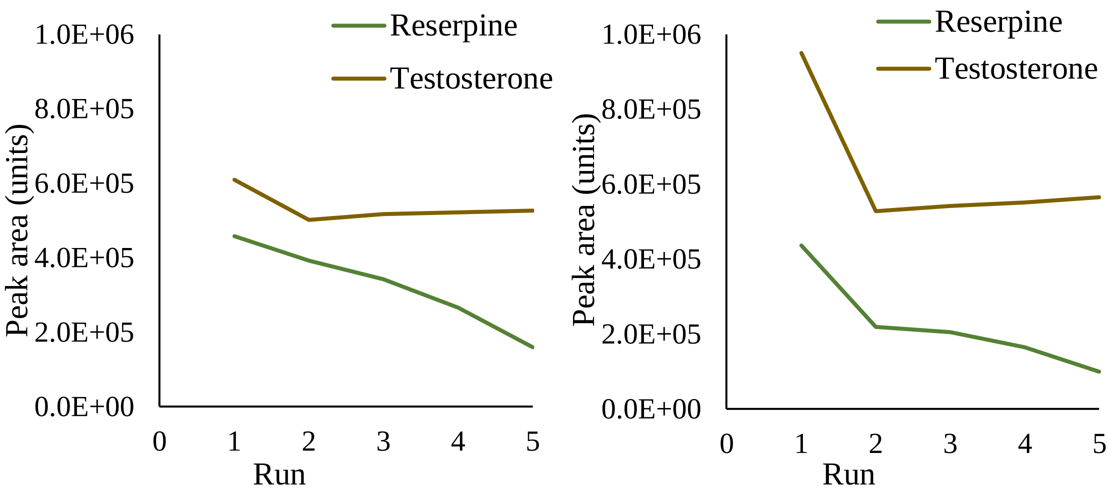

Figure 53: Peak areas for 30 µg L^{-1} reserpine and 10 µg L^{-1} testosterone in 50 : 50 methanol : water measured with five repetitions, with (left) and without repeller (right).

As can be seen in Figure 54, reserpine and testosterone in the plasma follow a similar trend of decreasing peak areas until a plateau is reached. Caffeine, however, does not show any significant changes. There is also no significant difference between the measurements with and without repeller. Normalizing the peak areas by dividing the results of the measurements with repeller by those without repeller did also not give conclusive results due to the high standard deviations in the measurements.

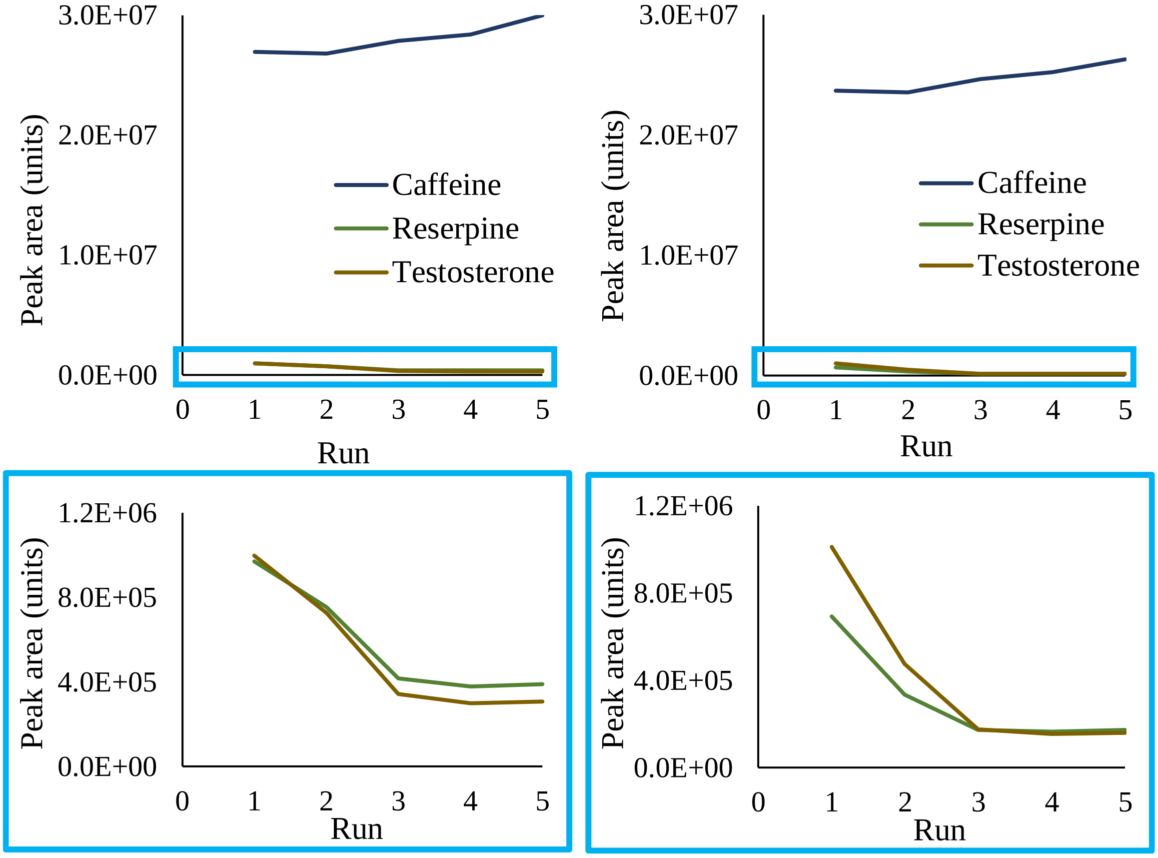

Figure 54: Peak areas for naturally occurring caffeine as well as spiked 30 µg L^{-1} reserpine and 10 µg L^{-1} testosterone in plasma measured with five repetitions, with (left) and without repeller (right). The graphs on the bottom show reserpine and testosterone results separately for better visualization.

During the cleaning procedure it was found that measurements with human plasma severely contaminated the MS which is a probable reason for the declining peak areas during the course of a measurement day. Figure 55 shows a construction piece of the MS02a located behind the counter plate after such a measurement day.

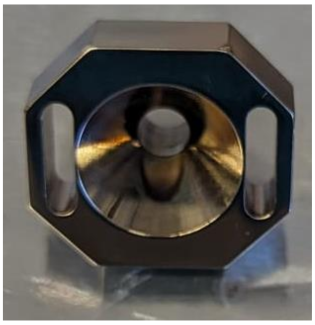

Figure 55: Visible contamination on a construction piece of the MS02a located behind the counter plate after a day of measurements with human plasma.

Putting the ion transmission theory to the test

It was discovered that ions could be detected with the MS even when the ESI needle voltage was turned off and only the repeller voltage was turned on. To test whether the repeller electrode itself is capable of ionizing the molecules, the APCI nebulizer, which had been the improvement effort of the previous chapter 6.1, was used (in its original set-up) to provide a nebulizing spray without any ionization source. The measuring parameters are listed in Table 7.

A UPLC was used to provide a continuous flow of 200 µL min^{-1} of the previously used test solution. Repellers 1, 2, 4, 5, and 6 were tested. The repellers were inserted in the lowest possible position (y = -11 mm) as it had proven advantageous during the optimization. As the outlet of the APCI nebulizer is in a different spatial position than the ESI needle, the repellers were manually adjusted in z-position (depth) to be right in front of the nebulizer outlet (position A). After the first measurement, the repeller was pulled out further away from the nebulizer by 5 mm and 10 mm (positions B and C).

The repeller voltage was increased until a mass spectrum could be seen in which the highest analyte peak (reserpine) became distinguishable from the background noise. The peak intensities of the analyte peaks were averaged over 10 s during which the voltage was kept constant. The voltage was increased until the TIC would decrease again in order to find a TIC maximum. In certain cases (e.g., Figure 56 position B), the voltage was decreased again to find the highest repeller response. Exemplary TIC chronograms for repeller 4 in three measured positions are shown in Figure 56.

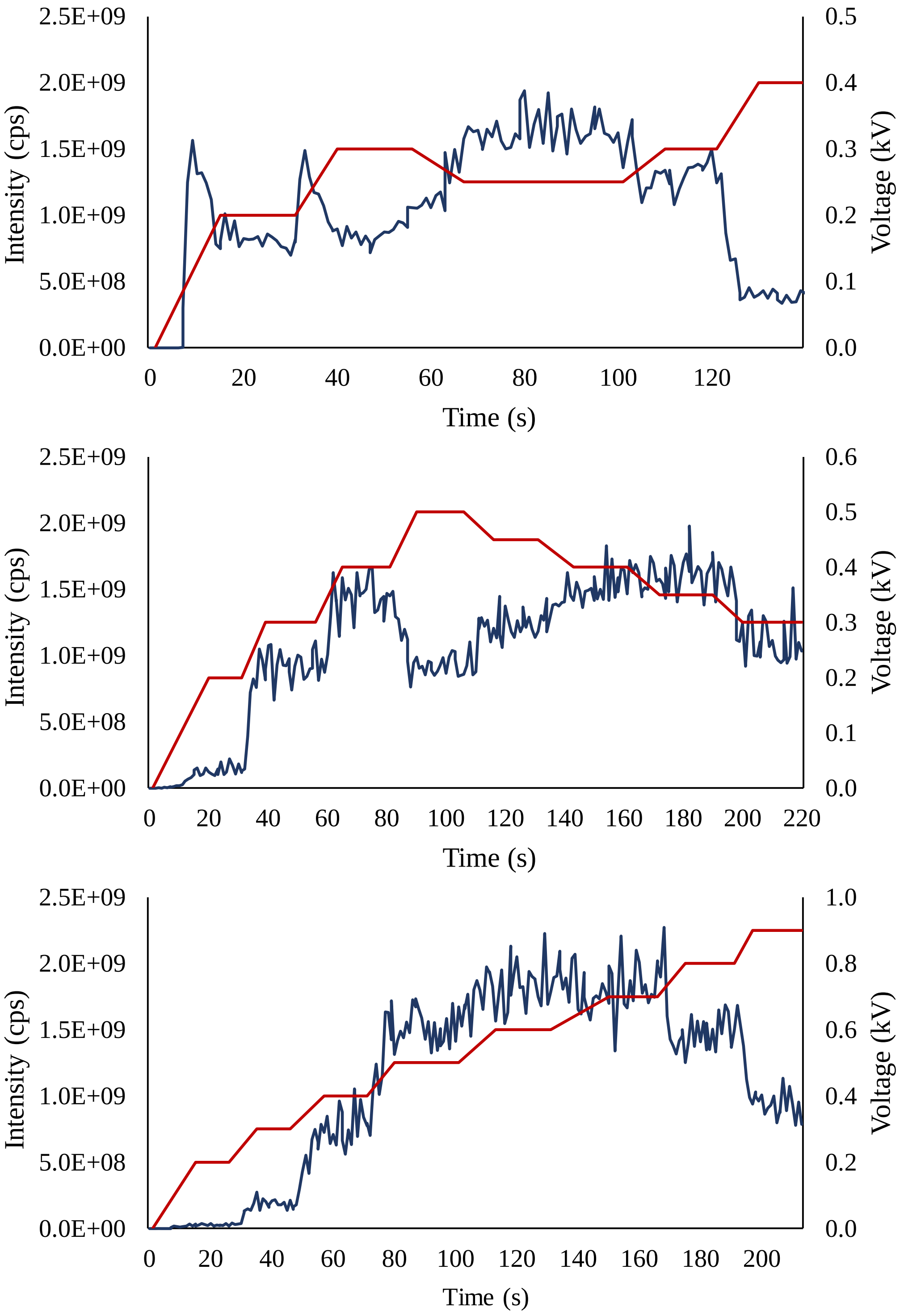

Figure 56: TIC chronograms (blue) for measurements with repeller 4 in three different positions (from top to bottom: A = closest to the spray exit, B = +5 mm, C = +10 mm) and without any additional ion source at different voltages (red).

During the previous optimization experiments with the ESI and the repellers on voltage, the optimal voltages had been between 1 and 2 kV for all tested flow rates from 50 to 450 µL min^{-1}. Surprisingly, the repeller voltages leading to the highest TIC response in the current experiment with only the APCI nebulizer were below 1 kV. Similarly to the previous measurements, it was noted that the required voltage necessary to reach the TIC signal intensity maximum increased with increasing distance from the nebulizing spray. However, the best results for each analyte were obtained with differing z-distances (cf. Appendix Table 19) because reserpine behaved differently than the compounds of lower *m/z* values.

For example, for repeller 2, which is the flat, slightly tilted repeller, in the upwards facing position, reserpine gave the highest signal response at the closest position to the nebulizing spray (cf. Figure 57 top) while the other detectable analytes caffeine, testosterone, and phenylalanine had their best responses at the position furthest away (cf. Figure 57 bottom). Repeller 2 was tested with the metal plate facing upwards and downwards. The upwards position gave overall higher peaks, while the downwards position did not give a pronounced mass spectrum for positions B and C.

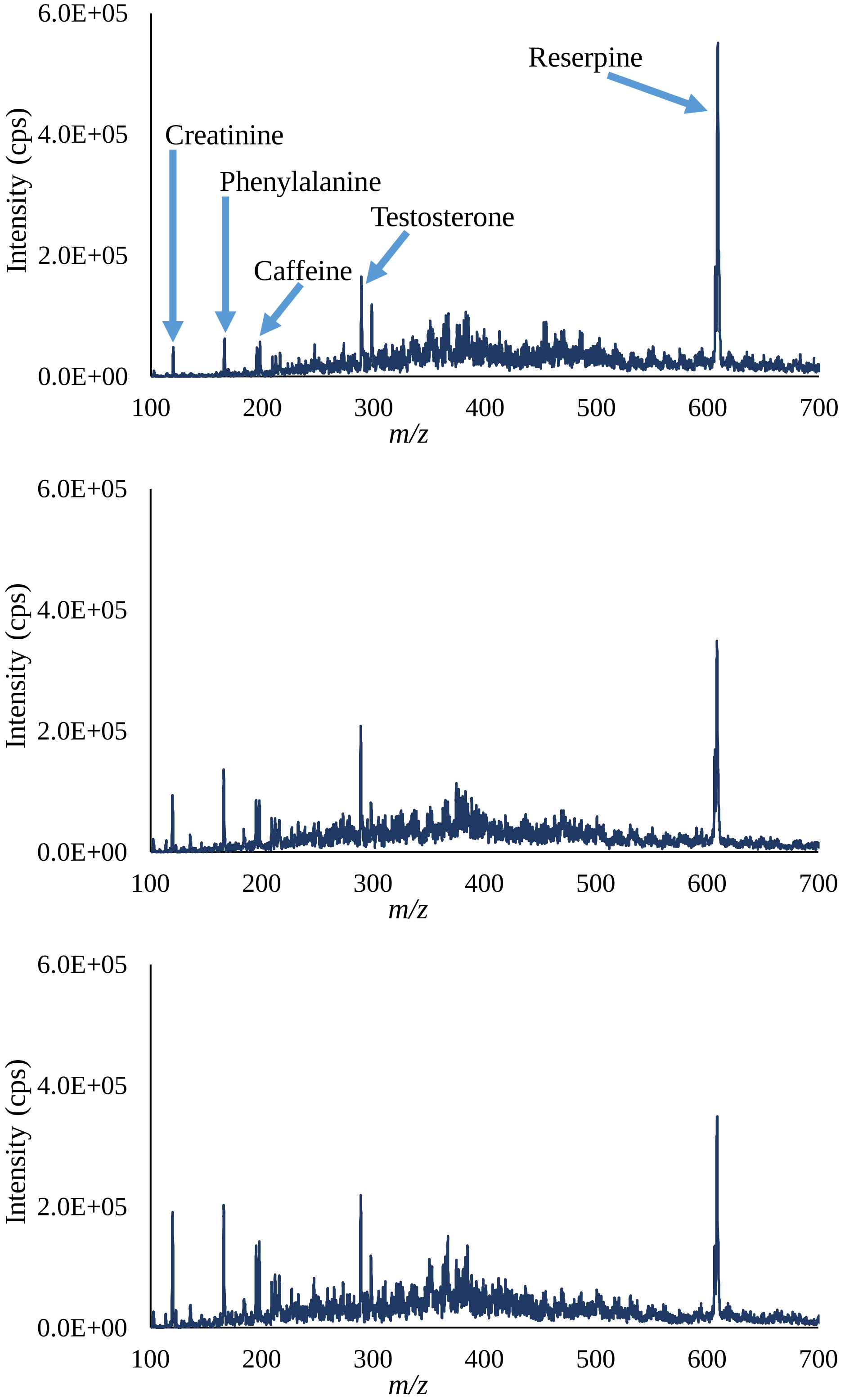

Figure 57: Averaged mass spectra for all three measured positions (top: A, middle: B (+5 mm), and bottom: C (+10 mm)) of repeller 2 (tilted) facing upwards at their respective best voltages 0.25, 0.3, and 0.4 kV.

Of all tested repellers, repeller 6 (rod, Ø 4 mm) required the highest voltages to reach a TIC intensity maximum (0.7 – 1.1 kV for positions A – C) and repeller 1 (flat, Ø 30 mm) required the lowest voltages (0.2 – 0.4 kV for positions A – C) (cf. Table 19).

The best responses in general are at different voltages than the voltages that had been found optimal during the previous repeller optimizations. Nevertheless, the fact that the repeller not only aids the ion transfer from the ESI needle to the mass spectrometer inlet but that it is capable of ionizing molecules itself is of vital interest.

For reserpine, the best responses were found with repeller 1 and repeller 6, and for testosterone and phenylalanine the best repeller was repeller 5. Caffeine was equally well detectable with repeller 2 in upwards position and repeller 5.

For comparison purposes, the same measurement was also performed using the APCI with the needle on voltage and without any repeller in the ion source. Surprisingly, the best results for the APCI needle were achieved at the lowest measured voltage, 3 kV. Table 20 in the appendix shows the relative peak heights which result from the peak heights obtained with the repellers divided by the peak heights obtained with the APCI. Since APCI ionization is not well suitable for reserpine, the relative detection of this compound is quite good, as is also depicted in Figure 58 which show the mass spectra obtained with the APCI (top) and with repeller 1 in position B (bottom).

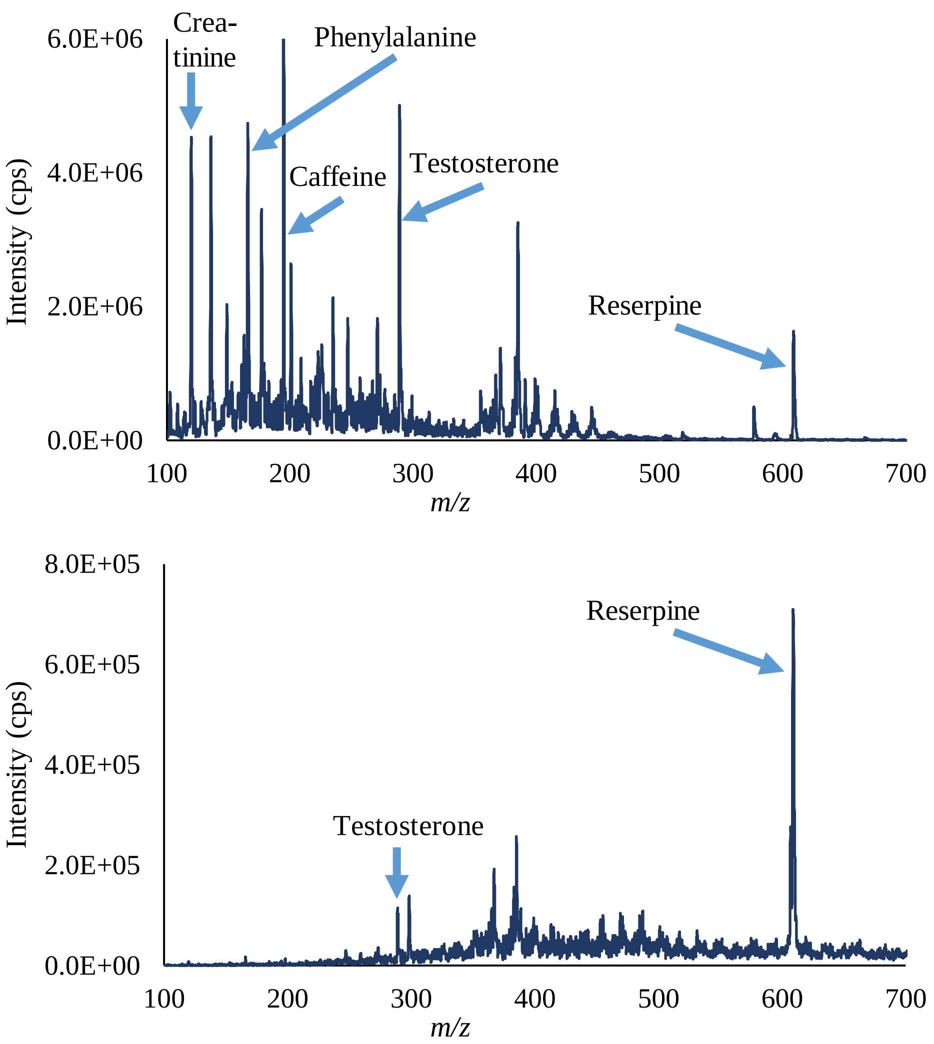

Figure 58: Averaged mass spectra for measurements with APCI at 3 kV (top) and repeller 1 in position B (= +5 mm) at 0.3 kV without APCI needle (bottom).

In the next experiment, the ESI ion source was combined with the repeller again, but now, no voltage was applied to the ESI capillary. Usually, the voltage difference between the capillary tip and the inlet of the mass spectrometer is responsible for the formation of the Taylor cone and thus the subsequent ionization of the analyte molecules.

The analyte solution was supplied in the same manner as in the APCI nebulizer experiment. All further parameters were as in Table 7. The repellers 1, 4, 5, and 6 were inserted in the position that had been found optimal with the syringe pump optimization experiments, and repellers 2 (facing upwards) and repeller 7 were inserted at the lowest height and at a z-distance of approximately 5 mm from the ESI capillary for Position A.

While the TIC curves reached a maximum at a certain voltage and then decreased again when increasing the voltage further for the APCI nebulizer, the TIC reached a plateau for most repellers and then decreased slightly when combined with the voltage-less ESI ion source. An exemplary chromatogram for repeller 5 (position C) with the APCI nebulizer and the voltage-less ESI is shown in Figure 59. For the APCI nebulizer, the voltage was continually increased which led to the TIC to increase at first and then decrease after 0.5 kV. For the ESI without capillary voltage, the voltage also decreased after having reached an intensity maximum, but when the voltage was increased further, it was found that the TIC would eventually reach a plateau around 3 kV before decreasing slightly. A similar trend regarding the plateauing of the TIC intensity when the voltage was high enough was found for repellers 1, 2 in upwards position, and 7. However, the TIC in repellers 4 and 6 decreased with increasing voltage after having reached a maximum, similarly to the responses obtained with the APCI nebulizer (cf. Appendix Figure 85).

The highest signal intensity for each analyte was often found at different voltages. Since most repellers reached an approximate plateau in which the peak height did not differ much, a best voltage was determined with special consideration to the peak heights of caffeine, reserpine, and testosterone. Except for repeller 6, all repellers required a higher voltage (0.5 – 2.9 kV) to reach the maximum response in comparison to the APCI nebulizer results (< 0.5 kV). The maximum peak heights for each repeller and the normalized peak heights (obtained by dividing the repeller results by the results obtained with the normal ESI) can be found in Appendix Table 21.

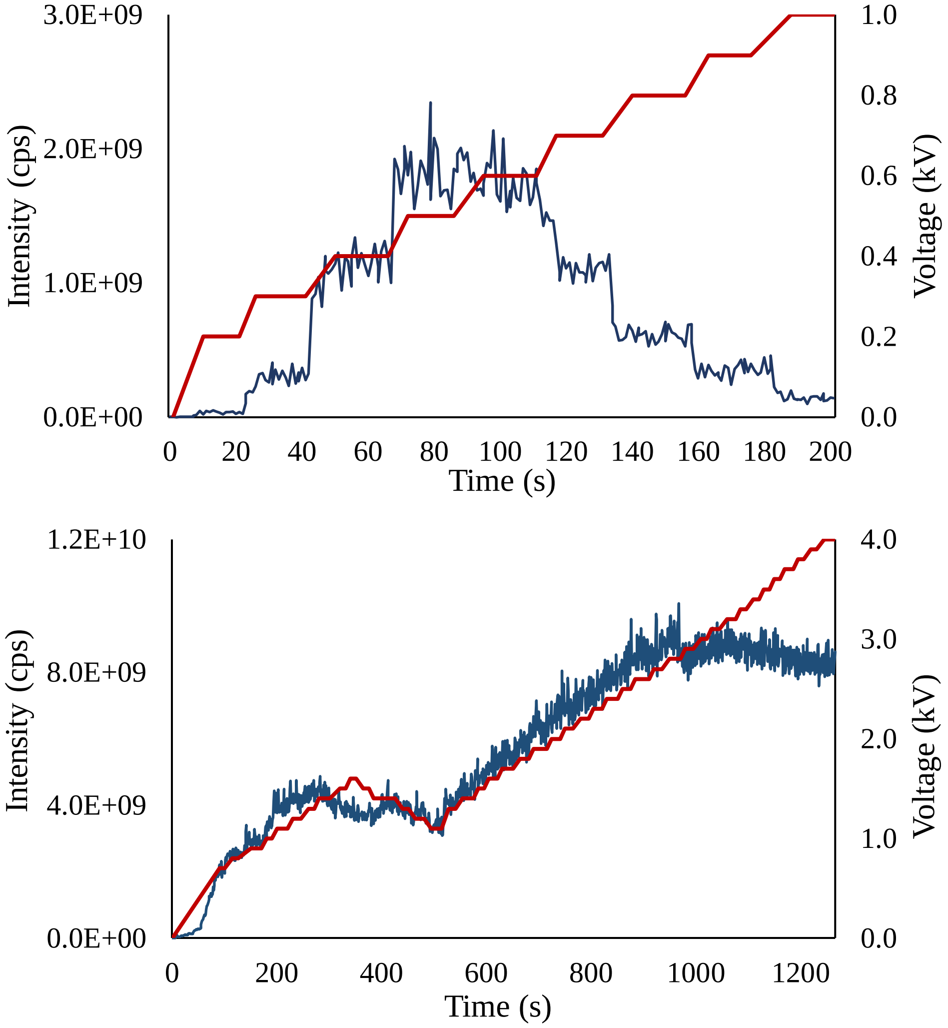

Figure 59: 200 µL min^{-1} test solution with the APCI nebulizer and repeller 5 in position C (top), as well as with the ESI without needle voltage and repeller 5 in its previously found optimal position (bottom).

As Table 11 shows, the ESI generally has a higher sensitivity than the APCI for all measured analytes. The highest peak heights obtained with the voltage-less ESI are also much higher than those obtained with the APCI nebulizer. The normalized values are also higher in nearly all cases for the ESI-set-up than for the APCI set-up. Since the required voltages, the differing peak heights, and the overall trend of the obtained signal responses for the ESI- and the APCI-set-up are so different, it has to be suggested that there is an effect happening between the repellers and the ESI capillary even when no voltage is applied to the capillary. The "true" ionization potential of the repellers is thus only demonstrated by the experiment with the APCI nebulizer since any other form of ionization can be excluded in this set-up.

Table 11: Peak intensities for the analytes measured via APCI, APCI-nebulizer with the best repellers 1 or 5, and ESI, voltage-less ESI with repeller 7, as well the normalized values obtained by dividing the peak results obtained with the repellers by the corresponding APCI or ESI values.

	APCI-set-up			ESI-set-up		
	Needle on 4 kV	**Only repeller**	**Normalized values**	**Capillary on 3 kV**	**Only repeller (R. 7)**	**Normalized ESI values**
Caffeine	6.6E+06	1.4E+05 (R. 5)	0.02	8.5E+06	5.0E+05	0.06
Reserpine	1.6E+06	7.1E+05 (R. 1)	0.35	1.9E+07	2.8E+06	0.15
Testo-sterone	5.0E+06	2.7E+05 (R. 5)	0.05	1.4E+07	1.2E+06	0.09
Phenyl-alanine	4.7E+06	2.4E+05 (R. 5)	0.05	7.7E+07	4.8E+06	0.06
Creatinine	-	-	-	5.2E+06	2.0E+06	0.38

Comparing the responses for each repeller by dividing the signal intensities obtained with the repellers in APCI-set-up and ESI-set-up, the ESI-responses are better in most cases (cf. Table 12).

Table 12: Peak intensities obtained with the APCI-set-up (optimal distances) divided by those obtained with the ESI-set-up for the different repellers.

	Repeller 1	Repeller 2	Repeller 4	Repeller 5	Repeller 6
Caffeine	-	0.40	0.25	0.65	-
Reserpine	0.37	0.18	0.98	0.37	1.33
Testosterone	0.13	0.27	0.35	0.46	0.31
Phenylalanine	-	0.07	0.10	0.38	-

Ionization without an intended ionization source present was also observed by McEwen *et al.* (2010). They performed laserspray ionization in which laser ablation of a matrix-analyte mixture produced ions similar to matrix-assisted laser desorption/ ionization (MALDI). They observed that in the absence of capillary or tube lens voltages, ions could still be observed as long as a voltage of 20 V was applied to the skimmer of an Orbitrap MS. They also reported that no laser ionization was necessary but that mere shockwaves, produced by shooting plastic pellets to the back of the sample plate, were sufficient to record ions.[132] They thus developed a matrix-assisted ionization method based on the use of a specific matrix and exposition of the sample to vacuum to generate ions similar to those created by ESI.[133]

For ESI, a potential difference needs to be established between the capillary, through which the analyte solution is flowing, and the inlet of the mass spectrometer. Usually, the voltage is applied to the ESI capillary in order to ionize the supplied molecules.[101] However, it is also possible to apply the voltage on the MS transfer capillary and put the ESI needle on ground which also allows the use of non-conductive materials for the ESI needle[134]. Having implemented a repeller electrode, it might have provided the required potential difference to the ESI capillary which was set to ground (0 kV). Thus, the typical ESI-type mechanism might have taken place, even though under suboptimal conditions in comparison to when the voltage is applied to the ESI capillary. Repeller 7 is the biggest repeller and thus automatically closest to the ESI needle which might explain why it gave the best results. This theory could also explain the improved results in contrast to pure repeller-ionization (which happened during the APCI nebulizer experiments) but worse results in contrast to “proper” ESI ionization which is performed under normal operating conditions.

The here implemented repeller electrode bears strong resemblance to SACI which was developed by Cristoni *et al.* (2003)[114]. They tested different repeller geometries of the same size, including planar, convex and concave metal surfaces, resulting in different ions in the case of the analyzed peptides. In their suggested mechanism, the metallic surface gets covered by solvent molecules and interacts with neutral analyte molecules which hence become charged. Another interesting feature in SACI is that the metallic surface is positioned in a 45 ° angle to the MS inlet which was unfortunately not possible to be tested within the present work due to time restraints. Likewise to the preliminary optimization experiments in the present work, the applied potential leading to the intensity maximum differed for each analyte. The best results were obtained with 150 – 300 V which is comparable to the optimal voltage that was found during the APCI nebulizer experiments (< 500 V)[135]. Furthermore, Cristoni and co-workers investigated the solvent type[135], pH, and nebulizing gas flow rate, and they also found that the best flow rate was below 80 µL min^{-1} which is supported to a limited extent by results of the present work[114].

6.3 Coupling of nanoESI and iLTP

In this proof-of-concept study, the sensitivity of a nanoESI-MS set-up was to be increased by coupling with a plasma-based ion source. Due to spatial restraints, an FµTP was built and incorporated in between the nanoESI frame and the mass spectrometer inlet as seen in Figure 60. In this way, the analyte-solvent spray exiting the ESI capillary passed through the plume of the plasma jet before entering the mass spectrometer. Unionized molecules are theorized to be thus ionized by the plasma, leading to a higher total ionization rate and thus higher sensitivity.

Since the used mass spectrometer in this project was a single quadrupole and the ambient ion source did not have a housing to shield it from environmental influences, the overall sensitivities are lower than in the previous two projects.

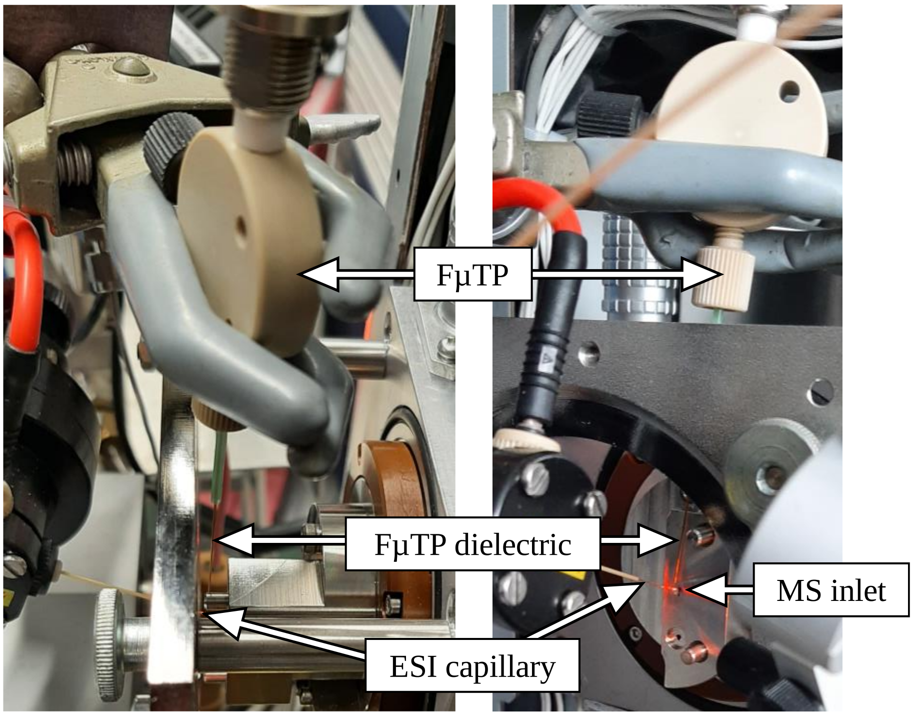

Figure 60: Coupling of a nanoESI ion source (from the front of the MS inlet) and an FµTP ion source (from the top of the MS inlet).

Unfortunately, the FµTP led to electrical short circuits with the mass spectrometer, leading to either erratic mass spectra (cf. Appendix Figure 86) or only an increase of the baseline and not of the analyte signal. One of the reasons might be that there was not sufficient insulation between the needle electrode and the MS inlet (AP1) which was operated at 80 V. While a TPI-configuration led to a “normal” background spectrum in contrast to the noise signal obtained with the FµTP, there were several reasons why eventually it was decided to continue with a plasma ion source in iLTP-configuration: The iLTP had previously been used in the first project of this doctoral work (Chapter 6.1) and could generally perform stable analyses. Furthermore, due to its bigger size, the HV needle electrode had to be placed further away from the MS inlet, probably contributing to the prevention of short circuits. The most important feature, however, was the ground electrode: The HV needle electrode was thus provided with a counter electrode, while operating an FµTP or TPI could lead to the MS inlet or ESI capillary working as ground electrode. This theory is supported by the fact that the TIC dropped to zero when the TPI was turned on at the same time as the ESI spray was operating and that in some measurements, the ESI capillary would stop spraying after turning the plasma off afterwards.

Therefore, the iLTP ion probe was mounted in front of the nanoESI-frame pointing in between the ESI capillary and MS inlet as shown in Figure 61. The entire set-up is shown in Appendix Figure 87.

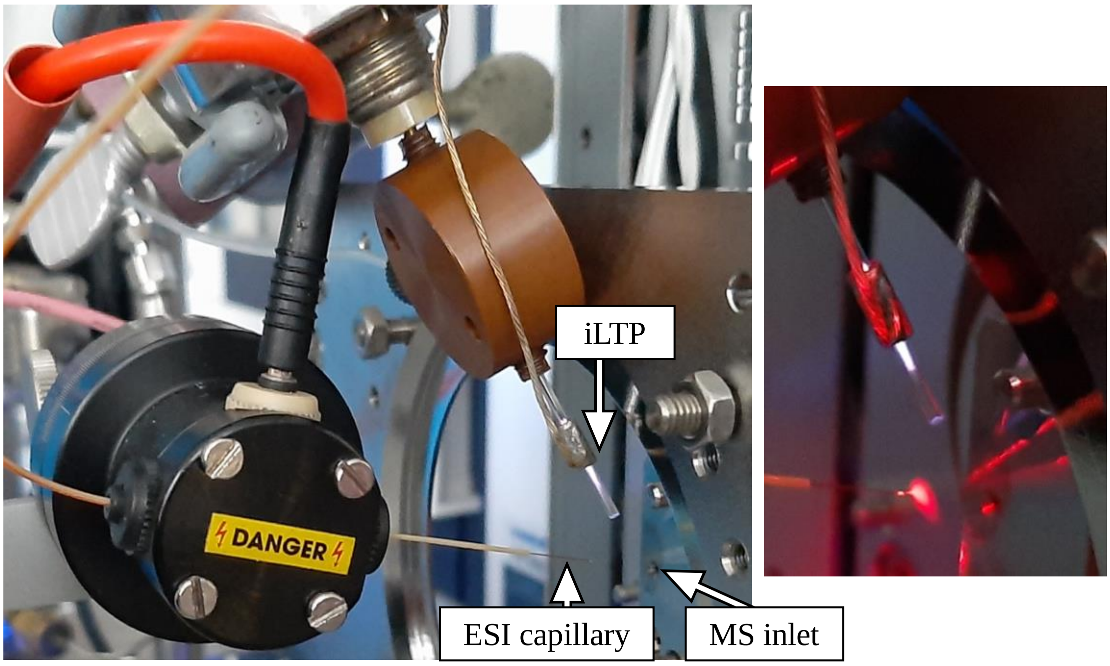

Figure 61: Coupling of the nanoESI with the iLTP ion source in front of the mass spectrometer. On the right, the ESI spray has been made visible with a laser pointer. The flow rate was 500 nL min^{-1}, the ESI ionization potential was 1.7 kV, and the plasma voltage was 1.3 kV.

One effect observed by integrating the iLTP ion source into the nanoESI-MS set-up were charging effects taking place at either the nanoESI capillary or the MS. For example, during a measurement in which the plasma frequency was changed from low to high and then back to low values, the reserpine signal in the averaged mass spectra constantly increased with time, independent of the plasma parameter (cf. Appendix Figure 88). This issue could be overcome by re-positioning the iLTP and the nanoESI. Due to the open design and the influences of the laboratory environment, the nanoESI position and voltage had to be readjusted for every measuring day in order to achieve a stable spray. Despite this, not every measurement day could lead to the same signal intensity despite keeping all other parameters unchanged. To thus reduce external influences, optimizations for one parameter were always executed on the same day. Furthermore, to counteract such charging effects, the plasma parameters were not changed within one run (except for the plasma voltages). This means that, in every measurement, during the first 20 min the ESI was operated alone, then the plasma was ignited under the conditions to be tested, and after 20 min, the ESI was operated alone again to check whether the TIC would fall back to its prior level and whether charging effects were successfully avoided. A typical TIC of such a measurement can be seen in Figure 62:

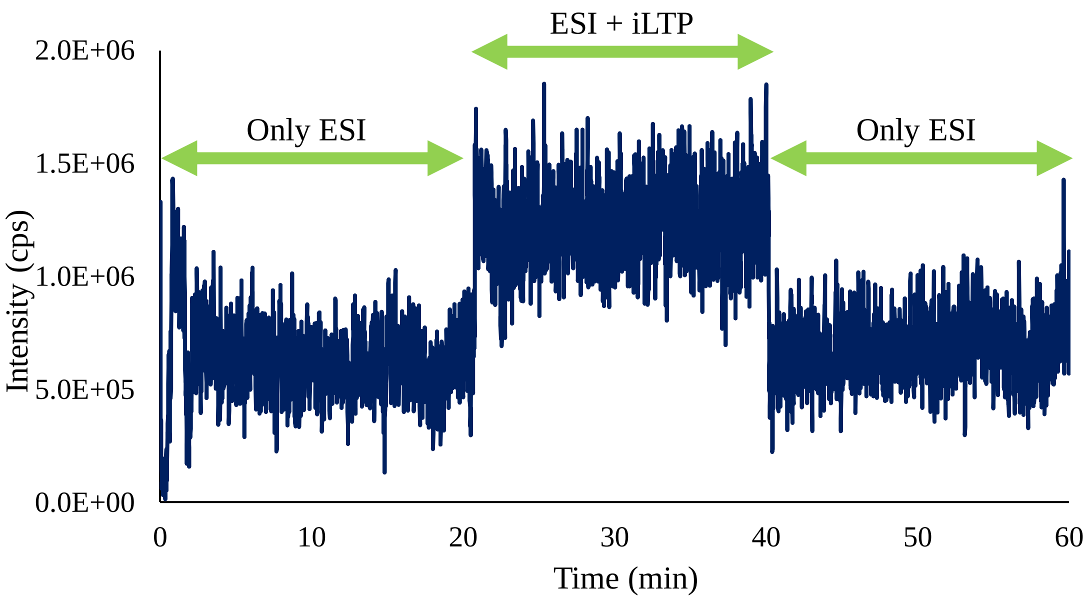

Figure 62: TIC of a measurement with only ESI, then with ESI + iLTP, and then again with only ESI. The ESI ionization potential was 1.8 kV and the nanoESI positioned at x = 7 mm, y = 1 mm, z = 10 mm, angle = 14°. The plasma was operated with a frequency of 12.5 kHz, pulse width of 50 µs, argon flow rate of 80 mL min^{-1}, and plasma voltage of 1.3 kV. The mass spectra in this and all following experiments were averaged over 15 min.

At first, frequency and pulse width were optimized. Figure 63 shows the peak heights of reserpine for each step of the measurement. Since the relative increase was biggest for 12.5 kHz and 50 µs, it was continued with these parameters (cf. Appendix Table 22).

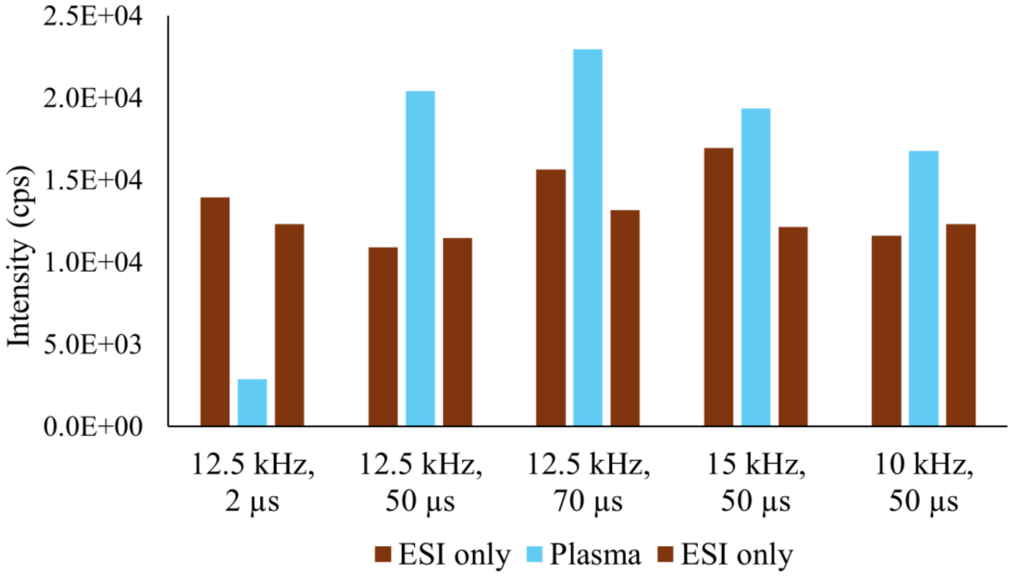

Figure 63: Measurements with only ESI and ESI + iLTP under different plasma conditions. The ESI ionization potential was 1.8 kV and the nanoESI positioned at x = 7 mm, y = 1 mm, z = 10 mm, angle = 14°. The plasma was operated with an argon flow rate of 80 mL min^{-1} and a plasma voltage of 1.8 kV.

Next, the plasma voltage was optimized. In between measuring with only ESI, the iLTP was ignited and the plasma voltage was increased in 0.2 kV steps. Due to the size of the syringe, the measurements were restricted to 100 min and only three voltage levels could be tested in each run. Therefore, the last tested voltage was repeated in the next measurement to check for possible charging effects. As can be seen in Figure 64, the best voltage was around 1.7 – 1.9 kV. The differences in peak heights between ESI measurements and the ESI + iLTP measurements under equal conditions might be explained by normal oscillations due to the ambient set-up. It was continued with a plasma voltage of 1.8 kV. To check the validity of these results, 1.9, 1.5 and 2.3 kV were tested in this order on the same measurement day and gave the same trend (cf. Appendix Figure 89).

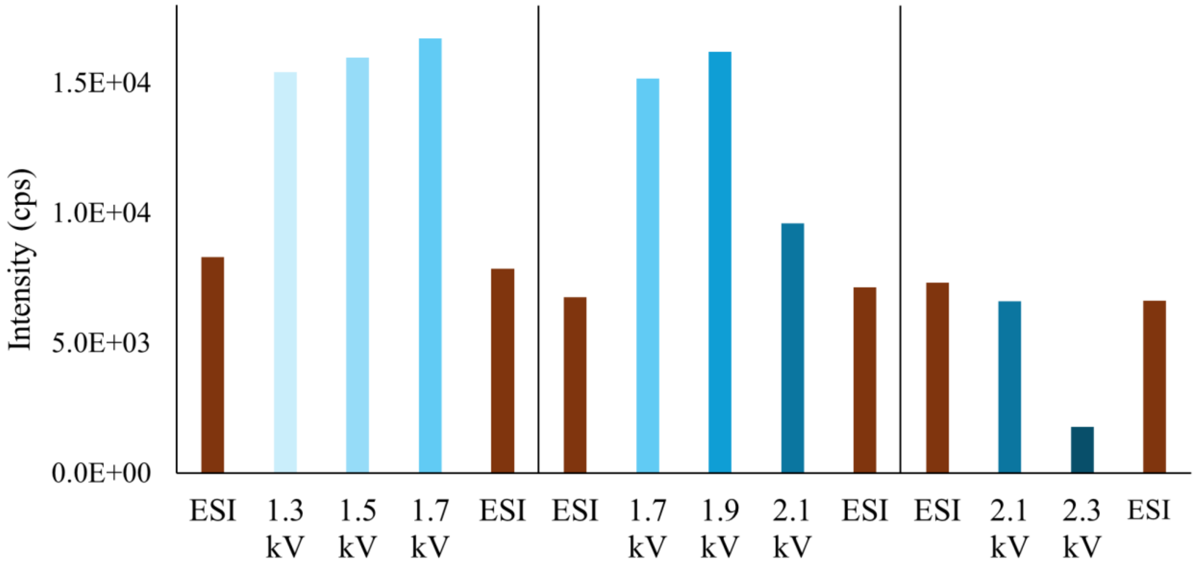

Figure 64: Measurements with only ESI and ESI + iLTP with different plasma voltages. The ESI ionization potential was 1.8 kV and the nanoESI positioned at x = 7 mm, y = 1 mm, z = 10 mm, angle = 14°. The plasma was operated with a frequency of 12.5 kHz, pulse width of 50 µs, and argon flow rate of 80 mL min^{-1}.

The iLTP used here had previously been used in the project to develop a new nebulization system and had been operated with an argon flow rate of 200 mL min^{-1}. The FµTP in the current project had been operated with 80 mL min^{-1} which is why the iLTP probe was also used with 80 mL min^{-1} so far. One aspect to be considered was that a flow rate too high would “push” the analyte spray exiting the ESI capillary downwards. Therefore, argon flow rates between 40 and 120 mL min^{-1} in 20 mL min^{-1} steps were investigated. Previously, the argon flow rate had already been turned on during the pure ESI measurements in order to have similar conditions to the ESI + iLTP measurements. To check whether the argon flow influenced the ESI spray, in the following measurements, the following conditions were tested for 20 min each: Only ESI, first without argon flow through the dielectric tube of the iLTP and then with argon flow, then ESI + iLTP, then again only ESI, first with and then without argon flow, as depicted in Figure 65 for the TIC of the 80 mL min^{-1} measurement. Figure 66 shows the averaged reserpine peak heights for all measured argon flow rates. Based on the ratio of reserpine peak height during plasma operation to the ESI only measurements, 80 mL min^{-1} proved to be optimal (cf. Appendix Table 23). There also did not seem to be a big influence of the argon gas flow onto the ESI spray.

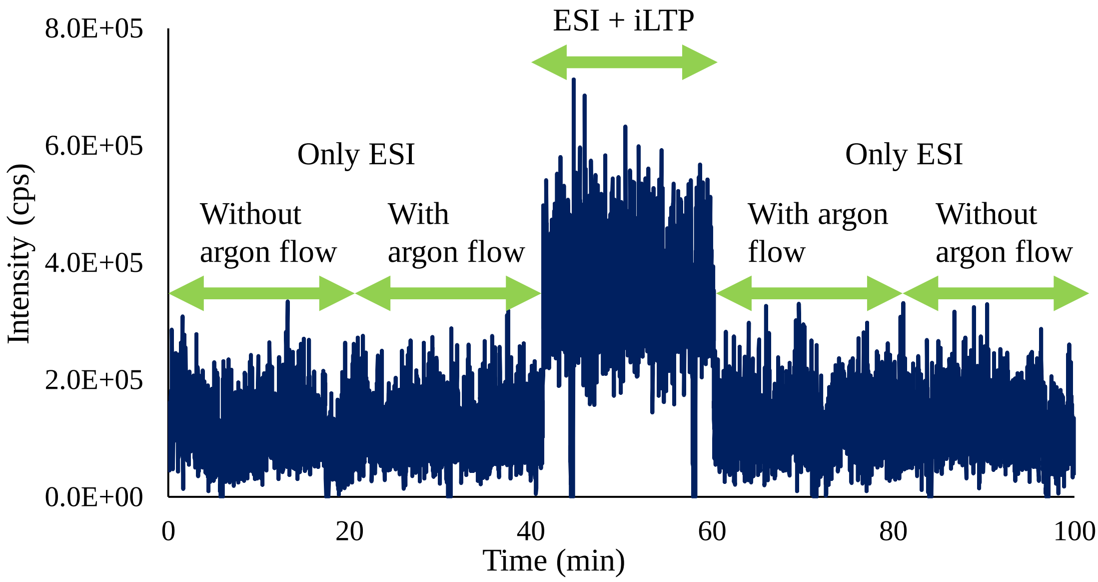

Figure 65: TIC of a measurement with only ESI, without and with argon flow through the iLTP dielectric tube, then with ESI + iLTP, and then again with only ESI with and without argon flow. The ESI ionization potential was at 1.8 kV and the nanoESI positioned at x = 7 mm, y = 1 mm, z = 11 mm, angle = 14°. The plasma was operated with a frequency of 12.5 kHz, pulse width of 50 µs, argon flow rate of 80 mL min^{-1}*, and plasma voltage of 1.8 kV.*

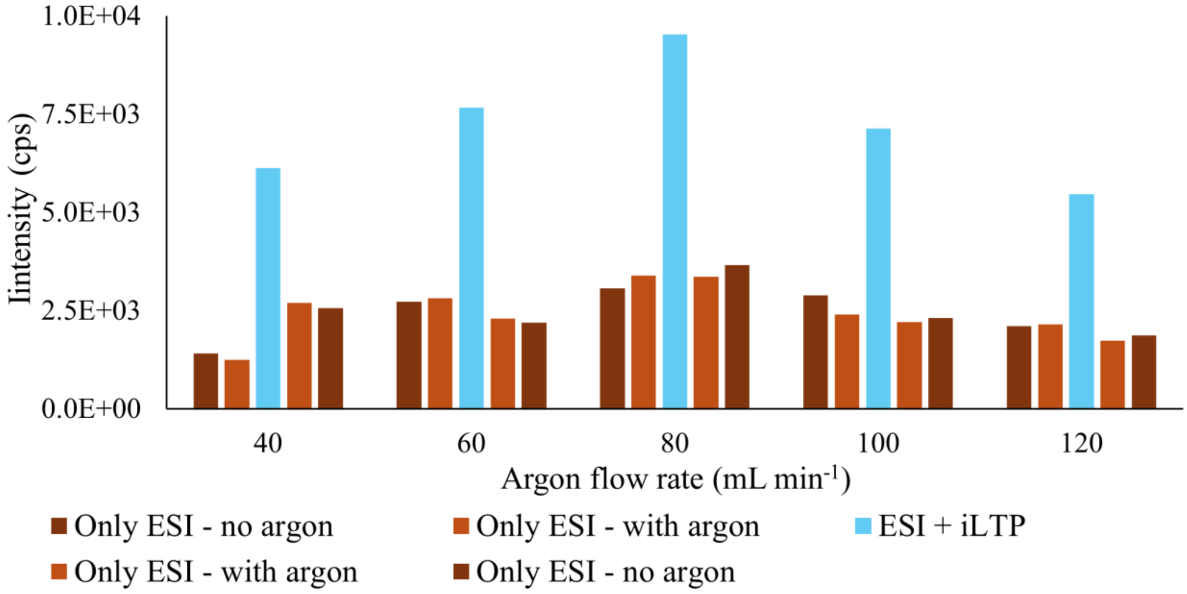

Figure 66: Reserpine peak heights in averaged mass spectra for different iLTP argon flow rates. The ESI ionization potential was at 1.8 kV and the nanoESI positioned at x = 7 mm, y = 1 mm, z = 11 mm, angle = 14°. The plasma was operated with a frequency of 12.5 kHz, pulse width of 50 µs, and plasma voltage of 1.8 kV. Due to environmental influence, the plasma ignited between 1.8 and 2.3 kV on this measuring day and was then turned down to 1.8 kV.

With the optimized conditions, a calibration curve was established testing reserpine concentrations ranging from 1 to 1000 µg L^{-1}. The lowest measured concentration for which reserpine peaks were visible was 250 µg L^{-1} as shown in Figure 67 and the calibration curve is depicted in Figure 68, illustrating that the addition of an iLTP in between ESI capillary and MS leads to an increase in signal response.

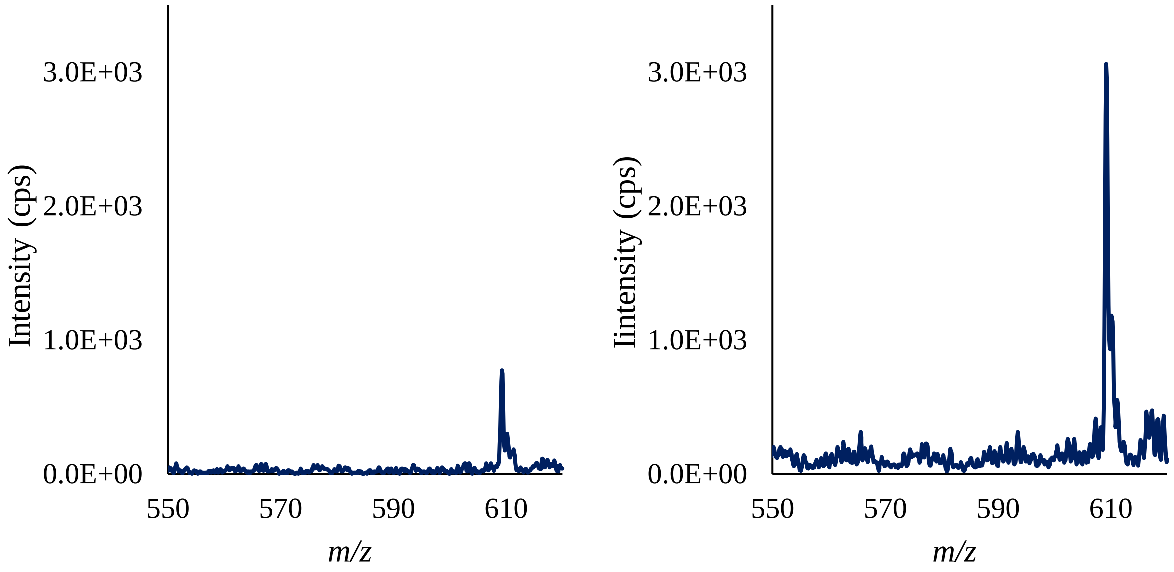

Figure 67:Mass spectra showing the 250 µg L^{-1} reserpine peak measured with only ESI (left) and ESI with iLTP (right). The ESI ionization potential was 1.8 kV and the nanoESI positioned at x = 7 mm, y = 1 mm, z = 10 mm, angle = 14°. The plasma was operated with a frequency of 12.5 kHz, pulse width of 50 µs, argon flow rate of 80 mL min^{-1}, and plasma voltage of 1.8 kV.

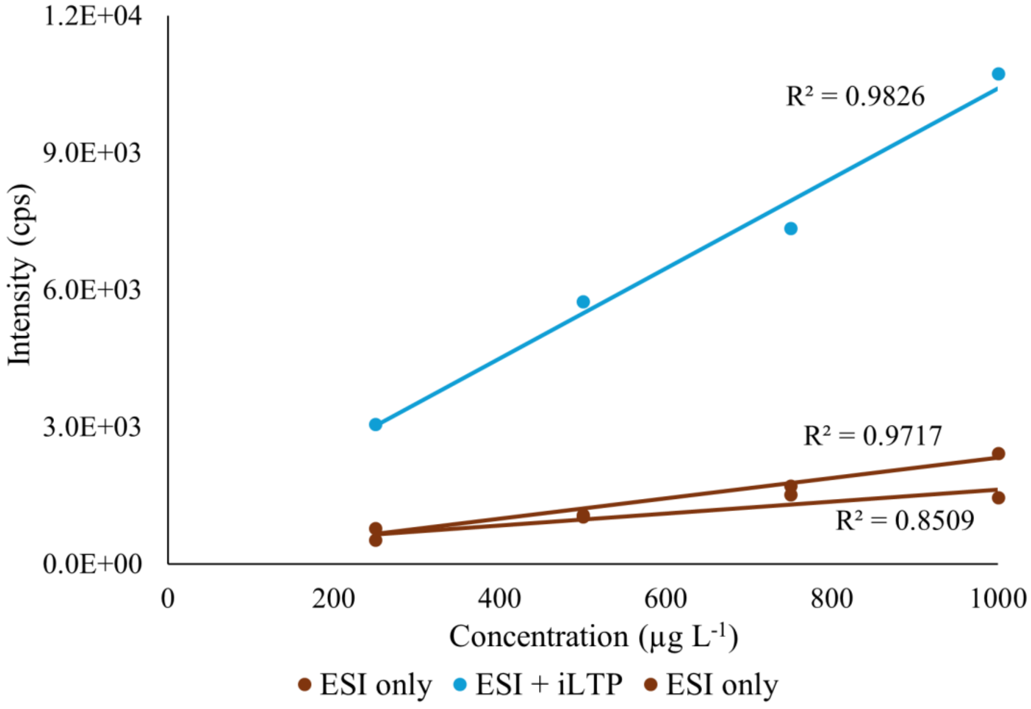

Figure 68: Calibration curve for 250 to 1000 µg L^{-1} reserpine under optimized conditions.

7. Conclusion and Outlook

In the present work, the analysis of a set of standards with atmospheric pressure ion sources, an iLTP and an ESI ion source, as well as the combination of both, were to be enhanced.

In the first project, two commercial nebulizers were adapted to introduce the analytes from LC to an iLTP ion source. Based on these results, a new nebulizer was developed with our cooperation partner Hitachi High-Tech, and a guidance cone was designed and attached to improve the focusing of the analyte onto the plasma region. This newly developed nebulization system did not reach the same level of sensitivity as the standard APCI vaporizer. Reasons for that can be the droplet size and possibly the occurrence of condensation of the molecules after exiting the heated guidance cone region. In order to facilitate the ionization further, a mesh guaranteeing smaller solvent droplets should be used. To ensure the gas phase of the molecules, the ion source housing itself could be heated and the path the molecules have to travel to the MS inlet should be reduced by miniaturizing the entire ion source. An important consideration in the heating of the ion source housing are the effects that altered atmospheric conditions might have on the plasma chemistry and thus the ionization of the analyte molecules. If the ion source will be used in routine analysis, the throughput must be increased by developing a nebulization method that is able to spray bigger amounts of liquids in a shorter period of time. For this endeavor, the regularity of the mesh vibration has to be improved and a dead-volume-less and leak-free solvent introduction must be developed. Alternatively, the developed nebulizer could be employed with a nanoLC using smaller eluent flow rates.

The use of the TPI configuration showed the potential of this ion source in comparison to the previously developed iLTP ion source. The TPI was not fully optimized in the present experiments yet and might even reach better results in the future. A full-out chemometric comparison of all ion source designs might also aid in future investigations of DBD-based ion sources.

In the second project, the ion transmission into the MS inlet was improved by implementing a repeller electrode into the ESI ion source housing and optimizing its shape, spatial position and applied voltage. During the course of the optimization procedure the role that analyte *m/z* and supply flow rate play in the signal detection and application of voltage were investigated. Further studies would be necessary in order to understand the exact influence of the presence of a repeller electrode in atmospheric pressure ion sources. Theoretical modelling of the gas flows and electric fields would be of tremendous advantage in order to explain the behavior of molecular ions travelling from the ESI capillary to the MS inlet. It could also aid in the development of new repeller shapes.

The effect of the repeller electrode was found to be advantageous at lower flow rates. Like the development in the first project, it could better be implemented in a nano-sized instrument and/ or be combined with other low flow rate applications. Furthermore, detailed studies regarding the influence that *m/z* and collision cross section of the molecules have on the repeller would help to design a compound-specific improvement of signal detection.

The investigation of real samples could be expanded, and sample preparation would help to reduce the contamination of the MS during the measurements. As it was found that the repeller electrodes themselves possess the capability of ionizing molecules, this phenomenon should be further investigated as well and supported by theoretical modelling if feasible.

The third project served as a proof-of-concept study to combine both types of ionization sources used in the previous projects by integrating a plasma ion source in between the tip of a nanoESI capillary and the inlet of a mass spectrometer. The idea was it to ionize the molecules that had not been ionized beforehand by the ESI mechanism and thus increase the ionization yield and with that the sensitivity of the method. Different types of ion sources were tested, and it was found that an iLTP-configuration seemed the most promising due to its counter electrode. Despite the precarious set-up and the ambient setting prone to external influences, the iLTP probe could be successfully positioned and operated. The optimization and subsequent calibration showed that the use of iLTP did indeed increase the ionization yield and led to higher intensities regarding the test compound reserpine.

To put it in a nutshell, two ion sources were aimed to be enhanced by altering the nebulization of the analyte molecule or by improving the ion transmission into the mass spectrometer inlet via a repeller electrode. It was also shown that both types of ion sources could be successfully combined to increase the ionization yield. These projects have demonstrated first successful implementations of all developments and paved the way for possible further improvements of ion sources which might show the potential of competing with established ion source designs.

8. List of Figures

9. List of Tables

10. Appendix

10.1 Ultrasonic nebulization

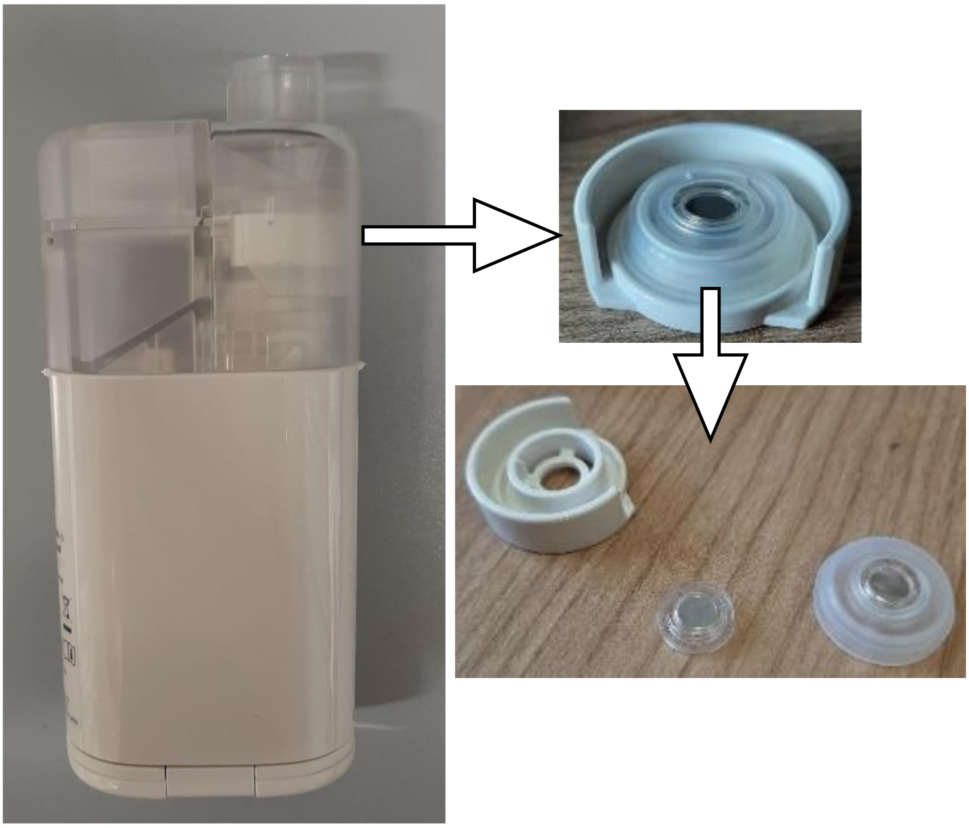

Figure 69: Commercial MicroAir U100 mesh nebulizer from Omron (left). Mesh in its holding system consisting of three different parts extracted from the commercial nebulizer device (right).

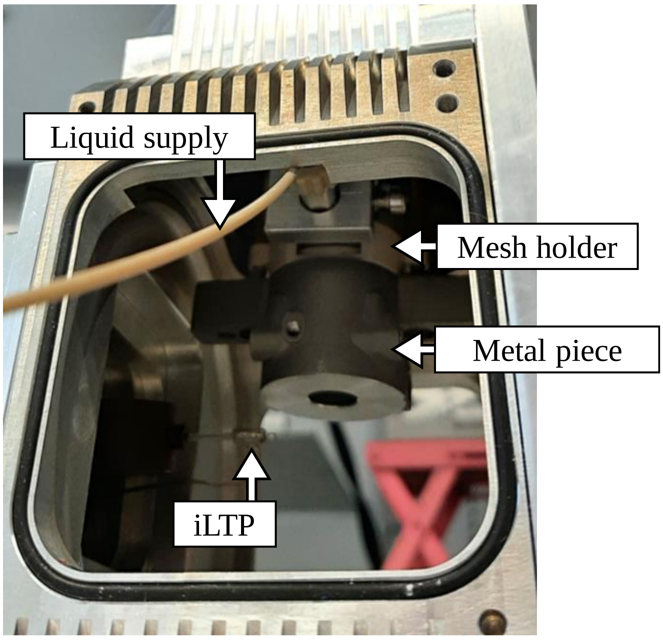

Figure 70: Extracted Omron set-up in the ion source housing. (The brightness and contrast in this picture were altered for better visualization.)

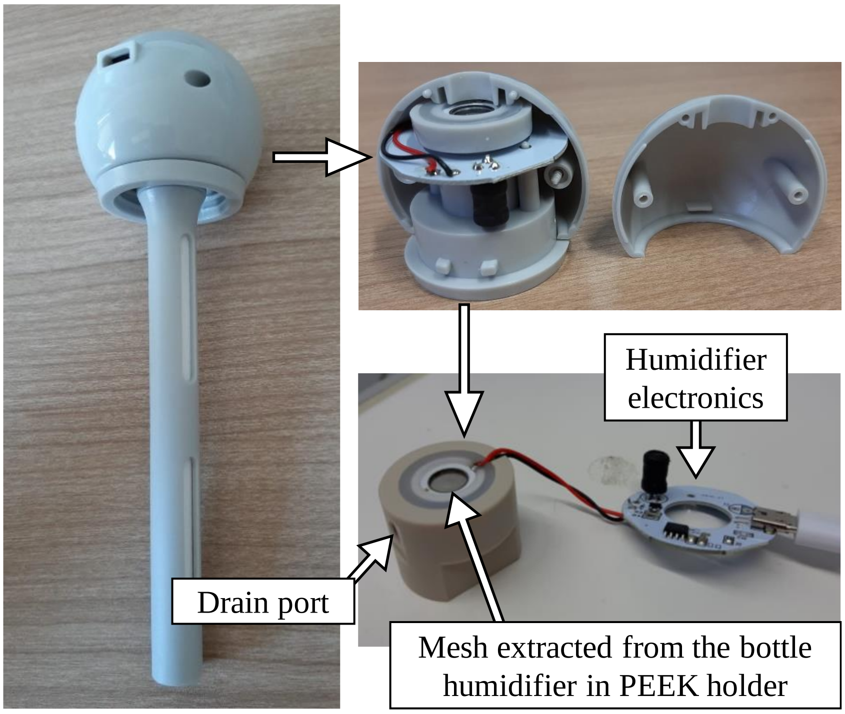

Figure 71: Commercial bottle humidifier of the company Daiso (left). Partially disassembled bottle humidifier in order to extract the mesh in its commercial plastic holder and the electronic circuit board (top right). Bottle humidifier mesh in its commercial plastic holder inserted into a PEEK holder provided by Hitachi HT (bottom right).

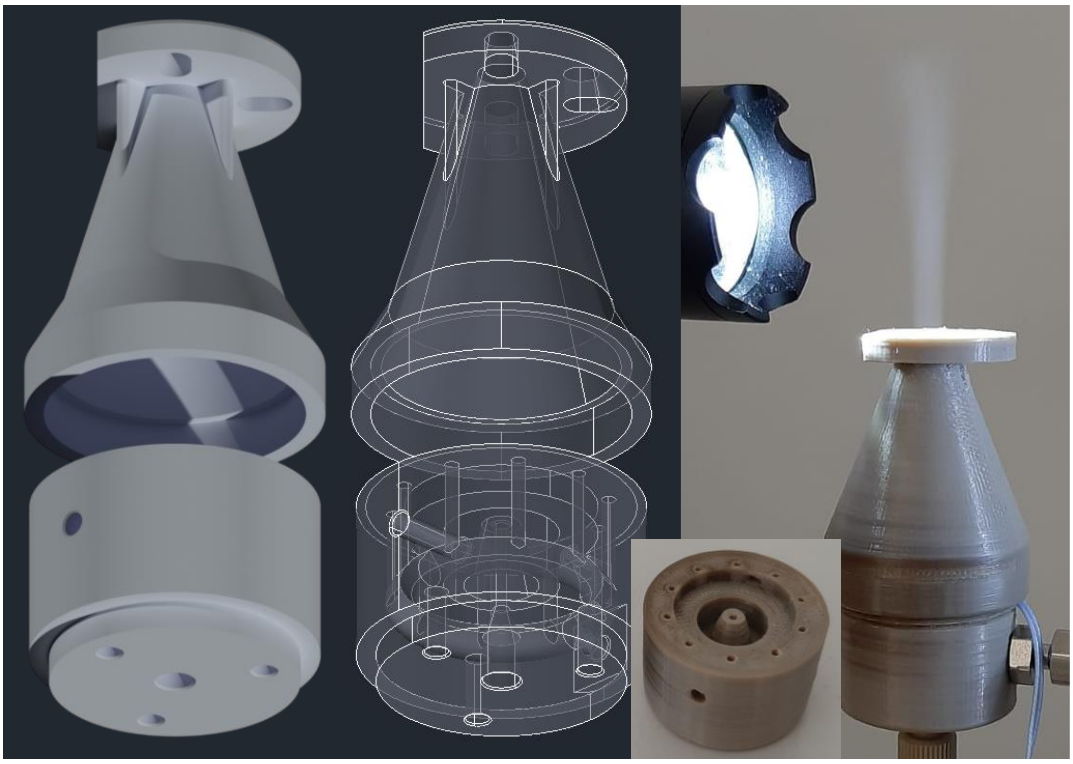

Figure 72: Focusing cone for the sprayed liquid in rendered view (left), X-ray view (middle), and operating with a flowing liquid supply and auxiliary nitrogen gas (entry at the side).

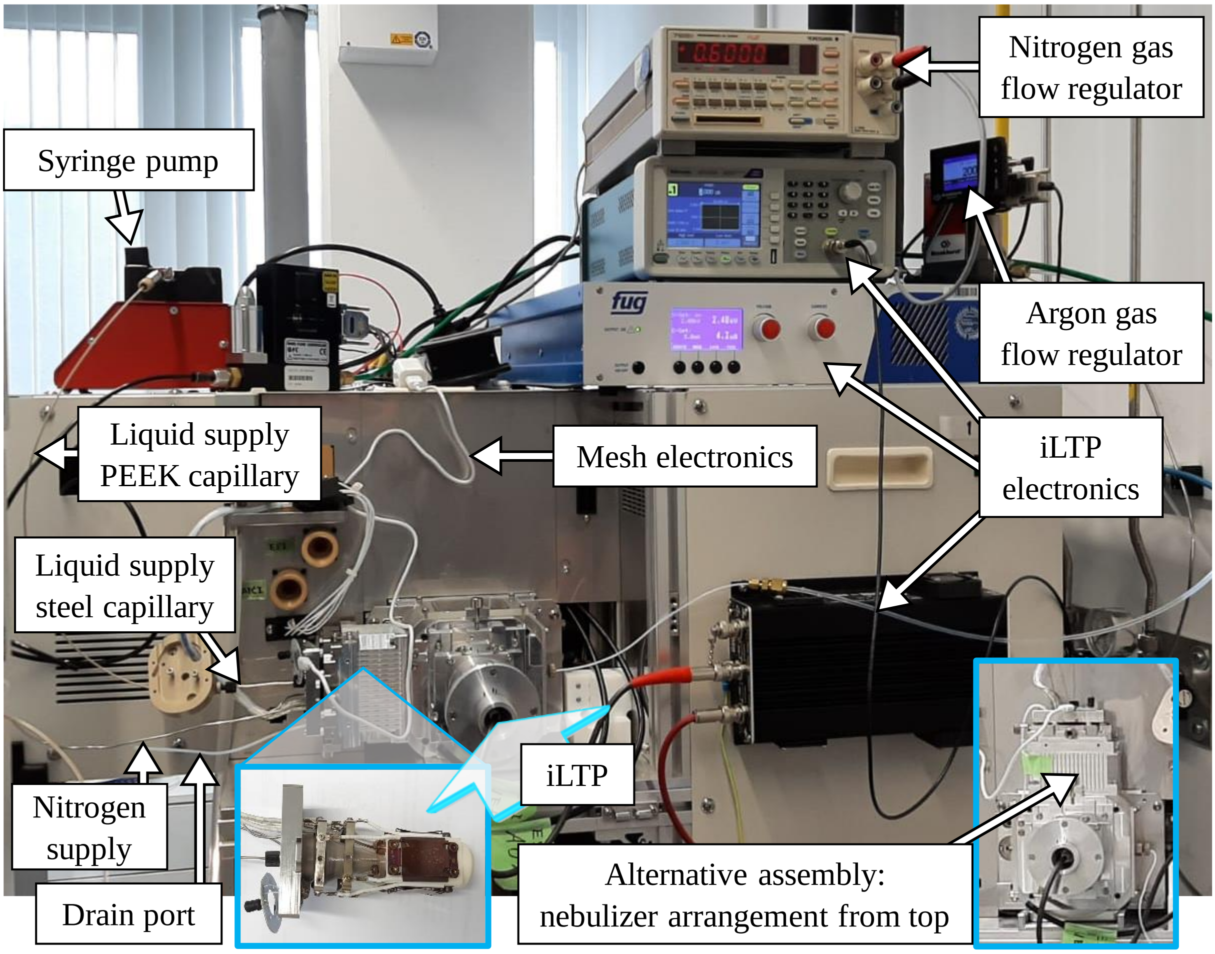

Figure 73: Experimental set-up of the humidifier-USN at the side (and top) of the iLTP ion source housing in front of the mass spectrometer. In this arrangement, the liquid supply is connected to a syringe pump. The auxiliary nitrogen gas is provided by the mass spectrometer and unheated.

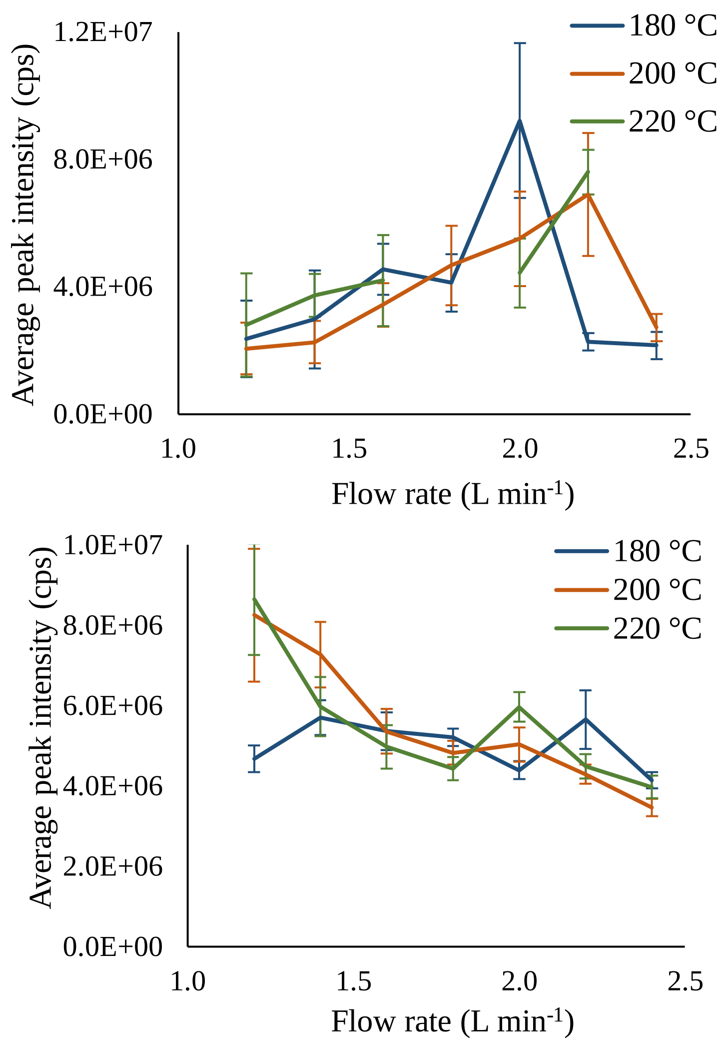

Figure 74: Average peak intensity of 1 mg L^{-1} caffeine (top) and 100 µg^{-1} L caffeine (bottom) measured via syringe pump with the USN mounted from the side (top) and top (bottom). When the mesh vibration was too irregular, no average intensity could be calculated.

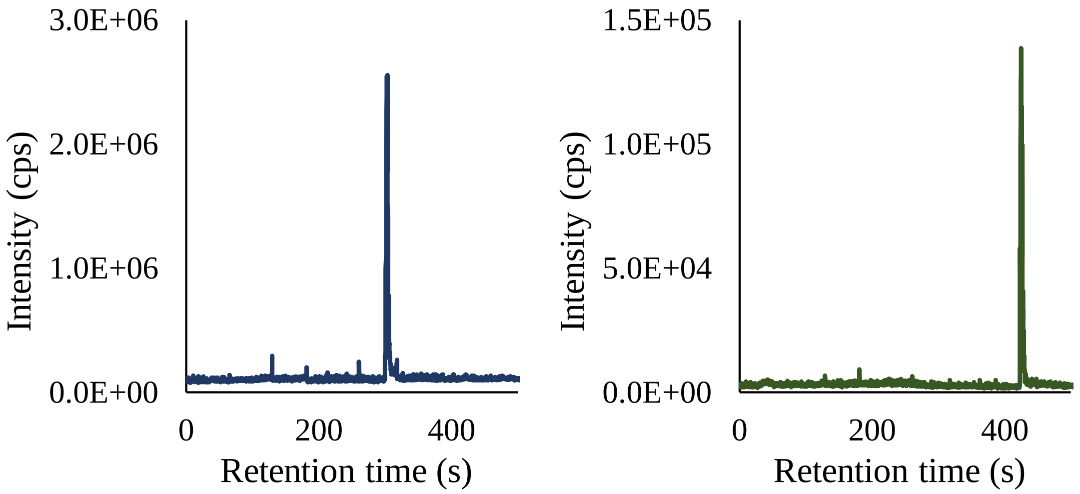

Figure 75: Exemplary chromatograms for 100 µg L^{-1} caffeine and 500 µg L^{-1} reserpine via LC-gradient.

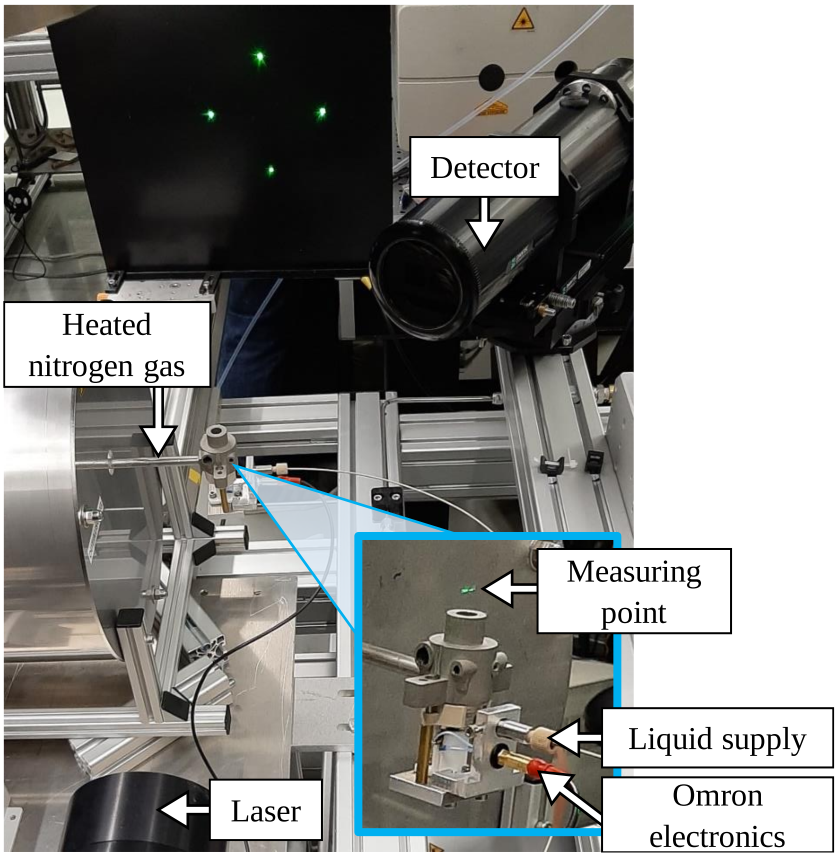

Figure 76: Set-up of the PDA experiment using the extracted Omron.

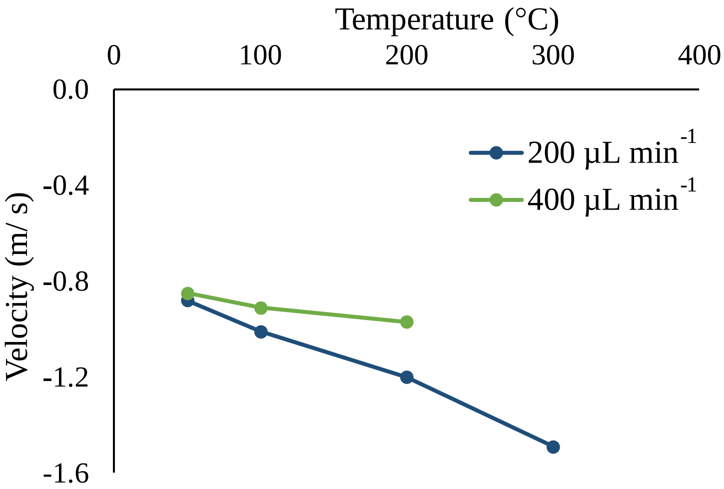

Figure 77: Average droplet velocity in dependence of the temperature to which the nitrogen heater was set for the Omron nebulizer. The nitrogen gas flow rate was 2.5 L min^{-1}.

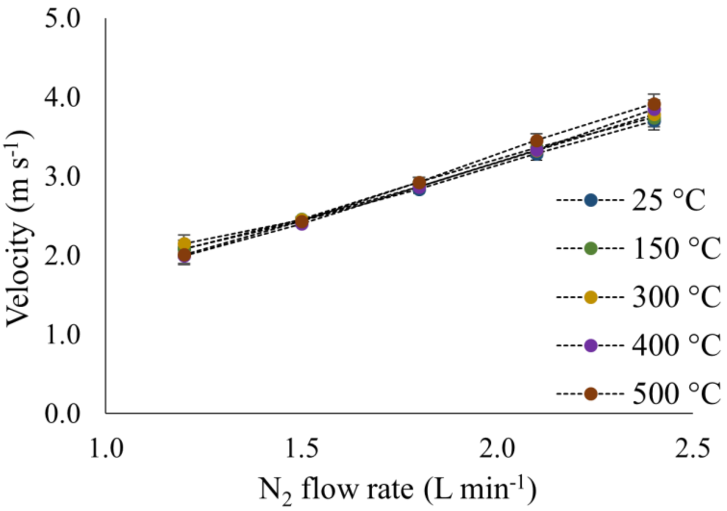

Figure 78: Average droplet velocity in dependence of nitrogen flow rate and temperature to which the nitrogen heater was set for the humidifier nebulizer. Due to heat loss, there was probably not a high temperature difference at the measuring point.

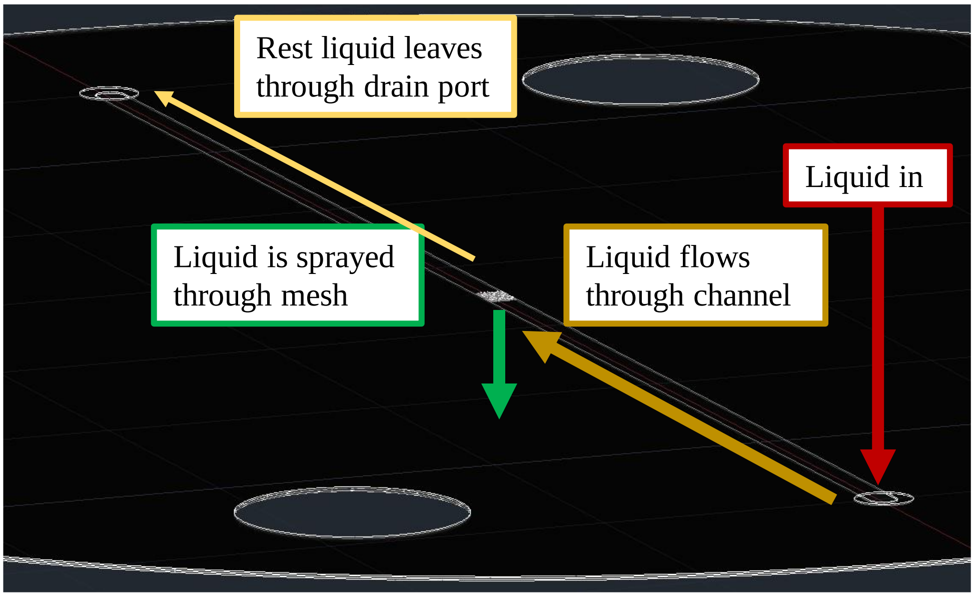

Figure 79: Three-dimensional view of the Hitachi-built USN consisting of a metal plate with three layers. The liquid flows into the channel in the middle layer and due to the vibration of the metal plate, it is sprayed through the mesh in the middle.

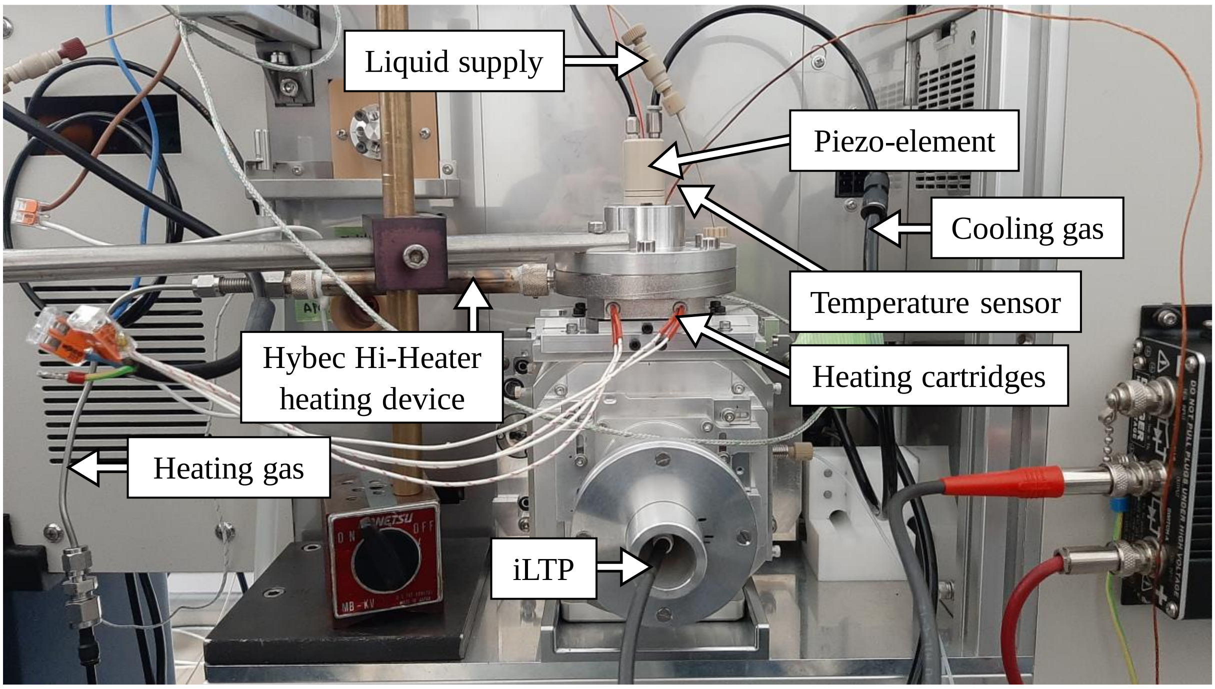

Figure 80: Experimental set-up of the LC-iLTP-MS experiments with cone B and the Hitachi nebulizer.

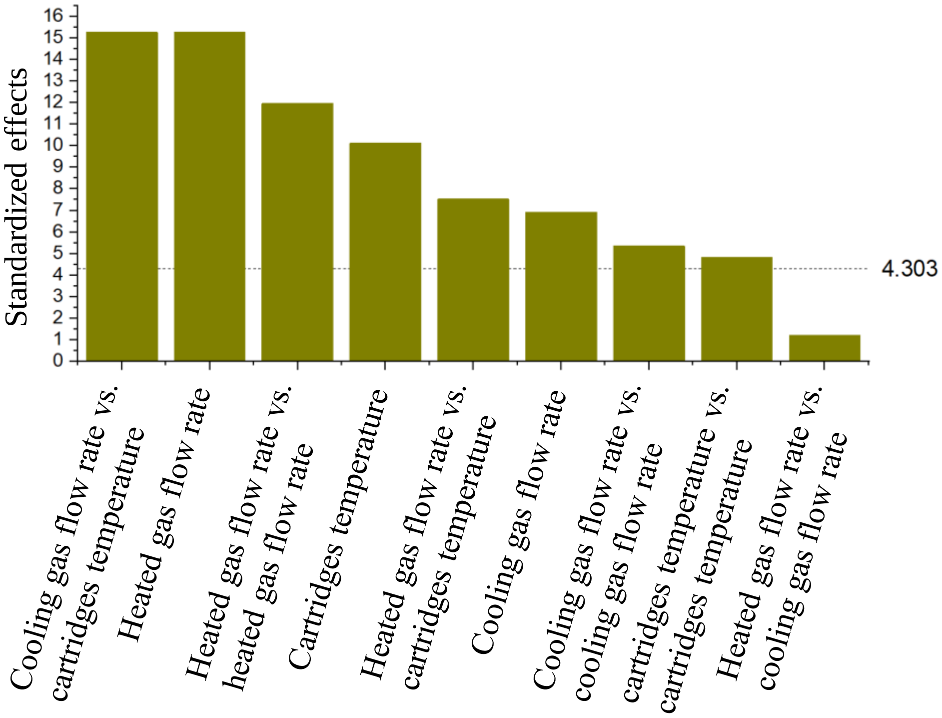

Figure 81: Standardized effects plots for testosterone. Any column over the marked threshold has a significant influence on the peak area.

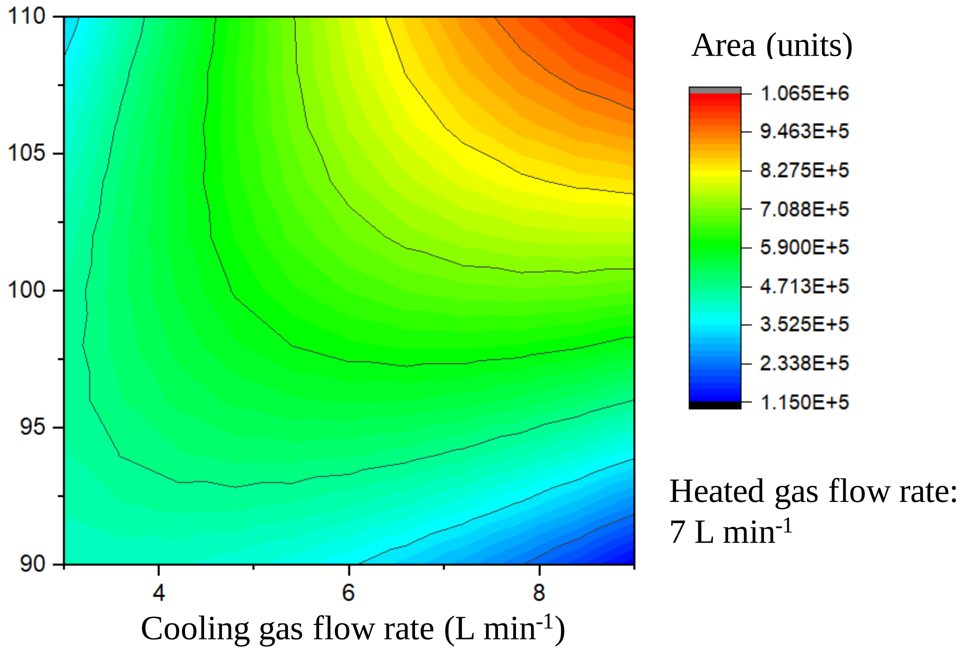

Figure 82: Contour plot for the influence of heating cartridges temperature and cooling gas flow rate on the peak area of testosterone. The heated gas flow rate was kept at the optimal value of 7 L min^{-1}.

Table 13: Figures of Merit for three measurement days for caffeine and testosterone via UPLC-USN-cone B-iLTP-MS.

Caffeine						
	Day 1	Day 2	Day 3	Average	Std. dev.	RSD (%)
iLOD (µg L^{-1})	14	31	32	26	10	39
iLOQ (µg L^{-1})	64	72	100	79	19	24
R^2 ((areal units per µg/ L)^2)	0.999	0.9988	0.992	0.997	0.00398	0.4
Sensitivity (µg/ L per areal units)	8.43E-04	6.88E-04	5.94E-04	7.08E-04	1.26E-04	18

		Inter-day			Intra-day	
Precision	Std. 4	8	-	18	18	%
	Std. 6	10	2	8	9.5	%
	Std. 8	10	14	15	17	%
Trueness	Std. 4	11	-	38	0.2	%
	Std. 6	7	-3	13	0.1	%
	Std. 8	6	6	33	0.1	%

Testosterone						
	Day 1	Day 2	Day 3	Average	Std. dev.	RSD (%)
iLOD (µg L^{-1})	47	41	36	41	6	13
iLOQ (µg L^{-1})	120	130	149	133	15	11
R^2 ((areal units per µg/ L)^2)	0.9994	0.9952	0.992	0.996	0.00371	0.4
Sensitivity (µg/ L per areal units)	1.96E-03	1.14E-03	2.74E-03	1.94E-03	7.97E-04	41

		Inter-day			Intra-day	
Precision	Std. 4	-	-	-	-	%
	Std. 6	-	11	8	29	%
	Std. 8	6	16	4	58	%
Trueness	Std. 4	-	-	-	-	%
	Std. 6		56	162	1.1	%
	Std. 8	4	48	254	1.0	%

Table 14: Figures of Merit for three measurement days for caffeine and testosterone via UPLC-HTUSN-cone B-TPI-MS.

Caffeine						
	Day 1	Day 2	Day 3	Average	Std. dev.	RSD (%)
iLOD (µg L^{-1})	11	20	28	20	9	43
iLOQ (µg L^{-1})	41	30	95	55	35	63
R^2 ((areal units per µg/ L)^2)	0.9909	0.9968	0.9979	0.995	0.00376	0.4
Sensitivity (µg/ L per areal units)	1.20E-04	1.46E-04	1.50E-04	1.39E-04	1.64E-05	12

		Inter-day			Intra-day	
Precision	Std. 4	1.4	14	8.8	22	%
	Std. 6	1.3	15	10	14	%
	Std. 8	2.6	15	4.8	16	%
Trueness	Std. 4	86	26	25	0.5	%
	Std. 6	20	-5.7	1.3	0.1	%
	Std. 8	-10	23	16	0.1	%

Testosterone						
	Day 1	Day 2	Day 3	Average	Std. dev.	RSD (%)
iLOD (µg L^{-1})	18	11	24	18	7	37
iLOQ (µg L^{-1})	53	130	74	86	40	46
R^2 ((areal units per µg/ L)^2)	0.9963	0.9975	0.9965	0.997	0.00064	0.1
Sensitivity (µg/ L per areal units)	3.90E-04	3.05E-04	1.71E-04	2.89E-04	1.10E-04	38

		Inter-day			Intra-day	
Precision	Std. 4	10	68	25	37	%
	Std. 6	21	17	20	24	%
	Std. 8	26	4.9	7.2	13	%
Trueness	Std. 4	60	-1.0	20	0.3	%
	Std. 6	88	31	43	0.5	%
	Std. 8	135	141	139	1.4	%

Table 15: Figures of Merit for three measurement days for caffeine and testosterone via UPLC-APCI nebulizer-iLTP-MS.

Caffeine						
	Day 1	Day 2	Day 3	Average	Std. dev.	RSD (%)
iLOD (µg L^{-1})	1.55	1.55	1.5	1.53	0.03	1.9
iLOQ (µg L^{-1})	8.62	5.77	4.78	6.39	1.99	31
R^2 ((areal units per µg/ L)^2)	0.9936	0.9979	0.996	0.996	0.00215	0.2
Sensitivity (µg/ L per areal units)	7.59E+03	6.47E+03	7.15E+03	7.07E+03	5.61E+02	7.9

		Inter-day			Intra-day	
Precision	Std. 4	7.1	2.7	15.7	16	%
	Std. 6	12.0	6.6	7.3	8.0	%
	Std. 8	3.5	5.8	2.7	4.0	%
Trueness	Std. 4	7.1	-9.1	-21.5	-0.08	%
	Std. 6	-11.5	-14.5	-16.1	-0.14	%
	Std. 8	3.2	1.2	3.5	0.03	%

Testosterone						
	Day 1	Day 2	Day 3	Average	Std. dev.	RSD (%)
iLOD (µg L^{-1})	4.09	0.76	1.13	2.0	1.83	92
iLOQ (µg L^{-1})	16.3	5.37	3.99	8.6	6.74	79
R^2 ((areal units per µg/ L)^2)	0.987	0.9863	0.9331	0.969	0.03092	3.2
Sensitivity (µg/ L per areal units)	1.19E+03	1.40E+03	3.31E+03	1.97E+03	1.17E+03	59

		Inter-day			Intra-day	
Precision	Std. 4	33.1	93.7	47.2	54	%
	Std. 6	24.5	93.0	41.3	66	%
	Std. 8	-	-	-	-	%
Trueness	Std. 4	99.0	26.0	31.1	0.5	%
	Std. 6	209.9	15.4	15.9	0.8	%
	Std. 8	-	-	-	-	%

Table 16: Figures of Merit for three measurement days for caffeine and testosterone via UPLC-APCI nebulizer-TPI-MS.

Caffeine						
	Day 1	Day 2	Day 3	Average	Std. dev.	RSD (%)
iLOD (µg L^{-1})	1.45	1.05	1.13	1.2	0.2	17
iLOQ (µg L^{-1})	6.38	3.9	4.73	5.0	1.3	25
R^2 ((areal units per µg/ L)^2)	0.9981	0.9945	0.9987	0.997	0.00227	0.2
Sensitivity (µg/ L per areal units)	6.59E+03	9.88E+03	1.03E+04	8.92E+03	2.03E+03	23

		Inter-day			Intra-day	
Precision	Std. 4	3.0	23.1	16.0	21.5	%
	Std. 6	6.5	13.7	6.5	8.6	%
	Std. 8	1.9	7.6	4.7	5.9	%
Trueness	Std. 4	-7.6	-28.7	6.1	-0.10	%
	Std. 6	-15.9	-18.6	-12.9	-0.16	%
	Std. 8	2.0	7.3	-1.1	0.03	%

Testosterone						
	Day 1	Day 2	Day 3	Average	Std. dev.	RSD (%)
iLOD (µg L^{-1})	1.18	1.18	1.73	1.4	0	23
iLOQ (µg L^{-1})	5.12	3.58	4.09	4.3	1	18
R^2 ((areal units per µg/ L)^2)	0.9991	0.9983	0.9905	0.996	0.00475	0.5
Sensitivity (µg/ L per areal units)	2.15E+03	4.13E+03	5.11E+03	3.80E+03	1.51E+03	40

		Inter-day			Intra-day	
Precision	Std. 4	49.2	37.9	12.7	42.3	%
	Std. 6	60.3	21.7	26.9	36.5	%
	Std. 8	-	-	-	-	%
Trueness	Std. 4	31.9	12.8	-21.3	0.08	%
	Std. 6	7.5	8.5	-8.0	0.03	%
	Std. 8	-	-	-	-	%

Table 17: Figures of Merit for three measurement days for caffeine and testosterone via UPLC-ESI-MS.

Caffeine						
	Day 1	Day 2	Day 3	Average	Std. dev.	RSD (%)
iLOD (µg L^{-1})	1.8	0.17	0.27	0.75	0.91	122.4
iLOQ (µg L^{-1})	6.25	0.58	0.89	2.57	3.19	124
R^2 ((areal units per µg/ L)^2)	0.9816	0.9978	0.9987	0.993	0.00962	1.0
Sensitivity (µg/ L per areal units)	8.13E-06	8.72E-06	6.68E-06	7.84E-06	1.05E-06	13.3

		Inter-day			Intra-day	
Precision	Std. 4	16.7	15.4	15.3	19	%
	Std. 6	5.9	15.0	24.3	15.9	%
	Std. 8	-	10.3	9.9	9.2	%
Trueness	Std. 4	-2.2	-24.7	-1.5	-0.09	%
	Std. 6	-2.9	-17.4	-11.5	-0.11	%
	Std. 8	-	-0.3	3.0	0.01	%

Testosterone						
	Day 1	Day 2	Day 3	Average	Std. dev.	RSD (%)
iLOD (µg L^{-1})	2.14	0.07	0.27	0.83	1.14	138
iLOQ (µg L^{-1})	7.14	0.29	0.9	2.78	3.79	137
R^2 ((areal units per µg/ L)^2)	0.9528	0.9924	0.9894	0.978	0.02205	2.3
Sensitivity (µg/ L per areal units)	9.37E-06	1.30E-05	1.02E-05	1.09E-05	1.88E-06	17

		Inter-day			Intra-day	
Precision	Std. 4	42.1	41.3	46.9	44	%
	Std. 6	22.4	43.9	63.4	42	%
	Std. 8	-	-	-	-	%
Trueness	Std. 4	33.7	2.5	67.0	0.3	%
	Std. 6	15.7	-23.8	-14.9	-0.1	%
	Std. 8	-	-	-	-	%

10.2 Electrospray ionization

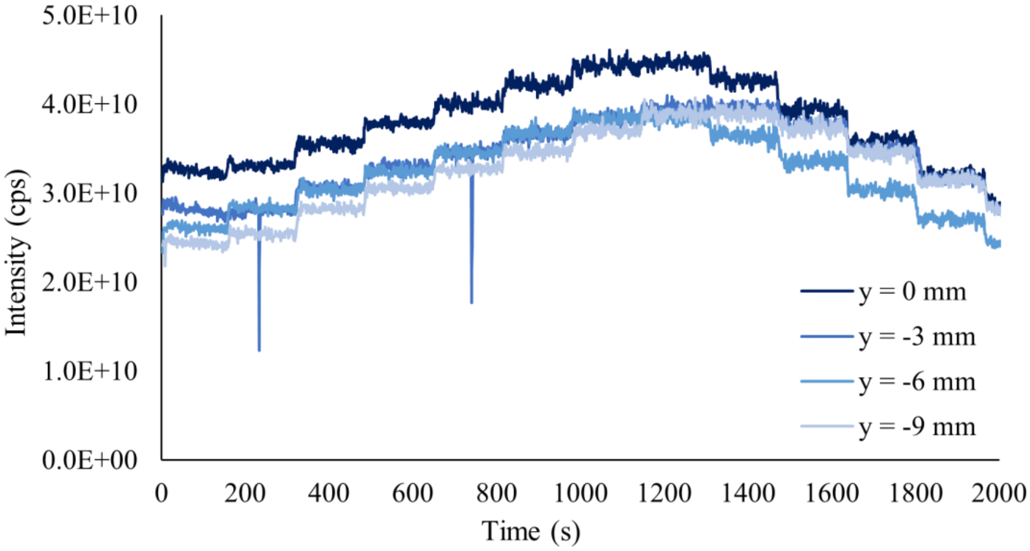

Figure 83: Total ion chronogram for a measurement with repeller 1 at a position of x = centered, z = +4 mm, and different y-positions.

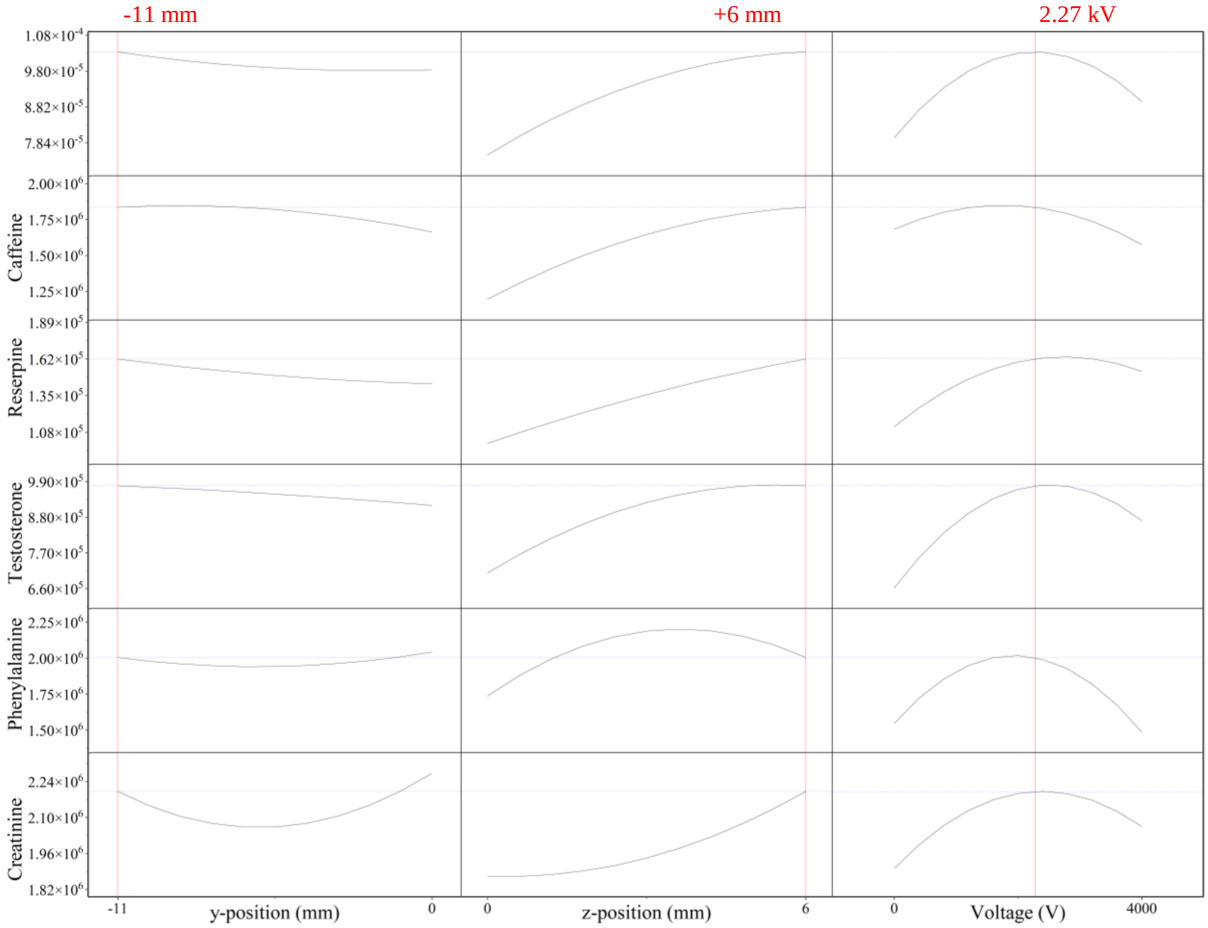

Figure 84: Curves of fit displaying the response of the peak areas of all averaged analytes (top) and then in order for caffeine, reserpine, testosterone, phenylalanine, and creatinine to the parameters y-position, z-position, and voltage. The optimal, average response is marked in red. The dependence on x-position is not displayed.

Table 18: Peak areas of caffeine (not spiked), 30 µg L^{-1} reserpine, and 10 µg L^{-1} testosterone in standard and plasma with and without repeller.

	Run 01	**Run 02**	**Run 03**	**Run 04**	**Run 05**	**Avg.**	**Std. dev.**	**RSD (%)**
Caffeine (not spiked)								
Plasma – with repeller	2.7E+07	2.7E+07	2.8E+07	2.8E+07	3.0E+07	2.8E+07	1.3E+06	4.6
Plasma – without repeller	2.4E+07	2.4E+07	2.5E+07	2.5E+07	2.6E+07	2.5E+07	1.1E+06	4.6
Reserpine								
Standard – with repeller	4.6E+05	3.9E+05	3.4E+05	2.7E+05	1.6E+05	3.2E+05	1.2E+05	35.8
Standard – without repeller	4.4E+05	2.2E+05	2.0E+05	1.6E+05	1.0E+05	2.3E+05	1.3E+05	56.5
Plasma – with repeller	9.7E+05	7.5E+05	4.2E+05	3.8E+05	3.9E+05	5.8E+05	2.7E+05	46.0
Plasma – without repeller	6.9E+05	3.3E+05	1.7E+05	1.6E+05	1.7E+05	3.1E+05	2.3E+05	73.6
Testosterone								
Standard – with repeller	6.1E+05	5.0E+05	5.2E+05	5.2E+05	5.3E+05	5.4E+05	4.2E+04	7.9
Standard – without repeller	9.5E+05	5.3E+05	5.4E+05	5.5E+05	5.7E+05	6.3E+05	1.8E+05	28.8
Plasma – with repeller	1.0E+06	7.3E+05	3.4E+05	3.0E+05	3.1E+05	5.4E+05	3.1E+05	58.7
Plasma – without repeller	1.0E+06	4.8E+05	1.8E+05	1.5E+05	1.6E+05	4.0E+05	3.7E+05	93.6

Table 19: Average peak height intensities for the measured analytes with the APCI nebulizer and for different repellers and repeller distances at their respective optimal voltage. The best signal intensity for each analyte is marked in a brighter color. When the peak was too low to be properly distinguished from the background spectrum, it is marked in grey.

	APCI needle			**Repeller 1**		
				Position A	**Position B**	**Position C**
	3 kV	3.5 kV	4 kV	0.2 kV	0.3 kV	0.4 kV
Caffeine	6.6E+06	6.1E+06	5.8E+06			
Reserpine	1.6E+06	1.5E+06	1.2E+06	4.7E+05	7.1E+05	6.0E+05
Testosterone	5.0E+06	4.6E+06	4.3E+06	9.8E+04	1.1E+05	8.7E+04
Phenylalanine	4.7E+06	4.5E+06	4.2E+06			

	Repeller 2 upwards			**Repeller 2 downwards**	**Repeller 4**		
	Position A	**Position B**	**Position C**	**Position A**	**Position A**	**Position B**	**Position C**
	0.25 kV	0.3 kV	0.4 kV	0.25 kV	0.25 kV	0.45 kV	0.7 kV
Caffeine		8.6E+04	1.4E+05		1.2E+05		
Reserpine	5.5E+05	3.5E+05	3.5E+05	3.8E+05	5.7E+05	4.3E+05	5.5E+05
Testosterone	1.6E+05	2.1E+05	2.2E+05		2.4E+05	1.5E+05	1.2E+05
Phenylalanine		1.4E+05	2.0E+05		2.1E+05	8.0E+04	3.4E+04

	Repeller 5			**Repeller 6**		
	Position A	**Position B**	**Position C**	**Position A**	**Position B**	**Position C**
	0.25 kV	0.4 kV	0.5 kV	0.7 kV	0.8 kV	1.1 kV
Caffeine	1.2E+05		1.4E+05			
Reserpine	4.9E+05	5.8E+05	3.9E+05	6.9E+05	6.0E+05	4.8E+05
Testosterone	2.2E+05	2.5E+05	2.7E+05	1.3E+05	1.3E+05	1.9E+05
Phenylalanine	1.9E+05	1.3E+05	2.4E+05			

Table 20: Signal intensities for the peaks obtained with APCI nebulizer and the different repellers divided by those obtained with the APCI needle at 3.5 kV.

	Repeller 1			**Repeller 2 upwards**			**Repeller 2 downwards**
	Position A	**Position B**	**Position C**	**Position A**	**Position B**	**Position C**	**Position A**
	0.2 kV	0.3 kV	0.4 kV	0.25 kV	0.3 kV	0.4 kV	0.25 kV
Caffeine					0.01	0.02	
Reserpine	0.29	0.43	0.36	0.34	0.21	0.21	0.24
Testosterone	0.02	0.02	0.02	0.03	0.04	0.04	
Phenylalanine					0.03	0.04	

	Repeller 4			**Repeller 5**		
	Position A	**Position B**	**Position C**	**Position A**	**Position B**	**Position C**
	0.25 kV	0.45 kV	0.7 kV	0.25 kV	0.4 kV	0.5 kV
Caffeine	0.02			0.02		0.02
Reserpine	0.35	0.26	0.34	0.30	0.36	0.24
Testosterone	0.05	0.03	0.02	0.04	0.05	0.05
Phenylalanine	0.04	0.02	0.01	0.04	0.03	0.05

	Repeller 6		
	Position A	**Position B**	**Position C**
	0.7 kV	0.8 kV	1.1 kV
Caffeine			
Reserpine	0.42	0.37	0.30
Testosterone	0.03	0.03	0.04
Phenylalanine			

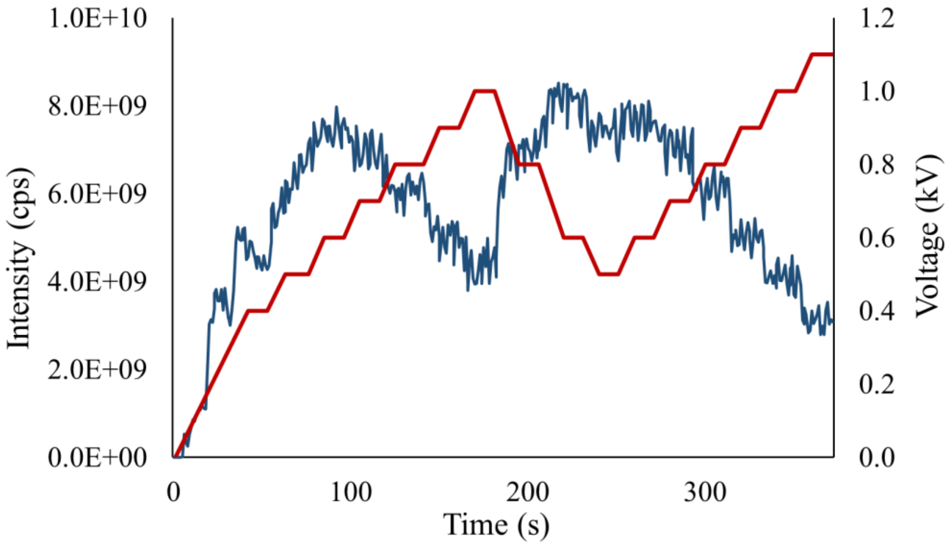

Figure 85: TIC chronogram for 200 µL min^{-1} test solution via continuous injection with the ESI without voltage and with repeller 6.

Table 21: Signal intensities for the peaks obtained with the ESI without voltage but with the different repellers (top) as well as those results divided by signal intensities obtained with the ESI needle at 4 kV (bottom).

	ESI 4.0 kV	**Repeller 1** 1.9 kV	**Repeller 2** 3.0 kV	**Repeller 4** 0.5 kV	**Repeller 5** 2.8 kV	**Repeller 6** 0.6 kV	**Repeller 7** 2.9 kV
Caffeine	8.5E+06	3.3E+05	3.4E+05	4.9E+05	2.1E+05	3.5E+05	5.0E+05
Reserpine	1.9E+07	1.9E+06	1.9E+06	5.9E+05	1.1E+06	3.6E+05	2.8E+06
Testosterone	1.4E+07	9.0E+05	8.2E+05	7.0E+05	5.8E+05	6.0E+05	1.2E+06
Phenylalanine	7.7E+07	3.6E+06	2.7E+06	2.1E+06	6.4E+05	1.7E+06	4.8E+06
Creatinine	5.2E+06	1.0E+06	1.1E+06	1.1E+06	8.7E+05	7.9E+05	2.0E+06

	Repeller 1	**Repeller 2**	**Repeller 4**	**Repeller 5**	**Repeller 6**	**Repeller 7**
Caffeine	0.04	0.04	0.06	0.03	0.04	0.06
Reserpine	0.10	0.10	0.03	0.05	0.02	0.15
Testosterone	0.06	0.06	0.05	0.04	0.04	0.09
Phenylalanine	0.05	0.04	0.03	0.01	0.02	0.06
Creatinine	0.20	0.22	0.21	0.17	0.15	0.38

10.3 nanoESI-iLTP coupling

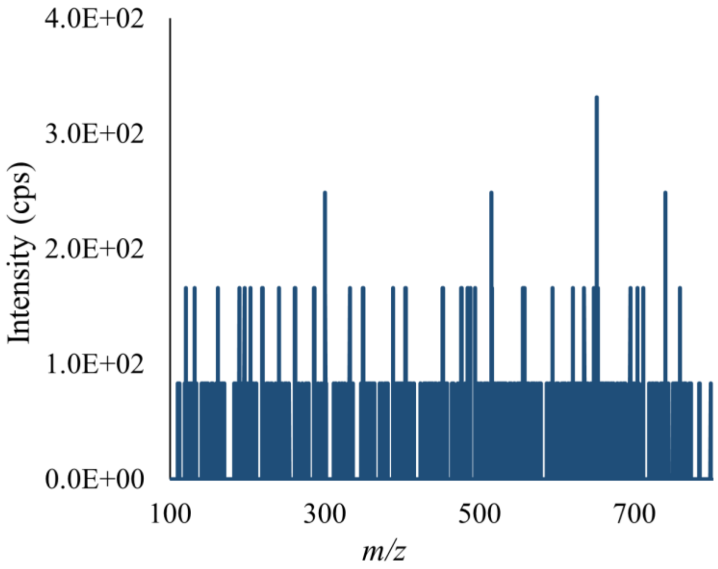

Figure 86: Signal in the mass spectrometer provoked most probably by electric short circuits between the FµTP ion source and the MS inlet. Mass spectrum averaged over 1.5 min. Plasma voltage 1.4 kV (2.6 mA), nanoESI voltage turned off.

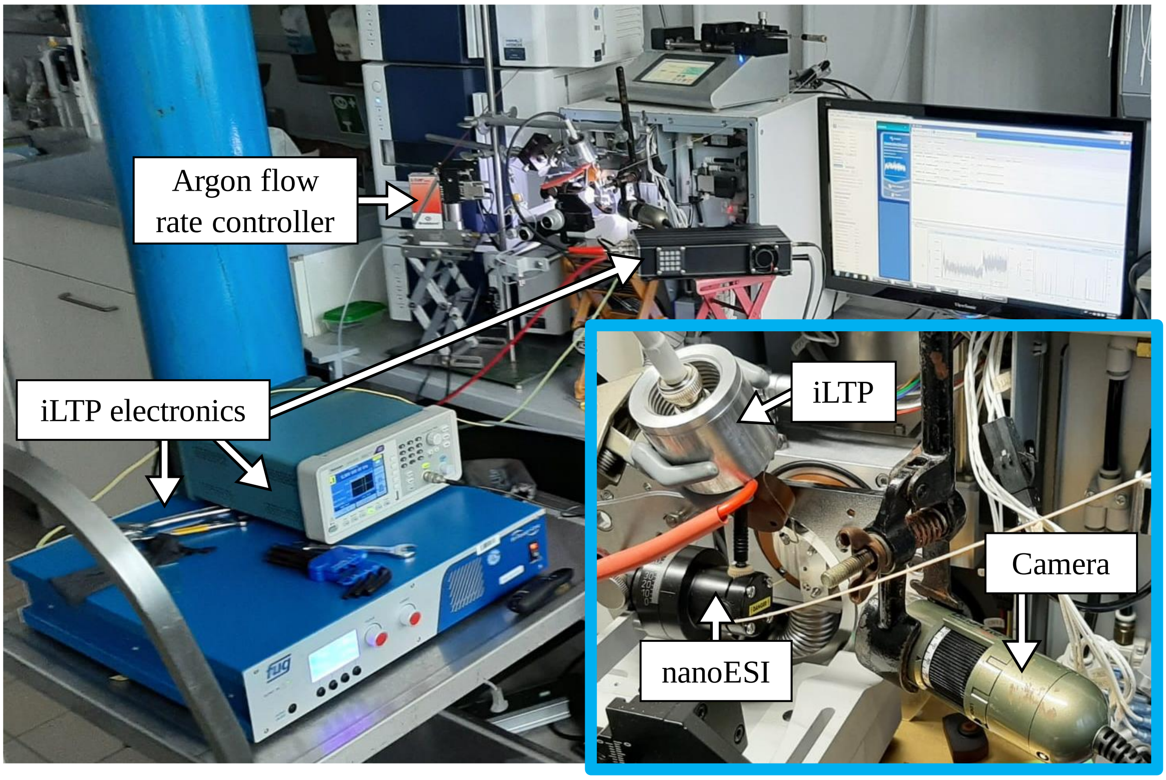

Figure 87: Complete experimental set-up of the ambient nanoESI-iLTP dual ion source.

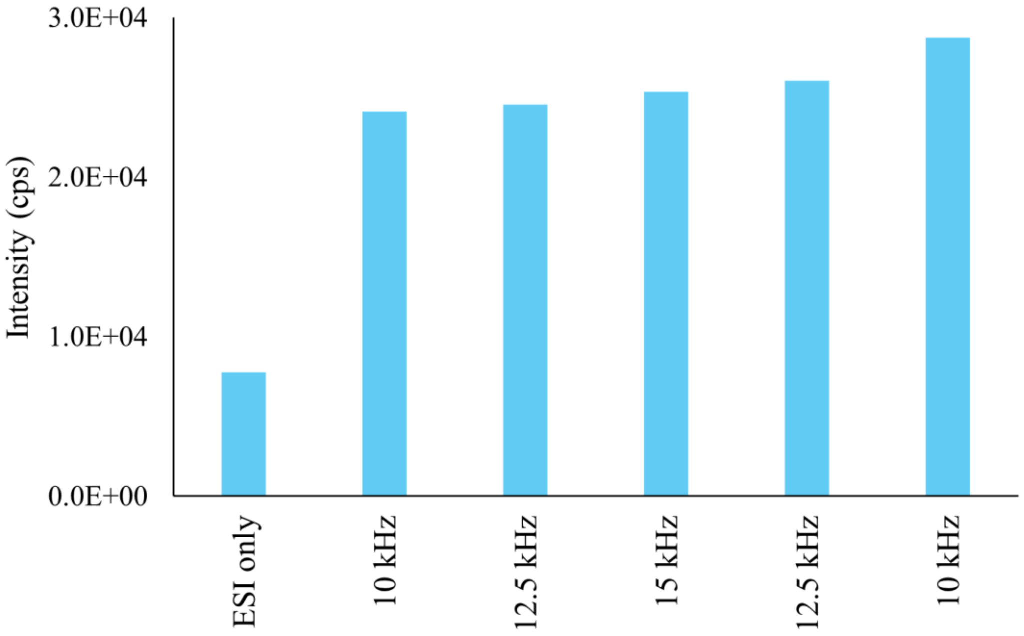

Figure 88: Reserpine peak height in averaged mass spectra. During the measurement, the ESI ionization potential was at 1.7 kV and the nanoESI positioned at x = 7 mm, y = 0 mm, z = 9 mm, angle = 14°. The plasma was operated with a pulse width of 50 µs, argon flow rate of 80 mL min^{-1}, and 1.3 kV. The frequency was increased every 20 min and eventually decreased while the analyte signal steadily increased.

Table 22: Reserpine peak heights in averaged mass spectra for different plasma conditions. The values for the ESI + iLTP measurement was divided by the first ESI measurement and 12.5 kHz and 50 µs showed the biggest relative increase in signal response.

	12.5 kHz			15 kHz	10 kHz
	2 µs	50 µs	70 µs	50 µs	
ESI only	1.40E+04	1.09E+04	1.56E+04	1.70E+04	1.16E+04
Plasma	2.88E+03	2.04E+04	2.30E+04	1.94E+04	1.68E+04
ESI only	1.23E+04	1.15E+04	1.32E+04	1.22E+04	1.23E+04
ESI + iLTP divided by first ESI	0.21	1.87	1.47	1.14	1.45

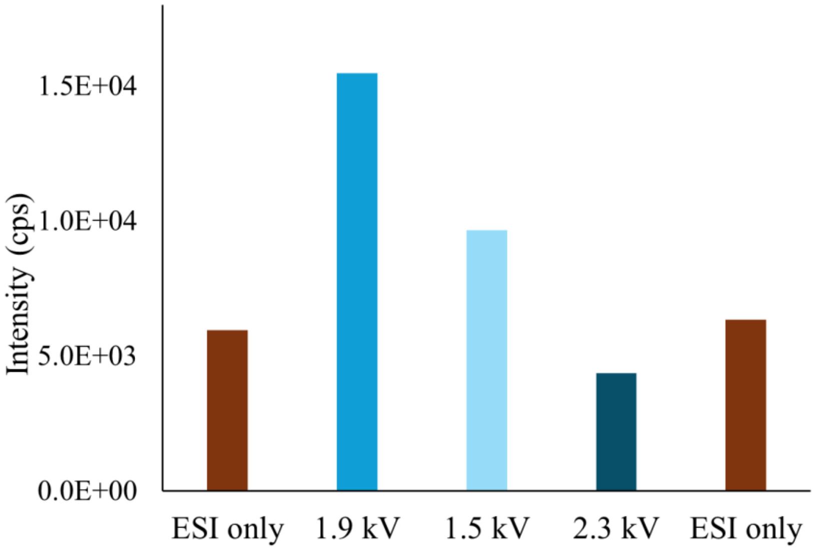

Figure 89: Checking the influence of plasma voltage. The order of 1.9 kV to 1.5 kV to 2.3 kV served to avoid possible charging effects. These results show the same trend as those of the previous measuring day. The ESI ionization potential was at 1.8 kV and the nanoESI positioned at x = 7 mm, y = 0.5 mm, z = 11 mm, angle = 14°. The plasma was operated with a frequency of 12.5 kHz, pulse width of 50 µs, and argon flow rate of 80 mL min^{-1}.

Table 23: Reserpine peak heights in averaged mass spectra for different argon flow rates. The values for the ESI + iLTP measurement was divided by the first ESI measurements with and without argon flow rate and 80 mL min^{-1} showed the biggest relative increase in signal response.

		Argon gas flow rate (mL min^{-1})				
		40	60	80	100	120
only ESI	Argon gas off	1.40E+03	2.73E+03	3.06E+03	2.89E+03	2.10E+03
only ESI	Argon gas on	1.24E+03	2.81E+03	3.39E+03	2.40E+03	2.14E+03
ESI + iLTP	(Argon on)	6.12E+03	7.66E+03	9.52E+03	7.13E+03	5.47E+03
only ESI	Argon gas on	2.69E+03	2.29E+03	3.36E+03	2.20E+03	1.73E+03
only ESI	Argon gas off	2.56E+03	2.18E+03	3.66E+03	2.31E+03	1.86E+03
Plasma / ESI without argon		4.4	2.8	3.1	2.5	2.6
Plasma / ESI with argon		4.9	2.7	2.8	3.0	2.6

11. References

1. Pape A., Schmitz O.J. Dielectric barrier discharge in mass spectrometry – An overview over plasma investigations and ion sources applications. Trends Analyt Chem. 2024;170.
2. Abian J. The coupling of gas and liquid chromatography with mass spectrometry †. J Mass Spectrom. 1999;34(3):157-168.
3. Arrizabalaga-Larrañaga A., Ayala-Cabrera J.F., Seró R., Santos J.F., Moyano E. Chapter 9 - Ambient ionization mass spectrometry in food analysis. In: Galanakis CM, editor. Food Toxicology and Forensics: Academic Press; 2021. p. 271-312.
4. Richter W.J., Schwarz H. Chemical ionization - A Mass-Spectrometric Analytical Procedure of Rapidly Increasing Importance. Angew Chem Int Ed Engl. 1978;17(6):13.
5. Venter A.R., Douglass K.A., Shelley J.T., Hasman G., Honarvar E. Mechanisms of Real-Time, Proximal Sample Processing during Ambient Ionization Mass Spectrometry. Anal Chem. 2014;86(1):233-249.
6. Shelley J.T., Badal S.P., Engelhard C., Hayen H. Ambient desorption/ionization mass spectrometry: evolution from rapid qualitative screening to accurate quantification tool. Anal Bioanal Chem. 2018;410(17):4061-4076.
7. Yamashita M., Fenn J.B. Electrospray ion source. Another variation on the free-jet theme. J Phys Chem. 1984;88(20):4451-4459.
8. Takáts Z., Wiseman J.M., Gologan B., Cooks R.G. Mass Spectrometry Sampling Under Ambient Conditions with Desorption Electrospray Ionization. Sci. 2004;306(5695):471-473.
9. Whitehouse C.M., Dreyer R.N., Yamashita M., Fenn J.B. Electrospray interface for liquid chromatographs and mass spectrometers. Anal Chem. 1985;57(3):675-679.
10. Horning E.C., Carroll D.I., Dzidic I., Haegele K.D., Horning M.G., Stillwell R.N. Liquid chromatograph—mass spectrometer—computer analytical systems: A continuous-flow system based on atmospheric pressure ionization mass spectrometry. J Chromatogr A. 1974;99:13-21.
11. Horning E.C., Carroll D.I., Dzidic I., Haegele K.D., Horning M.G., Stillwell R.N. Atmospheric Pressure Ionization (API) Mass Spectrometry. Solvent-Mediated Ionization of Samples Introduced in Solution and in a Liquid Chromatograph Effluent Stream. J Chromatogr Sci. 1974;12(11):725-729.
12. Carroll D.I., Dzidic I., Stillwell R.N., Haegele K.D., Horning E.C. Atmospheric pressure ionization mass spectrometry. Corona discharge ion source for use in a liquid chromatograph-mass spectrometer-computer analytical system. Anal Chem. 1975;47(14):2369-2373.
13. Lara-Ortega F.J., Robles-Molina J., Brandt S., Schütz A., Gilbert-López B., Molina-Díaz A., et al. Use of dielectric barrier discharge ionization to minimize matrix effects and expand coverage in pesticide residue analysis by liquid chromatography-mass spectrometry. Anal Chim Acta. 2018;1020:76-85.
14. Albert A., Engelhard C. Characteristics of Low-Temperature Plasma Ionization for Ambient Mass Spectrometry Compared to Electrospray Ionization and Atmospheric Pressure Chemical Ionization. Anal Chem. 2012;84(24):10657-10664.
15. Syage J.A., Evans M.D. Photoionization Mass Spectrometry: A Powerful New Tool for Drug Discovery-This article describes the benefits that photoionization MS has over existing methods for performing high-speed. Spectrosc. 2001;16(11):14-21.
16. Constapel M., Schellenträger M., Schmitz O.J., Gäb S., Brockmann K.J., Giese R., et al. Atmospheric-pressure laser ionization: a novel ionization method for liquid chromatography/mass spectrometry. Rapid Commun Mass Spectrom. 2005;19(3):326-336.
17. Javanshad R., Venter A.R. Ambient ionization mass spectrometry: real-time, proximal sample processing and ionization. Analytical Methods. 2017;9(34):4896-4907.

18. Zhao Z., Li D., Wang B., Ding X., Dai J., Yuan X., et al. A systematic study of the distinctive character of microwave induced plasma desorption/ionization (MIPDI) mass spectrometry: Is it a soft or a hard ion source? Int J Mass Spectrom. 2015;376:65-74.
19. Yin J., Zhao Z., Zhan X., Duan Y. Exploration and performance evaluation of microwave-induced plasma with different discharge gases for ambient desorption/ionization mass spectrometry. Rapid Commun Mass Spectrom. 2017;31(11):919-927.
20. Cody R.B., Laramée J.A., Durst H.D. Versatile New Ion Source for the Analysis of Materials in Open Air under Ambient Conditions. Anal Chem. 2005;77(8):2297-2302.
21. Ratcliffe L.V., Rutten F.J.M., Barrett D.A., Whitmore T., Seymour D., Greenwood C., et al. Surface Analysis under Ambient Conditions Using Plasma-Assisted Desorption/Ionization Mass Spectrometry. Anal Chem. 2007;79:6094-6101.
22. Andrade F.J., Shelley J.T., Wetzel W.C., Webb M.R., Gamez G., Ray S.J., et al. Atmospheric Pressure Chemical Ionization Source. 1. Ionization of Compounds in the Gas Phase. Anal Chem. 2008;80(8):2646-2653.
23. Harper J.D., Charipar N.A., Mulligan C.C., Zhang X., Cooks R.G., Ouyang Z. Low-Temperature Plasma Probe for Ambient Desorption Ionization. Anal Chem. 2008;80(23):9097-9104.
24. Brandt S., Klute F.D., Schutz A., Marggraf U., Drees C., Vogel P., et al. Flexible Microtube Plasma (FmuTP) as an Embedded Ionization Source for a Microchip Mass Spectrometer Interface. Anal Chem. 2018;90(17):10111-10116.
25. Na N., Zhao M., Zhang S., Yang C., Zhang X. Development of a dielectric barrier discharge ion source for ambient mass spectrometry. J Am Soc Mass Spectrom. 2007;18(10):1859-1862.
26. Ayala-Cabrera J.F., Turkowski J., Uteschil F., Schmitz O.J. Development of a Tube Plasma Ion Source for Gas Chromatography-Mass Spectrometry Analysis and Comparison with Other Atmospheric Pressure Ionization Techniques. Anal Chem. 2022;94(27):9595-9602.
27. Bregy L., Sinues P.M., Nudnova M.M., Zenobi R. Real-time breath analysis with active capillary plasma ionization-ambient mass spectrometry. J Breath Res. 2014;8(2):027102.
28. Siemens W. Ueber die elektrostatische Induction und die Verzögerung des Stroms in Flaschendrähten. Ann d Phys. 1857;178(9):66-122.
29. Kogelschatz U., Eliasson B., Egli W. From ozone generators to flat television screens: history and future potential of dielectric-barrier discharges. Pure Applied Chemistry. 1999;71(10):1819-1828.
30. Eliasson B., Kogelschatz U. Modeling and applications of silent discharge plasmas. IEEE Trans PLasma Sci. 1991;19(2):309-323.
31. Kogelschatz U., Eliasson B., Egli W. Dielectric-Barrier Discharges. Principle and Applications. Journal de physique IV France. 1997;07(C4):C4-47-C44-66.
32. Kogelschatz U. Dielectric-Barrier Discharges: Their History, Discharge Physics, and Industrial Applications. Plasma Chem Plasma Process. 2003;23(1):1-46.
33. Na N., Zhang C., Zhao M., Zhang S., Yang C., Fang X., et al. Direct detection of explosives on solid surfaces by mass spectrometry with an ambient ion source based on dielectric barrier discharge. J Mass Spectrom. 2007;42(8):1079-1085.
34. Klute F.D., Brandt S., Vogel P., Biskup B., Reininger C., Horvatic V., et al. Systematic Comparison between Half and Full Dielectric Barrier Discharges Based on the Low Temperature Plasma Probe (LTP) and Dielectric Barrier Discharge for Soft Ionization (DBDI) Configurations. Anal Chem. 2017;89(17):9368-9374.
35. Brecht D., Uteschil F., Schmitz O.J. Development of an inverse low-temperature plasma ionization source for liquid chromatography/mass spectrometry. Rapid Commun Mass Spectrom. 2021;35(10):e9071.

36. Albert A., Engelhard C. Chemometric optimization of a low-temperature plasma source design for ambient desorption/ionization mass spectrometry. Spectrochim Acta Part B At Spectrosc. 2015;105:109-115.

37. Hu J., Li W., Zheng C., Hou X. Dielectric Barrier Discharge in Analytical Spectrometry. Appl Spectrosc Rev. 2011;46(5):368-387.

38. Carbone E.A., Schregel C.-G., Czarnetzki U. Ignition and afterglow dynamics of a high pressure nanosecond pulsed helium micro-discharge: II. Rydberg molecules kinetics. Plasma Sources Sci Technol. 2016;25(5):054004.

39. Kratzer J., Mester Z., Sturgeon R.E. Comparison of dielectric barrier discharge, atmospheric pressure radiofrequency-driven glow discharge and direct analysis in real time sources for ambient mass spectrometry of acetaminophen. Spectrochim Acta Part B At Spectrosc. 2011;66(8):594-603.

40. Chan G.C.-Y., Shelley J.T., Wiley J.S., Engelhard C., Jackson A.U., Cooks R.G., et al. Elucidation of reaction mechanisms responsible for afterglow and reagent-ion formation in the low-temperature plasma probe ambient ionization source. Anal Chem. 2011;83(10):3675-3686.

41. Reininger C., Woodfield K., Keelor J.D., Kaylor A., Fernández F.M., Farnsworth P.B. Absolute number densities of helium metastable atoms determined by atomic absorption spectroscopy in helium plasma-based discharges used as ambient desorption/ionization sources for mass spectrometry. Spectrochim Acta Part B At Spectrosc. 2014;100:98-104.

42. Schütz A., Lara-Ortega F.J., Klute F.D., Brandt S., Schilling M., Michels A., et al. Soft Argon-Propane Dielectric Barrier Discharge Ionization. Anal Chem. 2018;90(5):3537-3542.

43. Bruggeman P.J., Kushner M.J., Locke B.R., Gardeniers J.G.E., Graham W.G., Graves D.B., et al. Plasma–liquid interactions: a review and roadmap. Plasma Sources Sci Technol. 2016;25(5).

44. Bruggeman P., Brandenburg R. Atmospheric pressure discharge filaments and microplasmas: physics, chemistry and diagnostics. Journal of Physics D: Applied Physics. 2013;46(46).

45. Brandt S., Klute F.D., Schutz A., Franzke J. Dielectric barrier discharges applied for soft ionization and their mechanism. Anal Chim Acta. 2017;951:16-31.

46. Karanassios V. Microplasmas for chemical analysis: analytical tools or research toys? Spectrochim Acta Part B At Spectrosc. 2004;59(7):909-928.

47. Huang M.Z., Yuan C.H., Cheng S.C., Cho Y.T., Shiea J. Ambient ionization mass spectrometry. Annu Rev Anal Chem (Palo Alto Calif). 2010;3:43-65.

48. Harris G.A., Nyadong L., Fernandez F.M. Recent developments in ambient ionization techniques for analytical mass spectrometry. Analyst. 2008;133(10):1297-1301.

49. Tendero C., Tixier C., Tristant P., Desmaison J., Leprince P. Atmospheric pressure plasmas: A review. Spectrochim Acta Part B At Spectrosc. 2006;61(1):2-30.

50. Reuter S., von Woedtke T., Weltmann K.-D. The kINPen—a review on physics and chemistry of the atmospheric pressure plasma jet and its applications. J Phys D Appl Phys. 2018;51:233001.

51. Beneito-Cambra M., Gilbert-López B., Moreno-González D., Bouza M., Franzke J., García-Reyes J.F., et al. Ambient (desorption/ionization) mass spectrometry methods for pesticide testing in food: a review. Analytical methods. 2020;12(40):pp. 4831-4852.

52. Martínez-Jarquín S., Winkler R. Low-temperature plasma (LTP) jets for mass spectrometry (MS): Ion processes, instrumental set-ups, and application examples. Trends Analyt Chem. 2017;89:133-145.

53. Chen J., Tang F., Guo C.a., Zhang S., Zhang X. Plasma-based ambient mass spectrometry: a step forward to practical applications. Analytical Methods. 2017;9(34):4908-4923.

54. Kauppila T.J., Kostiainen R. Ambient mass spectrometry in the analysis of compounds of low polarity. Analytical Methods. 2017;9(34):4936-4953.

55. Meyer C., Muller S., Gurevich E.L., Franzke J. Dielectric barrier discharges in analytical chemistry. Analyst. 2011;136(12):2427-2440.
56. Niu G., Knodel A., Burhenn S., Brandt S., Franzke J. Review: Miniature dielectric barrier discharge (DBD) in analytical atomic spectrometry. Anal Chim Acta. 2021;1147:211-239.
57. Brecht D. Entwicklung von Atmosphärendruck-Ionenquellen für die Massenspektrometrie. Essen: University Duisburg-Essen; 2020.
58. Hung J.-H. Low-Temperature Plasma Ionization Mass Spectrometry Combined with Thermal Analysis for Polymer Characterization [Ph.D. thesis]. Sizihwan: National Sun Yat-sen University; 2014.
59. Meisenbichler C. Neue Methoden der bildgebenden Massenspektrometrie [Ph.D. thesis]. Innsbruck: University Innsbruck; 2020.
60. Mirabelli M.F. Soft Ionization Mass Spectrometry: from Matrix-Assisted Laser Desorption/ Ionization to Dielectric Barrier Discharge Ionization and Atmospheric Pressure Photoionization. Zurich: ETH Zürich; 2018.
61. Schütz A. Eine schalt- und verstimmbare dielektrisch behinderte Entladung als weiche Ionisierungsquelle für die Analytik. Dortmund: Technical University Dortmund; 2018.
62. Alves Pereira G.M. Ionização Ambiente em Espectrometria de Massas: Construção de uma Fonte de Ionização LTP e Modificações na Técnica PS-MS. Belo Horizonte: Universidade Federal de Minas Gerais; 2020.
63. Löbbecke S. Analysis of phthalate esters in drinking water by GC-TPI-MS [Bachelor's thesis]. Essen: University Duisburg-Essen; 2022.
64. Michels A., Tombrink S., Vautz W., Miclea M., Franzke J. Spectroscopic characterization of a microplasma used as ionization source for ion mobility spectrometry. Spectrochim Acta Part B At Spectrosc. 2007;62(11):1208-1215.
65. Garcia-Reyes J.F., Mazzoti F., Harper J.D., Charipar N.A., Oradu S., Ouyang Z., et al. Direct olive oil analysis by low-temperature plasma (LTP) ambient ionization mass spectrometry. Rapid Commun Mass Spectrom. 2009;23(19):3057-3062.
66. Soparawalla S., Tadjimukhamedov F.K., Wiley J.S., Ouyang Z., Cooks R.G. In situ analysis of agrochemical residues on fruit using ambient ionization on a handheld mass spectrometer. Analyst. 2011;136(21):4392-4396.
67. Dalgleish J.K., Hou K., Ouyang Z., Cooks R.G. In Situ Explosive Detection Using a Miniature Plasma Ion Source and a Portable Mass Spectrometer. Anal Lett. 2012;45(11):1440-1446.
68. Kuhlmann C., Shelley J.T., Engelhard C. Plasma-Based Ambient Desorption/Ionization Mass Spectrometry for the Analysis of Liquid Crystals Employed in Display Devices. J Am Soc Mass Spectrom. 2019;30(10):2101-2113.
69. Shelley J.T., Wiley J.S., Chan G.C.Y., Schilling G.D., Ray S.J., Hieftje G.M. Characterization of direct-current atmospheric-pressure discharges useful for ambient desorption/ionization mass spectrometry. J Am Soc Mass Spectrom. 2009;20(5):837-844.
70. Andrade F.J., Wetzel W.C., Chan G.C.Y., Webb M.R., Gamez G., Ray S.J., et al. A new, versatile, direct-current helium atmospheric-pressure glow discharge. J Anal At Spectrom. 2006;21(11):1175-1184.
71. Shelley J.T., Hieftje G.M. Ionization matrix effects in plasma-based ambient mass spectrometry sources. J Anal At Spectrom. 2010;25(3).
72. Klute F.D., Brandt S., Franzke J. Spatiotemporal characterization of different dielectric barrier discharges designed for soft ionization. Spectrochim Acta Part B At Spectrosc. 2021;176:106037.
73. Klute F.D., Michels A., Schutz A., Vadla C., Horvatic V., Franzke J. Capillary Dielectric Barrier Discharge: Transition from Soft Ionization to Dissociative Plasma. Anal Chem. 2016;88(9):4701-4705.

74. Klute F.D., Schutz A., Michels A., Vadla C., Veza D., Horvatic V., et al. An experimental study on the influence of trace impurities on ionization of atmospheric noble gas dielectric barrier discharges. Analyst. 2016;141(20):5842-5848.
75. Schutz A., Klute F.D., Brandt S., Liedtke S., Jestel G., Franzke J. Tuning Soft Ionization Strength for Organic Mass Spectrometry. Anal Chem. 2016;88(10):5538-5541.
76. Meyer C., Müller S., Gilbert-Lopez B., Franzke J. Impact of homogeneous and filamentary discharge modes on the efficiency of dielectric barrier discharge ionization mass spectrometry. Anal Bioanal Chem. 2013;405(14):4729-4735.
77. Vogel P., Marggraf U., Brandt S., Garcia-Reyes J.F., Franzke J. Analyte-Tailored Controlled Atmosphere Improves Dielectric Barrier Discharge Ionization Mass Spectrometry Performance. Anal Chem. 2019;91(5):3733-3739.
78. Gilbert-Lopez B., Garcia-Reyes J.F., Meyer C., Michels A., Franzke J., Molina-Diaz A., et al. Simultaneous testing of multiclass organic contaminants in food and environment by liquid chromatography/dielectric barrier discharge ionization-mass spectrometry. Analyst. 2012;137(22):5403-5410.
79. Gilbert-Lopez B., Geltenpoth H., Meyer C., Michels A., Hayen H., Molina-Diaz A., et al. Performance of dielectric barrier discharge ionization mass spectrometry for pesticide testing: a comparison with atmospheric pressure chemical ionization and electrospray ionization. Rapid Commun Mass Spectrom. 2013;27(3):419-429.
80. Gilbert-Lopez B., Lara-Ortega F.J., Robles-Molina J., Brandt S., Schutz A., Moreno-Gonzalez D., et al. Detection of multiclass explosives and related compounds in soil and water by liquid chromatography-dielectric barrier discharge ionization-mass spectrometry. Anal Bioanal Chem. 2019;411(19):4785-4796.
81. Hagenhoff S., Hayen H. LC/MS analysis of vitamin D metabolites by dielectric barrier discharge ionization and a comparison with electrospray ionization and atmospheric pressure chemical ionization. Anal Bioanal Chem. 2018;410(20):4905-4911.
82. Hagenhoff S., Korf A., Markgraf U., Brandt S., Schütz A., Franzke J., et al. Screening of semifluorinated n-alkanes by gas chromatography coupled to dielectric barrier discharge ionization mass spectrometry. Rapid Commun Mass Spectrom. 2018;32:1092-1098.
83. Hayen H., Michels A., Franzke J. Dielectric barrier discharge ionization for liquid chromatography/mass spectrometry. Anal Chem. 2009;81(24):10239-10245.
84. Nudnova M.M., Zhu L., Zenobi R. Active capillary plasma source for ambient mass spectrometry. Rapid Commun Mass Spectrom. 2012;26(12):1447-1452.
85. Mirabelli M.F., Wolf J.C., Zenobi R. Atmospheric pressure soft ionization for gas chromatography with dielectric barrier discharge ionization-mass spectrometry (GC-DBDI-MS). Analyst. 2017;142(11):1909-1915.
86. Huba A.K., Mirabelli M.F., Zenobi R. Understanding and Optimizing the Ionization of Polycyclic Aromatic Hydrocarbons in Dielectric Barrier Discharge Sources. Anal Chem. 2019;91(16):10694-10701.
87. www.instrument.com. 华仪宁创 DBDI-100 介质阻挡放电离子源 2022 [Available from: https://www.instrument.com.cn/netshow/SH104136/C281620.htm.
88. Li B., Kong J., Yang L., Zhang L., Zhang Z., Li C. Direct detection of chemical warfare agent simulants in soil by thermal desorption-low temperature plasma-mass spectrometry. Int J Mass Spectrom. 2020;451.
89. Zhang Y., Xu S., Wen L., Bai Y., Niu L., Song D., et al. A dielectric barrier discharge ionization based interface for online coupling surface plasmon resonance with mass spectrometry. Analyst. 2016;141(11):3343-3348.
90. Zhang Y., Ai W., Bai Y., Zhou Y., Wen L., Zhang X., et al. An interface for online coupling capillary electrophoresis to dielectric barrier discharge ionization mass spectrometry. Anal Bioanal Chem. 2016;408(30):8655-8661.
91. GmbH P. Plasmion 2023 [Available from: https://plasmion.com/technology/.

92. Wiley J.S., Shelley J.T., Cooks R.G. Handheld low-temperature plasma probe for portable "point-and-shoot" ambient ionization mass spectrometry. Anal Chem. 2013;85(14):6545-6552.

93. Kiontke A., Holzer F., Belder D., Birkemeyer C. The requirements for low-temperature plasma ionization support miniaturization of the ion source. Anal Bioanal Chem. 2018;410(16):3715-3722.

94. Kumano S., Sugiyama M., Yamada M., Nishimura K., Hasegawa H., Morokuma H., et al. Development of a portable mass spectrometer characterized by discontinuous sample gas introduction, a low-pressure dielectric barrier discharge ionization source, and a vacuumed headspace technique. Anal Chem. 2013;85(10):5033-5039.

95. Meisenbichler C., Kluibenschedl F., Muller T. A 3-in-1 Hand-Held Ambient Mass Spectrometry Interface for Identification and 2D Localization of Chemicals on Surfaces. Anal Chem. 2020;92(21):14314-14318.

96. Dole M., Mack L.L., Hines R.L., Mobley R.C., Ferguson L.D., Alice M.B. Molecular Beams of Macroions. J Chem Phys. 1968;49(5):2240-2249.

97. Yamashita M., Fenn J.B. Negative ion production with the electrospray ion source. J Phys Chem. 1984;88(20):4671-4675.

98. Александров М., Галль Л., Краснов Н., Николаев В., Павленко В., Шкуров В., et al. Прямая стыковка микроколоночного жидкостного хроматографа с масс-спектрометром. Биоорганическая химия. 1984;10(5):710-711.

99. Smith R.D., Loo J.A., Edmonds C.G., Barinaga C.J., Udseth H.R. New developments in biochemical mass spectrometry: electrospray ionization. Anal Chem. 1990;62(9):882-899.

100. Wong S., Meng C., Fenn J. Multiple charging in electrospray ionization of poly (ethylene glycols). J Phys Chem. 1988;92(2):546-550.

101. Kebarle P., Verkerk U.H. Electrospray: From ions in solution to ions in the gas phase, what we know now. Mass Spectrom Rev. 2009;28(6):898-917.

102. Iribarne J.V., Thomson B.A. On the evaporation of small ions from charged droplets. J Chem Phys. 1976;64(6):2287-2294.

103. Konermann L., Ahadi E., Rodriguez A.D., Vahidi S. Unraveling the mechanism of electrospray ionization. Anal Chem. 2013;85(1):2-9.

104. Cech N.B., Enke C.G. Practical implications of some recent studies in electrospray ionization fundamentals. Mass Spectrom Rev. 2001;20(6):362-387.

105. Page J.S., Kelly R.T., Tang K., Smith R.D. Ionization and transmission efficiency in an electrospray ionization—mass spectrometry interface. J Am Soc Mass Spectrom. 2007;18(9):1582-1590.

106. Shaffer S.A., Prior D.C., Anderson G.A., Udseth H.R., Smith R.D. An Ion Funnel Interface for Improved Ion Focusing and Sensitivity Using Electrospray Ionization Mass Spectrometry. Anal Chem. 1998;70(19):4111-4119.

107. Kim T., Udseth H.R., Smith R.D. Improved ion transmission from atmospheric pressure to high vacuum using a multicapillary inlet and electrodynamic ion funnel interface. Anal Chem. 2000;72(20):5014-5019.

108. Chowdhury S.K., Katta V., Chait B.T. An electrospray‐ionization mass spectrometer with new features. Rapid Commun Mass Spectrom. 1990;4(3):81-87.

109. Voyksner R.D., Lee H. Improvements in LC/electrospray ion trap mass spectrometry performance using an off-axis nebulizer. Anal Chem. 1999;71(7):1441-1447.

110. Nemes P., Marginean I., Vertes A. Spraying Mode Effect on Droplet Formation and Ion Chemistry in Electrosprays. Anal Chem. 2007;79(8):3105-3116.

111. Ogorzalek Loo R.R., Udseth H.R., Smith R.D. A new approach for the study of gas-phase ion-ion reactions using electrospray ionization. J Am Soc Mass Spectrom. 1992;3(7):695-705.

112. Brecht D., Uteschil F., Schmitz O.J. Development of a fast-switching dual (ESI/APCI) ionization source for liquid chromatography/mass spectrometry. Rapid Commun Mass Spectrom. 2020;34(17):e8845.

113. Cristoni S., Bernardi L.R., Biunno I., Guidugli F. Analysis of protein ions in the range 3000-12000 Th under partial (no discharge) atmospheric pressure chemical ionization conditions using ion trap mass spectrometry. Rapid Communications in Mass Spectrometry. 2002;16:1153-1159.

114. Cristoni S., Bernardi L.R., Biunno I., Tubaro M., Guidugli F. Surface-activated no-discharge atmospheric pressure chemical ionization. Rapid Commun Mass Spectrom. 2003;17(17):1973-1981.

115. Cristoni S., Rubini S., Bernardi L.R. Development and applications of surface-activated chemical ionization. Mass Spectrom Rev. 2007;26(5):645-656.

116. Xie L., Dou X.Q., Zhou J. Sizing charged particles by phase Doppler anemometry. Applied Optics. 2016;55(12).

117. Olumee Z., Callahan J.H., Vertes A. Droplet dynamics changes in electrostatic sprays of methanol− water mixtures. J Phys Chem. 1998;102(46):9154-9160.

118. Koo J.Y., Kim J.-H. Assessment of a phase Doppler anemometry technique in dense droplet laden jet. KSME International Journal. 2003;17:1083-1094.

119. Brown D.A.R., Jones P.N., Middleton J.C., Papadopoulos G., Arik E.B. Experimental Methods. Handbook of Industrial Mixing2003. p. 145-256.

120. Prehm J., Hartz K. Diagnostics in Thermal Spraying Processes. Modern Surface Technology2006. p. 191-203.

121. Dobrowolska K., Sosnowski T. Evolution of droplet size distribution in selected nebulizers. Physicochemical Problems of Mineral Processing. 2020:32-40.

122. Tsai C.S., Mao R.W., Tsai S.C., Shahverdi K., Zhu Y., Lin S.K., et al. Faraday Waves-Based Integrated Ultrasonic Micro-Droplet Generator and Applications. Micromachines (Basel). 2017;8(2).

123. Jafari M.T., Ramazani S. Design of an ultrasonic piezoelectric injection port for analysis of thermally unstable compounds using corona discharge ion mobility spectrometry. Anal Chim Acta. 2018;1038:79-86.

124. Kambara H. Sample Introduction System for Atmospheric Pressure Ionization Mass Spectrometry of Nonvolatile Compounds. Anal Chem. 1982;54:143-146.

125. Saarela V., Haapala M., Kostiainen R., Kotiaho T., Franssila S. Glass microfabricated nebulizer chip for mass spectrometry. Lab Chip. 2007;7(5):644-646.

126. Franssila S., Marttila S., Kolari K., Ostman P., Kotiaho T., Kostiainen R., et al. A Microfabricated Nebulizer for Liquid Vaporization in Chemical Analysis. J Microelectromech Syst. 2006;15(5):1251-1259.

127. Go D.B., Atashbar M.Z., Ramshani Z., Chang H.C. Surface acoustic wave devices for chemical sensing and microfluidics: A review and perspective. Analytical Methods. 2017;9(28):4112-4134.

128. Kiontke A., Roudini M., Billig S., Fakhfouri A., Winkler A., Birkemeyer C. Surface acoustic wave nebulization improves compound selectivity of low-temperature plasma ionization for mass spectrometry. Sci Rep. 2021;11(1):2948.

129. Straub R., Linder M., Voyksner R.D. Determination of. beta.-lactam residues in milk using perfusive-particle liquid chromatography combined with ultrasonic nebulization electrospray mass spectrometry. Anal Chem. 1994;66(21):3651-3658.

130. Banks J.F., Shen S., Whitehouse C.M., Fenn J.B. Ultrasonically assisted electrospray ionization for LC/MS determination of nucleosides from a transfer RNA digest. Anal Chem. 1994;66(3):406-414.

131. Leal Cunha R., da Silva Lima Oliveira C., Lima de Oliveira A., Maldaner A.O., P. Pereira P.A. Fast determination of amphetamine-type stimulants and synthetic cathinones in whole blood samples using protein precipitation and LC-MS/MS. Microchem J. 2021;163.
132. McEwen C.N., Pagnotti V.S., Inutan E.D., Trimpin S. New paradigm in ionization: multiply charged ion formation from a solid matrix without a laser or voltage. Anal Chem. 2010;82(22):9164-9168.
133. Trimpin S., Inutan E.D. New ionization method for analysis on atmospheric pressure ionization mass spectrometers requiring only vacuum and matrix assistance. Anal Chem. 2013;85(4):2005-2009.
134. Diefenbach X.W., Farasat I., Guetschow E.D., Welch C.J., Kennedy R.T., Sun S., et al. Enabling Biocatalysis by High-Throughput Protein Engineering Using Droplet Microfluidics Coupled to Mass Spectrometry. ACS Omega. 2018;3(2):1498-1508.
135. Cristoni S., Bernardi L.R., Guidugli F., Tubaro M., Traldi P. The role of different phenomena in surface-activated chemical ionization (SACI) performance. J Mass Spectrom. 2005;40:1550-1557.